Model-based Analysis of Individual Atrioventricular Node Conduction Dynamics During Atrial Fibrillation

Karlsson, Mattias

2024

Document Version:
Publisher's PDF, also known as Version of record

Model-based Analysis of Individual Atrioventricular Node Conduction Dynamics During Atrial Fibrillation

Mattias Karlsson

LUND
UNIVERSITY

Doctoral Dissertation
by due permission of the Faculty of Engineering, Lund University, Sweden.
To be defended in E:1406, Ole Römers väg 3, Lund
November 12, 2024, at 13:00

Faculty opponent
Doctor Michela Masè

Organization	Document name
Department of Biomedical Engineering Lund University SE 22100 Lund	DOCTORAL DISSERTATION
	Date of issue November 2024
	Sponsoring organization Fraunhofer-Chalmers Centre
Author(s) Mattias Karlsson	

Title and subtitle

Model-based Analysis of Individual Atrioventricular Node Conduction Dynamics During Atrial Fibrillation

Atrial fibrillation (AF) is the most common arrhythmia in the world, leading to a significant burden to patients and the healthcare system. It is characterised by rapid and irregular atrial contractions stemming from disorganised electrical activity in the atria. The atrioventricular (AV) node regulates heart rate during AF by filtering electrical impulses from the atria.

However, for persistent AF, the regulating capabilities of the AV node are often insufficient in regards to maintaining a healthy heart rate. Thus, rate control drugs affecting the conduction properties of the AV node are the most common treatment, chosen empirically for each patient. This takes time and may result in a sub-optimal drug choice. Quantifying individual differences in AV-nodal function is therefore interesting in order to potentially aid in personalised treatment selection.

This thesis focuses on assessing the conduction properties of the AV node during AF from electrocardiography recordings, specifically the refractory period and conduction delay. The thesis comprises an introduction to the anatomy of the heart, AF, cardiac modelling, and parameter estimation, as well as four papers. The first paper proposes a mathematical model of the AV node where the model parameters could be estimated from 15-minute ECG recordings utilising a genetic algorithm. In the second paper, we used the proposed model and introduced a computationally efficient dynamic genetic algorithm to enable estimation of 24-hour model parameter trends, with a temporal resolution of one estimate per 1000 RR intervals, to analyse individual and drug-dependent differences in the model parameters. In the third paper, the optimisation framework was further extended to combine an Approximate Bayesian computation algorithm with the previously proposed genetic algorithm in order to quantify the uncertainty of the model parameter estimates. Additionally, a model parameter reduction step was introduced to increase interpretability of the results. In the fourth paper an improved optimisation framework consisting of a particle filter and an associated smoothing algorithm enabling beat-to-beat temporal resolution was proposed. This temporal resolution allows for analysis of beat-to-beat changes in the AV node conduction properties induced by the autonomic nervous system.

All-in-all, the work presented in this thesis has made it possible for the first time to assess the conduction properties of the AV node during AF based on ECG measurements.

Key words:

Mathematical modeling, Genetic algorithm, Atrioventricular node, Atrial fibrillation, Particle filter

Classification system and/or index terms (if any):

-

Supplementary bibliographical information: -		Language English
ISSN and key title: -		ISBN 978-91-8104-179-8 (printed) 978-91-8104-180-4 (electronic)
Recipient's notes -	Number of pages 148	Price -
	Security classification -	

Signature Date: 12 November 2024

Public defence
November 12, 2024, at 13:00 in E:1406, E-building, LTH, Ole Römers väg, 223 63 Lund, Sweden.

Supervisors
Docent Frida Sandberg
Dept. of Biomedical Engineering, Lund University, Lund, Sweden
Doctor Mikael Wallman
Dept. of Systems and Data Analysis, Fraunhofer-Chalmers centre, Gothenburg, Sweden
Docent Mats Jirstrand
Dept. of Systems and Data Analysis, Fraunhofer-Chalmers centre, Gothenburg, Sweden
Professor Pyotr G. Platonov
Dept. of Cardiology, Clinical Sciences, Lund University, Lund, Sweden

Faculty opponent
Doctor Michela Masè
Dept. of Industrial Engineering, University of Trento, Trento, Italy

Examination board
Docent Johannes Töger
Dept. of Clinical Physiology, Lund University, Sweden
Professor Philip Gerlee
Dept. of Mathematical Sciences, Chalmers, Gothenburg, Sweden
Docent Seraina Dual
Dept. of Biomedical Engineering and Health Systems, Royal Institute of Technology, Stockholm, Sweden
Deputy member: Professor Bo Bernhardsson
Dept. of Automatic Control, Lund University, Lund, Sweden

Chairman
Docent Christian Antfolk
Dept. of Biomedical Engineering, Lund University, Lund, Sweden

Cover illustration
Artistic representation of the human heart surrounded by signals.
Illustration by: Mattias Karlsson, partly using Microsoft Copilot.

ISBN: 978-91-8104-179-8 (print)
ISBN: 978-91-8104-180-4 (pdf)
Report No. 1/24
Printed by Tryckeriet, E-building, Faculty of Engineering, Lund University, Lund Sweden

Dedicated to Eva and Magnus Karlsson.

Populärvetenskaplig Sammanfattning

Hjärt- och kärlsjukdomar var den vanligaste dödsorsaken i Sverige år 2023, med förmaksflimmer som den vanligaste arytmin. Idag lever cirka 330000 svenskar med förmaksflimmer, vilket gör att tillståndet klassas som en folksjukdom. Därför är risken stor att du som läser detta har en vän eller närstående som lider av förmaksflimmer, eller kanske rent av gör det själv. Med förmaksflimmer ökar risken för blodpropp och stroke markant. Av dessa anledningar läggs stora resurser på forskning inom området, denna avhandling inkluderad.

Hjärtats rytm styrs av en elektrisk aktivering som startar i sinusknutan, belägen i höger förmak. Normalt aktiveras först förmaken av sinusknutan, varefter den elektriska impulsen leds vidare via atrioventrikulärknutan (AV-knutan) till kamrarna. Den här elektriska aktiveringen får hjärtmuskeln att dra ihop sig, vilket gör att blodet pumpas ut i lungorna och resten av kroppen. Vid förmaksflimmer störs den normala rytmen från sinusknutan ut av högfrekvent och kaotisk elektrisk aktivitet i förmaken. Lyckligtvis har AV-knutan förmågan att hindra alltför högfrekvent elektrisk aktivitet från att nå kamrarna, men hjärtrytmen under förmaksflimmer blir ändå snabb och oregelbunden.

För att behandla patienter med permanent förmaksflimmer ges som första steg ett läkemedel för att minska pulsen, vanligtvis betablockerare eller kalciumflödeshämmare. Eftersom alla människor är olika ger de två läkemedelstyperna dock olika resultat för olika individer, vilket gör att man ofta måste testa flera läkemedel innan man hittar ett som fungerar bra. Detta tar både tid och riskerar att leda till ett slutgiltigt val av ett läkemedel som fungerar tillräckligt bra, men ej optimalt. Detta kan i sin tur leda

till ett onödigt lidande och potentiellt en högre risk för blodpropp och stroke hos personer med förmaksflimmer.

Eftersom AV-knutan till stor del reglerar pulsen under förmaksflimmer är dess individuella egenskaper en stor bidragande faktor till ett läkemedels effekt. Därför är det av intresse att karaktärisera AV-knutans egenskaper individuellt. För att det ska vara praktiskt möjligt bör karaktäriseringen baseras på vanliga EKG-inspelningar.

Den här avhandlingen handlar om hur man med hjälp av matematisk modellering och parameteroptimering kan skatta egenskaper relaterade till refraktärtid och överledningshastighet i en individs AV-knuta baserat på EKG-inspelningar, och hur dessa egenskaper skiljer sig mellan individer samt hur de påverkas av olika läkemedel. Mycket av AV-knutans beteende och egenskaper är fortfarande ett mysterium, men genom detta arbete har vi kunnat visa hur man med hjälp av matematik och ingenjörskap kan få en bättre förståelse av AV-knutan, och därmed tagit ett steg i riktning mot skräddarsydda behandlingar för folksjukdomen förmaksflimmer.

Abstract

Atrial fibrillation (AF) is the most common arrhythmia in the world, leading to a significant burden to patients and the healthcare system. It is characterised by rapid and irregular atrial contractions stemming from disorganised electrical activity in the atria. The atrioventricular (AV) node regulates heart rate during AF by filtering electrical impulses from the atria.

However, for persistent AF, the regulating capabilities of the AV node are often insufficient in regards to maintaining a healthy heart rate. Thus, rate control drugs affecting the conduction properties of the AV node are the most common treatment, chosen empirically for each patient. This takes time and may result in a sub-optimal drug choice. Quantifying individual differences in AV-nodal function is therefore interesting in order to potentially aid in personalised treatment selection.

This thesis focuses on assessing the conduction properties of the AV node during AF from electrocardiography recordings, specifically the refractory period and conduction delay. The thesis comprises an introduction to the anatomy of the heart, AF, cardiac modelling, and parameter estimation, as well as four papers. The first paper proposes a mathematical model of the AV node where the model parameters could be estimated from 15-minute ECG recordings utilising a genetic algorithm. In the second paper, we used the proposed model and introduced a computationally efficient dynamic genetic algorithm to enable estimation of 24-hour model parameter trends, with a temporal resolution of one estimate per 1000 RR intervals, to analyse individual and drug-dependent differences in the model parameters. In the third paper, the optimisation framework was further extended to combine an Approximate Bayesian computation algorithm with the previously proposed genetic algorithm in order to quantify the uncertainty of the model parameter estimates. Additionally, a model parameter reduction step was introduced to increase interpretability of the results. In

the fourth paper an improved optimisation framework consisting of a particle filter and an associated smoothing algorithm enabling beat-to-beat temporal resolution was proposed. This temporal resolution allows for analysis of beat-to-beat changes in the AV node conduction properties induced by the autonomic nervous system.

All-in-all, the work presented in this thesis has made it possible for the first time to assess the conduction properties of the AV node during AF based on ECG measurements.

List of Papers

Included

I. **Non-invasive Characterization of Human AV-nodal Conduction Delay and Refractory Period During Atrial Fibrillation.**
Mattias Karlsson, Frida Sandberg, Sara R Ulimoen, Mikael Wallman
Published in: Frontiers in Physiology, vol. 12, 728955, 2021

The author developed the AV node model, the error function, and the genetic algorithm. He also created the ground truth data, analysed the results, and wrote the manuscript.

II. **ECG Based Assessment of Circadian Variation in AV-nodal Conduction During AF — Influence of Rate Control Drugs.**
Mattias Karlsson, Mikael Wallman, Pyotr G Platonov, Sara R Ulimoen, Frida Sandberg
Published in: Frontiers in Physiology, vol. 13, 976526, 2022

The author designed the genetic algorithm and the mixed effect model, analysed the results, and wrote the manuscript.

III. **Model-based Estimation of AV-nodal Refractory Period and Conduction Delay Trends from ECG.**
Mattias Karlsson, Pyotr G Platonov, Sara R Ulimoen, Frida Sandberg, Mikael Wallman
Published in: Frontiers in Physiology, vol. 14, 1287365, 2024

The author developed the approximate Bayesian computation algorithm, trained the machine learning algorithms, analysed the results, and wrote the manuscript.

IV. ECG-based Beat-to-beat Assessment of AV Node Conduction Properties during AF.
Mattias Karlsson, Felix Plappert, Pyotr G Platonov, Sten Östenson, Mikael Wallman, Frida Sandberg
Manuscript form

The author developed the particle filters and smoothing algorithms, analysed the results, and wrote the manuscript.

Related

Different parts of the work have also been published in

I. Non-Invasive Characterization of Atrio-Ventricular Properties During Atrial Fibrillation
Mattias Karlsson, Mikael Wallman, Sara R Ulimoen, Frida Sandberg
In Proceedings of Computing in Cardiology, Brno, Czech Republic, 2021.

II. Drug Dependent Circadian Variations in AV-nodal Properties During Atrial Fibrillation
Mattias Karlsson, Mikael Wallman, Pyotr G Platonov, Sara R Ulimoen, Frida Sandberg
In Proceedings of Computing in Cardiology, Tampere, Finland, 2022.

III. ECG-based Assessment and Therapeutic Implications of AV Nodal Conduction Dynamics During Atrial Fibrillation
Mattias Karlsson, Mikael Wallman, Pyotr G Platonov, Sara R Ulimoen, Frida Sandberg
In Proceedings of Computing in Cardiology, Atalanta, USA, 2023.

IV. Beat-to-beat In Silico Assessment of AV-nodal Conduction Dynamics during AF
Mattias Karlsson, Pyotr G Platonov, Frida Sandberg, Mikael Wallman
In Proceedings of Computing in Cardiology, Karlsruhe, Germany, 2024.

Acknowledgments

I would like to start things off by thanking the two most influential and supporting people throughout my PhD journey, my two supervisors Frida and Micke. Frida for being the grounding factor that keeps my work honest and focused. Micke for always sparking new ideas and for being a great office mate. I could not have asked for a better team to work with.

I spend most of my working hours in Gothenburg and would therefore like to thank all my colleagues in the department at FCC, led by my boss and supervisor Mats. A special thanks go to Viktor, Marcus, and Ludvig for your camaraderie and friendship. Marcus, you were the first one I befriended at the office, and we met more times for AW than at the office for the first year (Covid might had something to do with that). Viktor, you are insane and I love you for it.

For my second home during my time as a PhD student, I would like to thank everyone at the department in Lund. Special thanks to Johan and Lorenzo for making my first weeks in Lund something special, and to Jules who came in during the end. An extra special thanks to Felix, thank you kindly. Not only have we worked very closely together, but I found a friend in you from the first online meeting we had. A friendship that has not slowed for a second. And I can not mention Lund without thanking Lea. Too much can be said for you, and nothing could ever be enough. We met during my first visit to Lund, and since that day you have been the centre of my every day.

My thanks would not be complete without a big thanks to the medical doctors, Pyotr and Sara, for taking time from your busy work to read and give me feedback from a medical perspective.

Lastly, my journey to this PhD started long before I started as a PhD student. The biggest thanks go to my family and friends. I am grateful for the friends who existed since forever, thank you Ellen, Andreas, Galeskid (heja Häslö), and Richard. Thank you to the guys from Chalmers who I now have known for over 10 years! Thank you to the boys from the Ö-squad. And thank you to my family for everything. One final thanks goes to Patrik Nilsson for starting my scientific interest and career.

Mattias Karlsson
Göteborg 2024

List of Abbreviations

ABC Approximate Bayesian computation

AF Atrial fibrillation

AV Atrioventricular

ANS Autonomic nervous system

ECG Electrocardiography

FP Fast pathway

f-waves Fibrillatory waves

PPG Photoplethysmogram

SA Sinoatrial

SP Slow pathway

Contents

Part I

Introduction

Chapter 1
Background and Aims

1.1 Background

Atrial fibrillation (AF), the most common arrhythmia globally, is characterised by rapid and irregular atrial contractions stemming from highly disorganised electrical activity within the atria [7]. The prevalence of AF is highly correlated with age, as shown in Figure 1.1. Importantly, AF is associated with a heightened risk of mortality, primarily due to complications such as heart failure and stroke [8, 9].

During AF, the atrioventricular (AV) node acts as a gatekeeper between the atria and ventricles, partially shielding the ventricles from the chaotic electrical activity in the atria. By blocking and delaying incoming impulses, the AV node protects the ventricles from the rapid and irregular contractions seen in the atria. However, these efforts are often insufficient to maintain a healthy heart rate during AF.

Fortunately, rate control drugs offer a way to reduce the heart rate by mechanisms partly acting on the AV node conduction properties. Two types of rate control drugs are primarily used for AF treatment: β-blockers and calcium channel blockers, each with distinct physiological effects [7]. Due to the difference in physiological effects between the drugs, they affect the AV node conduction properties differently. While both drug types demonstrably decrease heart rate at a population level, their individual impacts on ventricular activation rate can vary significantly [10]. Notably, one key physiological distinction between these drug types lies in their influence on the autonomic nervous system (ANS). This distinction is important, considering the role of the ANS in initiating and maintaining AF [11]. Consequently, inter-patient variability in ANS activity might significantly influence individual responses to AF treatment. However, the choice of drug for a specific patient is often made empirically,

which can lead to a prolonged time until successful treatment and possibly result in a sub-optimal final choice of drug [7]. Thus, patient-specific information about the AV node conduction properties could give insights into a drug's impact on the ventricular activation rate and in turn guide therapeutic decisions.

This thesis focuses on quantifying variations in AV nodal conduction properties. However, since directly measuring AV node conduction properties during AF non-invasively is not feasible, an alternative approach is required.

Mathematical models have served as a cornerstone tool in science and engineering for centuries. They allow us to describe the world around us, analyse interactions within complex systems, and make predictions. These advantages, in concert with the ever-increasing computing power at our disposal, have led to the use of models in healthcare becoming more prevalent than ever [12, 13].

At their core, models aim to represent real-world systems in an objective, simplified, and ultimately useful way. However, it is important to recognise that all models are inherently simplifications of reality, and as such, they may not capture the full complexity of real-world systems. Despite this limitation, they remain valuable tools. A common approach involves fitting models to data, allowing us to draw meaningful conclusions about the underlying phenomena of interest, such as the AV node properties. This is precisely the approach we will utilise in this thesis.

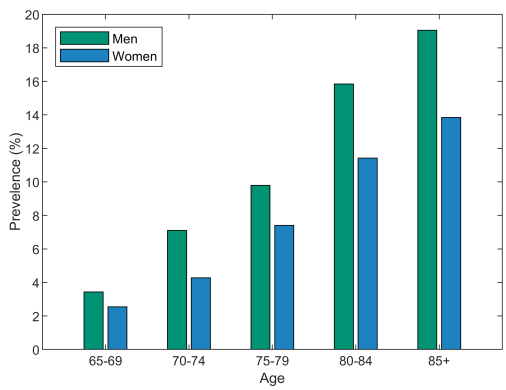

Figure 1.1: Prevalence of AF in the Italian population, stratified by age and gender, assumed representative for the European Union [14]. Reprint from [15].

1.2 Motivation and Aims

As previously described, the AV node is known to regulate ventricular activation during AF, and its properties can be affected by the ANS as well as by rate control drugs. Thus, patient-specific information about the AV node and the drug-dependent effect during AF may prove to be a key factor in personalised treatment selection during AF. However, there are currently no tools available for non-invasive analysis of the AV node properties for patients with AF. For such a tool to be clinically relevant, it should ideally rely solely on non-invasive data, such as electrocardiography (ECG) recordings, for parameter estimation.

In this thesis, mathematical modelling has been used to assess time-variations in AV node conduction properties during AF from ECG signals and to study the drug-dependent effects on these assessments. The extracted information about variations in AV node properties could be used to guide the treatment strategy on an individual basis. Therefore, the overall goal is to quantify variations in AV node conduction properties and the influence of rate control drugs on the AV node and ANS using non-invasive data. This is addressed in this thesis by the following three aims:

Aim 1: To develop a mathematical model of the AV node that accounts for its electrophysiological properties, is capable of replicating its behaviour during AF, and which computational efficiency allows for patient-specific parameter estimation (addressed in *Paper I*).

Aim 2: To set up a framework for reliable estimation of model parameters based on ECG recordings (addressed in *Paper II-IV*).

Aim 3: To evaluate the applicability of the proposed method in a clinical context by analysing drug-induced and ANS-related changes in AV node conduction properties during AF (addressed in *Paper II-IV*).

1.3 Thesis Outline

This thesis is divided into two parts: *Part I*, the Introduction, and *Part II*, the included research papers. *Part I* comprises seven chapters, providing foundational knowledge and context for the research presented in *Part II*.

The remainder of *Part I* is organised as follows: Chapter 2 delves into the anatomy of the heart, with a particular focus on the conduction system. This chapter lays the

groundwork for modelling the heart during AF. Chapter 3 provides a more detailed description of AF by explaining its origins, treatment options, and the characteristic ECG patterns observed during this condition.

Shifting the focus from physiology to engineering, Chapter 4 introduces the concept of cardiac modelling and provides an overview of existing AV node models, including the one presented in *Paper I*. Chapter 5 introduces optimisation and parameter estimation concepts and various relevant algorithms. Chapter 6 summaries the four research papers included in *Part II*. Finally, Chapter 7 discusses potential future research directions related to this work and thereby concludes the thesis.

Chapter 2

Anatomy of the Heart

A thorough understanding of the heart function during normal sinus rhythm is essential for understanding it during AF. This chapter provides a detailed examination of the heart's anatomy (Section 2.1), encompassing both overall structure and the cellular mechanisms responsible for a heartbeat. Subsequently, Section 2.2 focuses on the heart's conduction system, with particular emphasis on the AV node and the sinoatrial (SA) node.

2.1 Cardiac Anatomy and Mechanical Function

The heart functions as a muscular pump, continuously propelling blood throughout the body to deliver oxygen. As illustrated in Figure 2.1, it comprises four chambers: two atria and two ventricles. Deoxygenated blood from the body enters the right atrium via the superior and inferior vena cava. Right atrial contraction then pumps blood into the right ventricle, which subsequently pumps it to the lungs through the pulmonary arteries for gas exchange. Oxygenated blood from the lungs reaches the left atrium via the pulmonary veins, and left atrial contraction fills the left ventricle. Finally, the left ventricle pumps blood via the aorta throughout the rest of the body.

To achieve this pumping function, the heart wall consists primarily of cardiac muscle tissue, known as the myocardium. The thickness of the myocardium varies across the chambers, reflecting their distinct workloads. The atria possess thinner walls compared to the ventricles, and the left ventricle has thicker walls than the right ventricle.

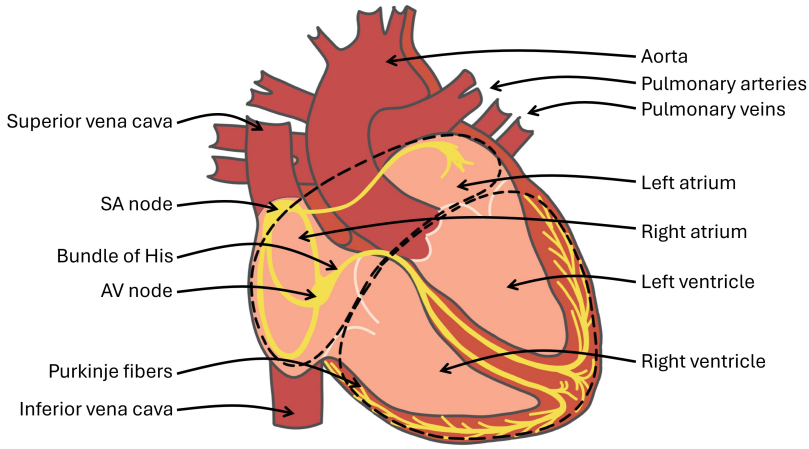

Figure 2.1: A schematic figure of the human heart with the conduction system highlighted in yellow. The figure was created by Felix Plappert with inspiration from [16].

2.1.1 Cardiomyocytes

The myocardium is composed of individual cardiac muscle cells, termed cardiomyocytes. Within each cardiomyocyte reside long contractile fibers known as myofibrils. These myofibrils contain thick myosin and thin actin filaments, the fundamental components responsible for cellular contraction [17]. Contraction is initiated when myosin heads bind to actin, forming cross-bridges between the filaments. As a source of energy, the myosin heads can bind and split adenosine triphosphate. This energy is used to pull the thick and thin filaments along each other, thereby shortening the myofibril. Subsequently, the myosin head binds a new adenosine triphosphate molecule, detaches from the actin, and repeats the cycle.

The coordinated action of numerous myosin heads within a myofibril collectively contract that myofibril. Similarly, all myofibrils within a cardiomyocyte work together to contract that cardiomyocyte. For the coordinated contraction of an entire chamber, all cardiomyocytes within that chamber must contract simultaneously. However, this process is not spontaneous. In a relaxed state, the protein tropomyosin blocks the binding sites which prevents myosin head attachment. The influx of calcium ions (Ca^{2+}) triggers a change in the tropomyosin, removing the blockade and enabling myosin-actin interaction. Calcium originates from two sources: the sarcoplasmic reticulum, an internal cellular store, and the extracellular space, accessed through Ca^{2+}-specific ion channels and T-tubules during an action potential – a rapid rise and a more prolonged fall in membrane potential across the cell membrane [17].

The generation of an action potential relies primarily on two key components; a resting membrane potential and the presence of specific ion channels. These specialised channels allow for the selective diffusion of ions across the plasma membrane, following the principle of diffusion from high to low concentration. This movement of ions generates an ionic current that alters the membrane potential. Ion channels are equipped with gates that regulate the passage of ions. Two main types of ion channels contribute to the action potential; the leaky channels, which open and close seemingly at random, and the voltage-gated channels, which open upon a change in membrane potential.

The resting membrane potential in a cardiomyocyte corresponds to the difference in voltage between the intracellular and extracellular environments. This resting potential is established by the continuous outward flux of potassium ions (K^+) through numerous leaky K^+ channels, and an inward current of sodium ions (Na^+) via leaky Na^+ channels. This interplay, along with the action of sodium-potassium pumps actively transporting Na^+ out of the cell and K^+ into the cell, creates the stable resting membrane potential.

When a stimulus, such as an influx of ions from an adjacent cell, disrupts the resting membrane potential by exceeding a threshold level (Figure 2.2a, phase 4), an action potential is initiated in the cardiomyocyte. This stimulus marks the beginning of phase 0 and triggers the opening of voltage-gated Na^+ channels, leading to a rapid rise in membrane potential due to Na^+ influx [18]. The Na^+ channels then deactivate shortly thereafter, coinciding with the activation of K^+ channels, which initiate the repolarization phase (phase 1) by efflux of K^+. During phase 0, Ca^{2+} channels are also activated, although with a slower opening and closing compared to the Na^+ channels. This delayed activation results in a later influx of Ca^{2+} that persists for a longer duration than Na^+ influx. The combined effect of Ca^{2+} influx and continued K^+ efflux creates the plateau phase observed in phase 2. The action potential concludes with phase 3, characterised by the closure of Ca^{2+} channels and a dominant outward current of K^+ ions, which restores the cell to its resting membrane potential (phase 4). The cardiomyocytes are linked by intercalated discs, which contain gap junctions that permit the rapid flow of ions between adjacent cells. This allows for the fast propagation of action potentials from cell to cell, ensuring synchronised contraction of the entire heart chamber.

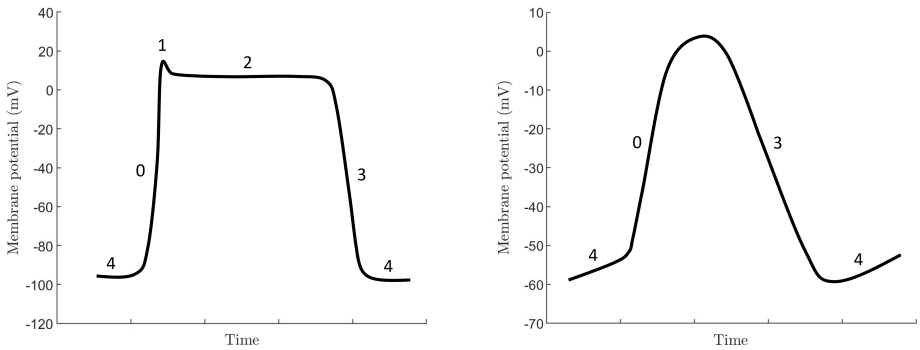

(a) Cardiomyocyte **(b)** Pacemaker cell

Figure 2.2: Action potential in a cardiomyocyte (a) and in a pacemaker cell (b). Note that there is no distinct phase in the pacemaker cell resembling phase 1 or 2 in the cardiomyocyte. Reprint from [15].

2.2 Conduction System of the Heart

The rhythmic contraction of the myocardium originates from the SA node, located in the right atrial wall (see Figure 2.1). This specialised region generates action potentials at a rate determined by the body's blood demand, which in turn is regulated by the ANS. The action potentials originating from the SA node conduct rapidly throughout both atria through the intercalated discs, leading to synchronised atrial contraction.

Before reaching the ventricles, the action potential travels through the AV node, the sole conduction point between the chambers. Three internodal pathways, characterised by a higher conduction velocity compared to the atrial myocardium, carry the action potential from the SA node to the AV node [19]. The AV node acts as a gatekeeper, delaying or blocking incoming electrical impulses based on their rate. This delay allows for efficient pumping of blood by ensuring proper timing between atrial and ventricular contractions. When an impulse is conducted by the AV node, it reaches the bundle of His, which splits into the right and left bundle branches. These branches further deliver the impulse to the Purkinje fibers (Figure 2.1), triggering ventricular contraction. Purkinje fibers are specialised cardiomyocytes with a fast conduction velocity compared to both the internodal pathways and other cardiomyocytes [20].

During cardiac arrhythmias such as AF, this structured conduction pathway becomes disrupted. In AF, the rapid electrical activations of the surrounding tissue block the normal function of the SA node, leaving it unable to initiate a new action potential. Consequently, the AV node plays a more prominent role.

2.2.1 Sinoatrial Node

As previously mentioned, cardiac electrical activation is normally initiated by the SA node. In healthy hearts, the SA node maintains a steady pace by virtue of specialised pacemaker cells that continuously generate action potentials, setting the heart rhythm. Unlike regular cardiomyocytes, pacemaker cells lack a resting potential and instead exhibit spontaneous depolarisation immediately after repolarization. To achieve this, the pacemaker cells in the SA node have specific anatomical features and unique ion channels. In contrast to the non-SA nodal myocardium, the SA node does not have a stable resting potential, thereby facilitating pacemaking activity.

The action potential in pacemaker cells, depicted in Figure 2.2b, can be divided into three phases: a pacemaker potential phase (4), a depolarisation phase (0), and a repolarization phase (3). The numbering of these phases corresponds to the five phases of the action potential in non-pacemaker cardiomyocytes (Figure 2.2a). The most significant difference between the action potentials of cardiomyocytes and pacemaker cells lies in phase 4, the resting potential phase. In pacemaker cells, phase 4 begins immediately after repolarization, with the majority of K^+ channels closing, leading to a reduced outward K^+ current [21]. The highly negative membrane potential also activates hyperpolarisation-activated cyclic nucleotide-gated channels, contributing to the pacemaker potential by generating an inward current of K^+ and Na^+ ions. Additionally, the release of stored calcium within the sarcoplasmic reticulum further increases the pacemaker potential. This released calcium is exchanged for Na^+, resulting in an inward current. The final part of phase 4 involves the opening of the so-called T-type Ca^{2+} channels, a fast-activating type of calcium channel, along with the slower activation of L-type Ca^{2+} channels, transporting Ca^{2+} ions into the cell. Both these channels are voltage-gated channels, opening when the membrane potential reaches a specific threshold. During phase 0, the membrane potential rises rapidly due to the full activation of the slow L-type channels. Concurrently, both the T-type channels and the hyperpolarisation-activated cyclic nucleotide-gated channels close. In phase 3, the L-type channels close, and the K^+ channels open, leading to repolarization of the membrane potential. This repolarization generates the electrical impulse that will subsequently activate the heart and sets the stage for the next cycle, beginning with phase 4 [21].

2.2.2 Atrioventricular Node

The AV node plays a critical role in optimising heart function by performing three key tasks: delaying incoming electrical impulses, filtering out high-frequency atrial activations, and functioning as a secondary pacemaker. The delay mechanism is the most important part for healthy hearts, ensuring efficient pumping of blood by allowing sufficient time for ventricular filling after atrial contraction.

Several anatomical and physiological features contribute to the ability of the AV node to delay impulses. Firstly, the AV node has a lower density of gap junctions compared to the surrounding atrial myocardium, leading to a slower conduction velocity [22]. Secondly, the AV node cells themselves are smaller in diameter compared to atrial myocytes. This smaller size further reduces the overall conductance velocity within the node [22]. Finally, the action potential in the AV node also contributes to the delay process. Unlike atrial cardiomyocytes with a fast upstroke driven by a high density of Na^+ channels, the AV node action potential exhibits a slower rise due to a lower Na^+ channel density. Consequently, L-type Ca^{2+} channels play a more prominent role in driving the depolarisation phase of the AV node action potential [23].

The second function of the AV node is to act as a filter for incoming atrial impulses, which is more prominent during atrial tachyarrhythmias. This filtering occurs by blocking or delaying incoming impulses. The blocking occurs when the AV node cells are in their refractory period, a brief window following an action potential where the cells are resistant to further excitation. For transmitted impulses, the conduction velocity can differ, resulting in different conduction delays. These complex patterns of blocking and delaying within the AV node are possible due to its unique dual pathway electrophysiology. The AV node comprises two distinct functional pathways: a fast pathway (FP) and a slow pathway (SP) [24, 25]. The FP has a shorter refractory period but conducts impulses faster compared to the SP. These differences occur due to differences in their cellular composition. The FP consists of longer cells with a larger diameter, while the SP is composed of shorter cells with a smaller diameter [23]. However, the precise anatomical and molecular basis for the pathways of the AV node is not yet fully understood [26]. Studies using an S1-S2 protocol[1] have demonstrated that conduction occurs primarily through the FP for longer S2 intervals. For shorter S2 intervals, the AV node utilises both the FP and the SP for impulse conduction [25]. Additionally, the current clinical criterion of dual pathway physiology in the AV node is a 50 ms jump in the AV conduction curve [27]. However, recent studies challenge the established association between the AV conduction jump and dual pathway physi-

[1]When electrodes are used to deliver a pulse train at a constant interval (S1), followed by a single premature pulse after a shorter interval (S2).

ology [28], suggesting that the underlying mechanisms of the AV node remain elusive.

The AV node can be characterised by its refractory period and conduction delay in its two pathways, which will be denoted RP^{FP}, RP^{SP}, CD^{FP}, and CD^{SP} in this dissertation. Furthermore, the AV node junction, the area where atrial and nodal tissues meet, plays a significant role in AV node conduction properties [29]. Based on electrophysiological recordings of the rabbit AV node junction, different types of AV node cells have been classified; the atrial-nodal cells, the nodal cells, and the nodal-His cells [30, 31].

Another noteworthy aspect of the AV node is its ability to be affected by concealed conduction. Concealed conduction refers to a partial activation of the AV node that does not result in ventricular activation. Despite not generating a ventricular response, concealed conduction can still influence the conduction characteristics of the AV node for later impulses [32]. Finally, the AV node can also function as a secondary pacemaker if the SA node fails. In this scenario, the AV node exhibits an intrinsic activation rate of 20-60 beats per minute [23].

2.3 Autonomic Nervous System Regulation

The ANS regulates the human heart through its sympathetic and parasympathetic divisions. The balance between these ensures optimal cardiac function during various physiological states.

The sympathetic nervous system acts as a physiological activator. It does this by releasing norepinephrine, which binds to β-adrenergic receptors on cardiomyocytes. This binding affects several calcium mechanisms in the cardiomyocytes, including an increased probability of L-type calcium channels opening and increased storage of Ca^{2+} in the sarcoplasmic reticulum [11, 33, 34]. These lead to an increased pacemaker potential and in turn to an increased heart rate (via changes in the SA node) and increased contractility in order to meet heightened demands during exercise or stress [34]. Furthermore, as an effect of the increased influx of Ca^{2+} in cardiomyocytes, increased sympathetic activity is associated with a decrease in AV nodal conduction delay [35, 36, 37, 38] and refractory period [37, 38].

Conversely, the parasympathetic divisions counterbalance the sympathetic effects and slow the heart rate by releasing the neurotransmitter acetylcholine [34, 39]. The release of acetylcholine inhibits the activation of L-type calcium channels, making them less likely to open, in turn slowing the spontaneous firing rate of pacemaker cells in the

SA node [40]. Moreover, large doses of acetylcholine are known to decrease AV node conduction velocity [41]. Note that the activation of the sympathetic and parasympathetic systems is complex, with additional receptors and neurotransmitters influencing heart rate and contractility [34].

Several factors are known to change the ANS activity and are thus used to test the ANS function, such as deep breathing, tilt-table test, direct measures from sympathetic nerve fibers, as well as pharmacological provocation [42, 43, 44]. For this thesis, the tilt test is of interest since ECG recordings from one are used for *Paper IV*. In the context of the ANS, a tilt test evaluates how well the body regulates in response to a change in posture. By observing the body's response to the tilt, insights into the dominance or imbalance within the ANS can be studied. Importantly, a change from a horizontal position to a head-up-tilt position is associated with an increase in sympathetic activity [45]. Moreover, heart rate variability is often used as a basis for ANS activity metrics during normal sinus rhythm [46].

Chapter 3
Atrial Fibrillation

To develop a mathematical model of the AV node for use during AF, a thorough understanding of the arrhythmia itself is necessary. Consequently, this chapter starts with a detailed exploration of AF in Section 3.1. This section delves into the mechanisms underlying the origination and classification of AF. Subsequently, Section 3.2 provides an overview of the ECG during AF. Finally, Section 3.3 discusses the various treatments used to manage AF.

3.1 Mechanisms of Atrial Fibrillation

As previously stated, AF is characterised by rapid and irregular electrical activity within the atria which disrupts the coordinated beating in the atria and ventricles. This arises when the electrical impulse triggering atrial activation fails to terminate normally. Instead, it whirls in chaotic patterns that override the usual activation initiated by the SA node. This can happen due to a combination of factors, including alterations of the structure and electrical properties of the atrial tissue and imbalances in the ANS [47]. Additionally, enhanced automaticity, leading to an increase in the spontaneous firing of electrical impulses, appears to be a common part of the triggering mechanism behind AF. Studies suggest that over 90% of these impulses originate from the pulmonary veins, with the majority arising from the left superior vein [48, 49]. Although great progress has been made in understanding the initiation of AF during the last 50 years, debate regarding the precise mechanisms still exists [50, 47].

However, a trigger mechanism alone is insufficient to sustain AF. Additional factors related to the maintenance of AF are necessary to convert a trigger into an AF episode [51]. The underlying mechanisms responsible for perpetuating AF remain a subject of ongoing debate [52, 53]. The two main contenders are multi-wavelet reen-

try and focal drivers [54]. Additionally, structural and electrical remodelling of the atria plays an important role in AF maintenance. This remodelling process involves changes in cardiomyocyte electrophysiology due to fibroblast activation, enhanced deposition of connective tissue, and fibrosis [7]. The primary electrical consequence is a reduction in conduction velocity within atrial cardiomyocytes, often attributed to alterations in L-type Ca^{2+} channels [55]. These changes can be brought on by structural heart disease, hypertension, or even AF itself, creating a cycle where "AF begets AF" [56]. Consequently, patients with seemingly similar AF symptoms may exhibit diverse underlying physiological mechanisms, necessitating personalised treatment strategies.

Atrial fibrillation can be categorized into five distinct types: first-diagnosed AF (initial diagnosis); paroxysmal AF (self-terminating within seven days); persistent AF (lasting longer than seven days or requiring intervention for sinus rhythm restoration); long-standing persistent AF (lasting more than a year); and permanent AF (accepted by both patient and physician) [7]. In permanent AF, variations regulated by the ANS become particularly relevant, since the two recommended first-line rate control medications – β-blockers and calcium channel blockers – have different physiological effects relating to the ANS.

3.2 Diagnosis of Atrial Fibrillation

The ECG of a patient with AF exhibits distinct characteristics compared to a healthy individual's ECG, thus ECG is used for diagnosing AF. In a healthy heart, as detailed in Section 2.2, the SA node initiates an action potential that propagates through the atria, resulting in atrial contraction. This atrial depolarisation manifests on the ECG as the P-wave, as shown in Figure 3.1. Following conduction through the AV node, the action potential travels throughout the ventricles, triggering ventricular contraction. This ventricular depolarisation is reflected on the ECG by the QRS complex. The sequence of intervals between consecutive R waves on the ECG is termed the RR interval series. During the QRS complex, atrial repolarization also occurs, but is masked by the larger ventricular activity and not readily visible on the ECG. Finally, ventricular repolarization is depicted on the ECG by the T wave.

Three key features are visible on the ECG and used for AF detection and diagnosis: irregular RR intervals, P-wave absence, and the presence of atrial fibrillatory waves (f-waves) [51]. The rapid and irregular electrical activity in the atria during AF translates to rapid and irregular stimulation of the AV node. This, in turn, results in irregular RR intervals, as depicted in Figure 3.1 and 3.2a. The irregularity of the RR intervals

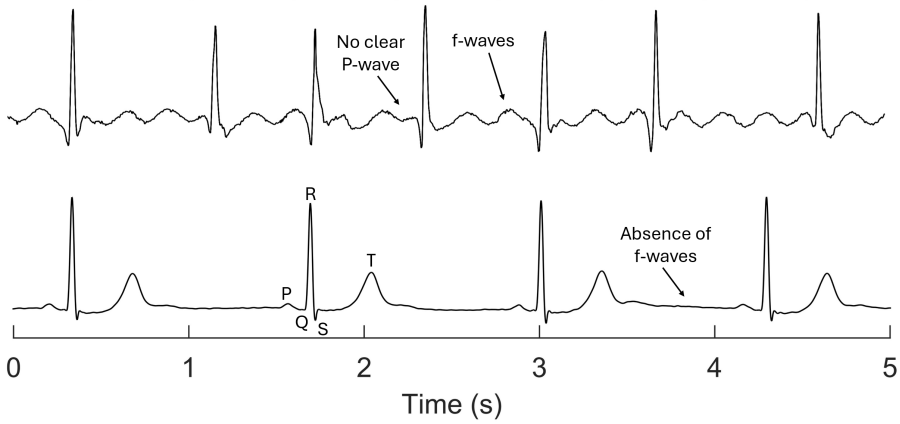

Figure 3.1: Characteristics of the ECG during AF (top) and during normal sinus rhythm (bottom), where the three main differences: RR interval irregularity, P-wave absence, and presence of f-waves, are seen.

is a basis for several AF-detection algorithms due to its ease and robustness of extraction from the ECG signal [57, 58]. Notably, the time series of intervals between consecutive heartbeats can also be extracted from the photoplethysmogram (PPG), often measured on the skin by smartwatches using a light source and photodetector combination. Because of this, recent years have seen a rise in the development of AF-detection algorithms based on PPG signals, with a focus on PPG measurements from smartwatches, often employing deep learning [59, 60, 61, 62].

3.2.1 Characterisation of f-waves

During normal sinus rhythm, the P-wave represents the depolarisation wave in the atria. However, due to the rapid and irregular electrical activity in the atria during AF, a distinct P-wave is absent. Instead, the ECG shows incessant f-waves. While the presence of f-waves is a vital indicator of AF, detailed f-wave characteristics can provide further insights into atrial electrical activity. Different techniques exist to estimate the dominant atrial frequency from the f-waves, such as using the dominant peak in the frequency spectrum [63], or using a model-based approach [64, 65]. *Papers I-III* of this thesis utilises a hidden Markov model for robustly tracking the dominant frequency of f-waves from the ECG signal [66]. Moreover, *Paper IV* uses the model-based approach presented in [64, 65] to gain high-resolution estimates of the f-wave frequency trend. However, these methods require QRS complex removal since f-waves have a significantly smaller amplitude compared to the QRS complex. Several

methods can achieve QRS removal, including average beat subtraction [67], adaptive filtering [68], blind source separation [69], and a voting scheme on four different template subtraction algorithms [70]. In all papers in this thesis, the QRS removal was performed using the commercial CardioLund ECG parser (`www.cardiolund.com`) which uses a spatiotemporal average beat subtraction approach.

3.2.2 Characterisation of RR Interval Series

The RR interval series serves as a useful representation of cardiac activity and is commonly represented as a time series plot or using a histogram. As shown in Figure 3.2b, the histograms of the RR interval series for normal sinus rhythm and AF differ substantially. The histogram during sinus rhythm exhibits a narrow distribution, whereas the histogram during AF is significantly more scattered. Hence, researchers can analyse data from different models or patients by comparing the number of data points in each bin [71].

Another visualisation method for the RR interval series is the Poincaré plot, a scatter plot depicting successive pairs of RR intervals. The Poincaré plot offers the ability to analyse non-linear aspects of the heart rate by capturing more dynamic features compared to histograms [51]. During normal sinus rhythm, the Poincaré plot shows a compact area where all points concentrate, contrasting with the more spread-out distribution observed during AF, as illustrated in Figure 3.2c.

Papers I-III of this thesis utilises a target function based on the Poincaré plot (see Section 5.3.3) to estimate model parameters, whereas *Paper IV* utilises the RR interval series. Additional methods for characterising the RR interval series during AF include autocorrelation, Shannon entropy, and root mean square of successive differences [1, 72, 73].

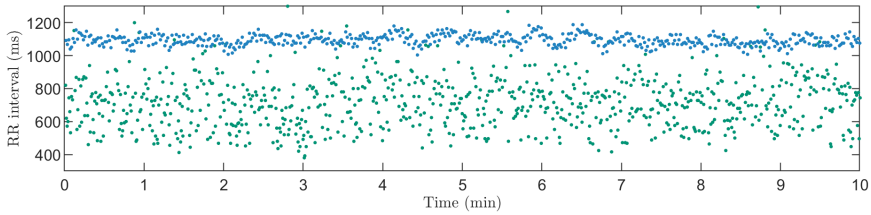

(a) RR interval series

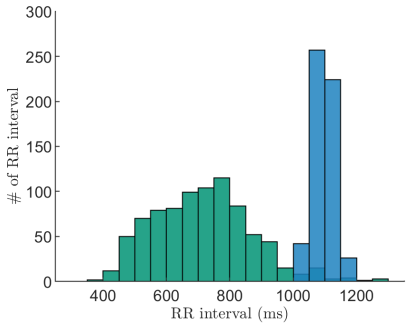

(b) Histogram of the RR interval series

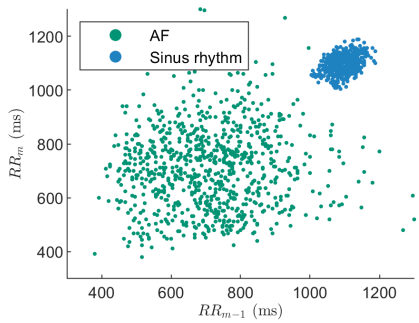

(c) Poincaré plot of the RR interval series

Figure 3.2: A comparison of the RR interval series (a), the histogram of the RR interval series (b), and the Poincaré plot of the RR interval series (c) during AF (green) and during normal sinus rhythm (blue) (data from the MIT-BIH AF Database) [74]. Reprint from [15].

3.3 Management of Atrial Fibrillation

Atrial fibrillation management focuses on three primary objectives. The first is preventing ischemic strokes through anticoagulation therapy, which does not directly impact AF itself [7]. The second objective targets heart rate control. This approach aims to achieve a normal heart rate during ongoing AF episodes, thereby improving patient quality of life and mitigating risks associated with other cardiac conditions, such as decreased ventricular contractile function. The third objective is rhythm control, which focuses on terminating or preventing AF episodes altogether. Rate control is recommended as the first-choice therapy for patients with no or minor AF symptoms whereas rhythm control is typically employed when rate control strategies prove ineffective or for patients with greater AF-related symptoms [7]. For this thesis and the included papers, rate control will be in focus.

3.3.1 Rhythm Control

Rhythm control includes restoration and maintenance of a normal sinus rhythm. Acute restoration can be achieved through either electrical cardioversion, utilising electrodes placed on the chest, or pharmacological cardioversion, using antiarrhythmic drugs. For pharmacological cardioversion in recent-onset AF, vernakalant [75], flecainide [76, 77], and propafenone [77] are recommended medications [7]. Long-term maintenance of sinus rhythm can be achieved through antiarrhythmic drugs – such as amiodarone [78] and dronedarone [79] – or catheter ablation. Catheter ablation performed by experienced teams has demonstrated superior efficacy compared to antiarrhythmic drugs [80]. This invasive procedure involves isolating the pulmonary veins and, in some cases, creating additional ablation lines within the atria. Nevertheless, long-term (3-5 years) success of catheter ablation varies considerably from 50 to 80% [81, 82], and estimation of catheter ablation success is difficult due to inconsistency in the definitions of success and wherever single or multiple catheter ablation procedures were performed [82].

3.3.2 Rate Control

Rate control is a cornerstone of AF treatment and is recommended for the majority of patients [7]. Even in cases where a high ventricular rate does not cause immediate discomfort, leaving it untreated can lead to heart complications such as reduced pumping capacity [7]. Several pharmacological options exist for rate control, including β-blockers, non-dihydropyridine calcium channel blockers, and digitalis. However, β-blockers and calcium channel blockers are recommended as first-line therapies [7].

β-blockers, commonly metoprolol or carvedilol, target β-1 receptors in the heart, effectively reducing the influence of the sympathetic nervous system and consequently lowering the heart rate. The general effect of β-blockers on the action potential is complex without any clear trends between different β-blockers [83]. Nevertheless, as detailed in Section 2.3, stimulation of β-1 receptors enhances inward calcium current via L-type channels, and blocking of these receptors decreases the conduction velocity in the AV node [34]. Furthermore, electrophysiological studies of the β-blocker metoprolol have demonstrated an increased AV nodal refractory period [84]. Additionally, the β-blocker carvedilol has been shown to prolong the effective refractory period in the atria during AF, reducing the frequency of impulses into the AV node, thereby reducing the heart rate [85].

Non-dihydropyridine calcium channel blockers, such as verapamil or diltiazem, prevent the opening of L-type calcium channels. This results in a weaker upstroke of the action potential in pacemaker cells and thereby a reduced conduction velocity within the SA and AV node cells, resulting in a lowering of the heart rate. Electrophysiological studies of verapamil and diltiazem have also demonstrated an increased AV nodal refractory period [86, 87].

Combination therapy employing β-blockers, calcium channel blockers, and digitalis is also used in some cases [88]. Notably, robust evidence remains limited regarding the most effective type and intensity of rate control treatment [89, 7]. Ablation of the AV node with pacemaker implantation is an option, but this is typically reserved as a last resort when drugs are ineffective [7].

In addition, the FP and SP of the AV node exhibit distinct electrophysiological behaviours, as stated in 2.2.2. Therefore, a difference in their response to medications is expected [90, 26, 91]. For instance, studies have shown that the β-blocker esmolol has a less pronounced effect on the anterograde refractory period of the SP compared to the FP [92]. In general, the detailed mechanisms governing AV nodal function remain under debate, and the precise physiological differences between the pathways relevant to drug effects are not fully understood [93].

Chapter 4
Cardiac Modelling

Over the years, researchers have developed numerous mathematical models of the human heart. Depending on their ultimate purpose, they range from whole-heart models to those focused on specific components such as the AV node. Some models aim to deepen our understanding of the heart's function, while others aim to identify patient-specific characteristics to guide personalised treatment selection. Since this thesis focuses on modelling the AV node, this chapter will mostly focus on models of the AV node.

This chapter begins with a broad overview of the field of cardiac electrophysiology modelling, in Section 4.1. Section 4.2 focuses on models of the AV node; exploring six different AV node models, the last being the model we propose in *Paper I*. This model is specifically designed to assess conduction delay and refractory period within the AV node during AF.

4.1 Cardiac Electrophysiology Models

We begin our exploration of cardiac electrophysiology modelling by focusing on cell models. Cell models delve into the electrical activity at the cellular level and model the interaction of ion channels within the cell membrane, which coordinates the action potential. As described in Section 2.1.1, the action potential plays a key role in the electrophysiology of the heart, heavily influenced by the interplay of Na^+, K^+, and Ca^{2+} channels. Consequently, cellular cardiac electrophysiology models often integrate representations of these ionic currents. Markov models and Hodgkin-Huxley models are common choices for this purpose [94, 95]. These models capture the dynamic voltage-dependent gating behavior of ion channels across the cell membrane [95]. By combining such models, researchers can create detailed representations of

the action potential. The physiological details of these models have increased greatly from the first computational model of a cardiac action potential by Noble in 1962 [96], to now include e.g. modelled β-adrenergic signalling and updated formulations for the L-type Ca^{2+} channel current [94].

It is possible to connect multiple cell models into larger structures. This can be achieved using a bidomain model, a mathematical model using partial differential equations to describe the membrane potential and ionic currents of a group of cells organised in a complex structure [97]. By combining multiple cell models, larger structures of the heart such as tissues or even the whole heart can be modelled, with varying physiological detail [98]. These models combine anatomical representations of the atria, ventricles, and conduction system, and allow for investigation of complex phenomena of various structures. These types of cardiac models are particularly valuable for studying arrhythmias such as AF [99]. However, a detailed description of the whole heart leads to a large number of parameters and degrees of freedom to describe the models (possibly several million). This leads to high computational demand and often precludes the models from using the patient-specific optimisation of model parameters used in this thesis [99]. While some studies have explored patient-specific estimation in whole-heart models, this will always require some assumption, since it is generally impossible to reliably determine the huge number of degrees of freedom that these models contain.

Therefore, larger structure cardiac models with less physiological detail and fewer parameters have been developed, such as the eikonal models used to efficiently map the cardiac activation [100, 101] and repolarization [102]. These types of models have been used to simulate electrograms and ECGs in human whole hearts [102]. As an example, whole-heart models are used to guide catheter ablation procedures for AF by simulating electrical wave propagation and identifying optimal ablation targets [103, 104]. Another way to reduce computational complexity is to focus on specific regions of the heart relevant to the research question, such as the AV node. These techniques for reducing the complexity are not mutually exclusive. As an example, the model proposed in *Paper I* describes the AV node as a network of simplified cell models, hence describing a specific region with reduced level of physiological detail.

4.2 AV Node Models

Several AV node models have been created, ranging in spatial resolution from zero-dimensional lumped structures to one-dimensional networks with varying complex-

ity levels tailored to specific intents. This section presents a summary of five AV node models relevant to the model proposed in *Paper I* either by having a one-dimensional structure [105, 106, 107], incorporating interaction between the FP and SP [105, 106, 108], or by having similar purpose of individual assessment of AV node properties using ECG recordings [109]. Nevertheless, models of the AV nodal recovery curve have long exited [110] and evolved to incorporate facilitation[1] and fatigue [111, 112] before including concealed conduction [113, 114]. These types of models have successfully been used to study atrial tachyarrhythmias such as AF [115, 116].

4.2.1 Inada et al.

Inada et al. developed a biophysically detailed action potential model including the SA node, right atrium, and AV node of a rabbit heart [105]. This one-dimensional multicellular model represents the heart as a network of cell models. For the AV node specifically, the model utilises the three distinct cell types described in Section 2.2.2; the atrio-nodal cells (beginning), nodal cells (middle), and nodal-His cells (end), as shown in Figure 4.1. Each cell type is based on action potential recordings from rabbit hearts and incorporates various ion currents crucial for electrical activity. A system of 26 nonlinear ordinary differential equations governs the action potential dynamics within each cell. The model replicates the dual pathway physiology of the AV node with 200 sub-models representing the SP and 150 sub-models representing the FP. To simulate AF, the model introduces stimuli with random intervals into the atrial cells preceding the AV node.

Figure 4.1: A schematic representation of the AV node model presented in [105].

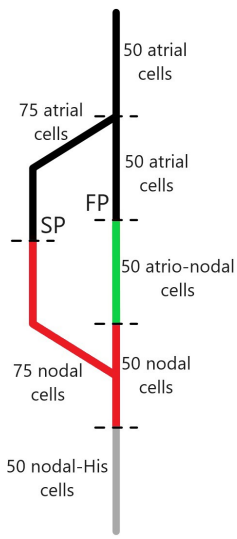

This comprehensive model captures the physiological characteristics of the AV node tissue and has been used to analyse various aspects of its function, including the effects of calcium channel blockers and AV node pacemaking activity.

[1] Increasing the excitability or responsiveness of the AV node to incoming electrical signals.

4.2.2 Ryzhii et al.

Ryzhii et al. proposed a one-dimensional representation of the conduction system of the rabbit from the SA node until the bundle of His comprising a total of 33 cells [106], where all cells are based on the Aliev-Panfilov model [117]. Compared to the one-dimensional AV node model proposed by Inada et al. [105], this formulation offers a computationally more efficient method to capture the essential electrophysiological behaviours of the AV node, such as dual pathway physiology. It has been shown to replicate normal sinus rhythm, AV node automaticity, and the filtering of rapid atrial rhythms seen in AF. The model was designed to be used as a stand-alone model, as a part of a three-dimensional model of the atrial, or as a part of a whole-heart model.

4.2.3 Lian et al.

Lian et al. proposed an AV node model for investigating ventricular pacing, conduction delays, and refractoriness within the AV node during AF [107]. This four-component model incorporates an AF generator, an AV junction component, a ventricular component, and an optional pacing electrode, as shown in Figure 4.2. The AF generator utilises a Poisson process, a common approach for simulating the arrival of impulses at the AV node. The Poisson process is characterised by a single parameter, λ, representing the average rate of incoming impulses. The AV junction is modelled as a zero-dimensional lumped structure, characterising several properties of the AV node, such as the refractory period and conduction delay. An exponential recurrence relation describes the dynamics of recovery and delay within the AV junction. The ventricular components account for the influence of the ventricles on the AV junction through retrograde waves. Finally, the optional pacing electrode allows for investigating the effects of external pacing on the AV node. All four components are interconnected, enabling them to influence the behavior of each other.

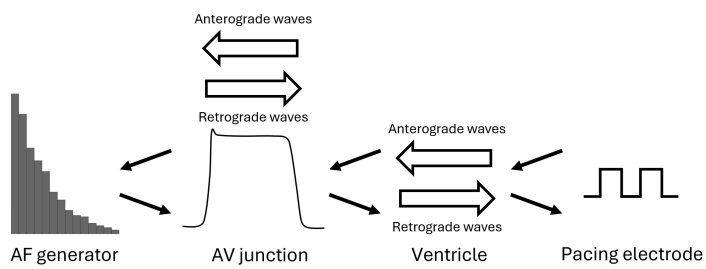

Figure 4.2: A schematic representation AV node model presented in [107].

This model has been used to study the impact of conduction properties and AF rate on the ventricular response during AF, as well as the electrotonic modulation in the AV junction. While capable of replicating realistic RR series, the model lacks spatial resolution in the AV node and dual pathway physiology due to the lumped structure of the AV junction.

4.2.4 Climent et al.

Climent et al. focused on modelling the conduction delay of the FP and SP within the AV node during AF using a zero-dimensional model [108]. To represent the conduction delay in each pathway, the model employs the exponential function seen in Equation 4.1,

$$A_3H_3 = AH_{min} + \beta \cdot exp(-(A_2A_3 - A_2H_2)/\tau_{rec}), \tag{4.1}$$

to calculate a test conduction time A_3H_3; where AH_{min} is the minimum observed time for an atrial impulse to reach the His bundle; A_2A_3 is the coupling interval between a conditioning atrial stimulus and a test-stimulus; A_2H_2 is the conditioning stimulus conduction time; β is a modulating factor; and τ_{rec} the AV node recovery period. These parameters were determined using data obtained from in vitro pacing experiments on rabbit hearts. To validate the performance of the model during AF, irregularly distributed AA intervals as input for both the model and the in vitro preparations were used.

Moreover, the model captures concealed conduction by calculating the conduction delay for both pathways. The pathway with the shorter delay retrogradely invades the other. This model has advanced our understanding of the complex and poorly understood characteristics of conduction time and dual pathway physiology within the AV node during arrhythmias like AF.

4.2.5 Corino et al.

Corino et al. proposed a statistical model specifically designed to assess AV node electrophysiology properties from ECG data during AF, with further development reported in subsequent works [109, 118, 119]. This zero-dimensional lumped model, shown in Figure 4.3, incorporates key physiological features such as concealed conduction, relative refractoriness, and dual pathways. The model simulates incoming atrial impulses to the AV node using a Poisson process. Each impulse can trigger ventricular

activation through propagation via the SP with a probability α, trigger activation via the FP with a probability of $1 - \alpha$, or be blocked due to the refractory state of the AV node (τ_1 in the SP, τ_2 in the FP). The refractory period is modelled by a combination of deterministic and stochastic components. The deterministic component is split into two parts, representing the two pathways within the AV node, while the stochastic component is assumed to be uniformly distributed. The mean arrival rate of atrial impulses is estimated from the atrial activity extracted from the ECG using spatiotemporal QRST cancellation [67]. The remaining model parameters are estimated by maximising a log-likelihood function.

This model has demonstrated a high degree of accuracy, replicating 88% of RR interval series histograms when compared to empirical data. However, it is limited by the lumped nature of the model, since several AV node characteristics are grouped together, limiting the interpretation of these parameters.

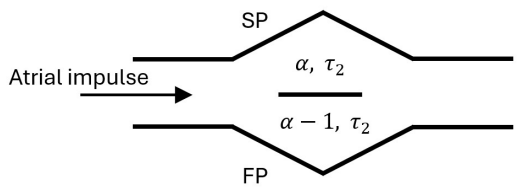

Figure 4.3: A schematic representation AV node model presented in [118].

4.2.6 Network Model of the AV Node

The event-based phenomenological model proposed in *Paper I* is used in *Papers I-IV*. It has separate parameters for the refractory period and the conduction delay, making it possible to study both pathways. It is based on a previous model presented in [71]. The model is similar in structure to the one-dimensional AV node models proposed by Inada et al. [105] and Ryzhii et al. [106], although, vastly more computationally efficient. Similar to the model proposed by Corino et al. [109], the purpose of this model is to assess the electrophysiology properties of the AV node during AF based on ECG recordings.

The model depicts the AV node as a network of 21 interconnected nodes, as shown in Figure 4.4. These nodes are categorized into three functional groups; FP, SP, and a coupling node. Each pathway is represented by ten individual nodes, corresponding to a localised region within the AV node. An impulse arriving at a node can either propagate to all its neighbouring nodes after a conduction delay or be blocked if the

node is in its refractory period. The refractory period and conduction delay for the pathway node i is updated for each incoming impulse n according to Equation 4.2, 4.3 and 4.4,

$$R_i(n) = R_{min} + \Delta R(1 - e^{-\tilde{t}_i(n)/\tau_R}) \tag{4.2}$$

$$D_i(n) = D_{min} + \Delta D e^{-\tilde{t}_i(n)/\tau_D} \tag{4.3}$$

$$\tilde{t}_i(n) = t_i(n) - t_i(n-1) - R_i(n-1), \tag{4.4}$$

where $t_i(n)$ is the arrival time and $\tilde{t}_i(n)$ the diastolic interval preceding the impulse. A negative value of $\tilde{t}_i(n)$ indicates the node is currently in its refractory phase, consequently blocking any incoming impulses. The refractory period and conduction delay for each pathway is defined by three parameters each: a minimum value (R^{FP}_{min} and R^{SP}_{min} for the refractory period, D^{FP}_{min} and D^{SP}_{min} for the conduction delay), a maximum prolongation (ΔR^{FP}, ΔR^{SP}, ΔD^{FP} and ΔD^{SP}), and a time constant (τ^{FP}_R, τ^{SP}_R, τ^{FP}_D, and τ^{FP}_D). Notably, the parameters are identical for all nodes within a pathway. However, due to the varying arrival times of impulses at each node, the actual values of the refractory period and conduction delay will differ between nodes at any given time. Furthermore, the coupling node represents the connection between the end of the AV node and the bundle of His, the bundle of His itself, and the Purkinje fibers. Here, both the refractory period and conduction delay are set to constant values.

Impulse generation can be modelled by a Poisson process with a mean arrival rate (λ) derived from the ECG (as in *paper I-III*), or extracted from endocardial recordings (as in *Paper IV*). These impulses propagate throughout the network in an event-based manner, allowing for efficient computation using a modified version of Dijkstra's algorithm [120]. Using a network model allows for several interesting properties besides the model parameters themself to be studied, such as the amount of concealed conduction and the ratio of impulses propagating through the different pathways.

Each time a heartbeat is simulated with the model, the refractory period and conduction delay for each node activation are calculated using Equation 4.2 and 4.3, respectively. Thus, a vector of the refractory periods and conduction delays is generated for the nodes in the FP and the SP. The median of these vectors can be used to estimate the refractory period and conduction delay of each pathway, instead of the 12 model parameters. This is utilised in *Papers III and IV* to study the properties of the AV node, as a contrast to only studying the changes in parameter values, facilitating interpretation of the results.

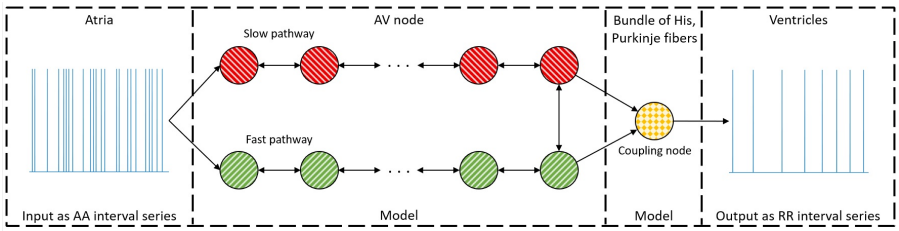

Figure 4.4: A schematic representation of the network model, divided into the slow pathway (red), fast pathway (green), and coupling node (yellow). The input is created using a Poisson process, representing atrial activation, and the output represents ventricular activation [1].

Chapter 5
Model Fitting and Parameter Estimation

Having established a mathematical model, the next step towards individual estimation of AV node properties involves fitting the model parameters based on clinical measurements. This can be achieved by finding the optimal value (minimum or maximum) of a target function quantifying the difference between model output and clinical measurements.

This chapter starts with discussing target functions, in Section 5.1. The chapter continues with discussing the importance of quantifying uncertainty and different methods to achieve this in Section 5.2. Building on the previous sections, Section 5.3 describes several optimisation algorithms, where specific focus is placed on the genetic algorithm, as *Papers I-III* utilises it. This chapter closes with a short section on mixed-effect modelling, useful for understanding the results of *Paper II*.

5.1 Target Functions

In order to estimate model parameters, a function quantifying how closely the model output aligns with clinical measurements needs to be defined. This function is known as the target function, and its inverse is called the error function. How the target function is defined determines the resulting fit to clinical data, and thus what truly is modelled. Therefore, a target function should preferably capture all relevant information about a system. However, a more complex target function often results in optimisation difficulties, hence a trade-off between complexity and ease of optimisation exists.

Target functions can be categorised into probabilistic target functions, quantifying the difference using probability theory, and heuristic target functions, using a more pragmatic quantification of the differences. Generally, heuristic target functions are more flexible and can be tailored to a specific problem. As an example, we proposed to use a heuristic target function based on the Poincaré plot (see Section 3.2.2) in *Paper I*, where the differences between Poincaré plots of a measured and simulated RR interval series are quantified. This increased the complexity of a previously used target function for the AV node model based on the histogram of the RR series [121], to also include dynamics of the RR series. In turn, this necessitated a more complex optimisation algorithm, highlighting the trade-off between complexity and ease of optimisation.

Using a probabilistic target function can be challenging since setting up a probabilistic representation of the problem is often difficult. Nevertheless, Bayes' theorem provides a mathematical expression for a probabilistic representation including the relationship between prior knowledge, observed data, our confidence in the model, and the resulting posterior distribution, as shown in Equation 5.1 [122].

$$p(\boldsymbol{\theta}|y) = \frac{p(y|\boldsymbol{\theta}) \cdot p(\boldsymbol{\theta})}{p(y)} \tag{5.1}$$

Here, $\boldsymbol{\theta}$ represents some model parameters and y represent observed data. Furthermore, in the case where only a single model structure is considered, the evidence $p(y)$ acts as a normalisation constant. The likelihood function, $p(y|\boldsymbol{\theta})$, describes the probability of observing y given $\boldsymbol{\theta}$. The prior probability distribution, $p(\boldsymbol{\theta})$, encodes the initial belief about possible parameter values. By applying Bayes' theorem, the prior beliefs are updated using the data, resulting in the posterior distribution $p(\boldsymbol{\theta}|y)$, which can be used as a probabilistic target function, relevant for the work in *Paper IV*. Using $p(\boldsymbol{\theta}|y)$ as a target function and searching for its maximum results in a so-called maximum a posteriori estimate of $\boldsymbol{\theta}$. Similarly, a maximum-likelihood estimate is obtained using the same approach and setting $p(\boldsymbol{\theta})$ to one. However, a more common approach when using a Bayesian formulation of the target function is to quantify aspects of $p(\boldsymbol{\theta}|y)$ such as the mode or credibility regions, as is done in *Paper III-IV*. This can be used as a tool for uncertainty quantification, which will be discussed in the next section.

5.2 Uncertainty Estimation

A crucial aspect of model parameter estimation lies in quantifying their associated uncertainty. Without a proper measure of uncertainty, it is difficult to assess the quality

and reliability of the estimated parameters. This uncertainty encompasses both the inherent variability in the parameter estimation process and the impact of the parameters on the model output.

A straightforward approach for understanding the uncertainty involves running the optimisation algorithm multiple times and analysing the spread of the resulting parameter values, as employed in *Paper I*. However, this approach is computationally expensive and does not theoretically guarantee a reliable uncertainty estimate.

To derive a more nuanced interpretation for a better understanding of a specific parameter's influence on the model output, sensitivity analysis is often employed. The most common and basic approach is the one-at-a-time method, where each parameter is individually perturbed while all others remain fixed [123]. While this technique can provide some insights, it neglects the potential influence of parameter interactions. A more robust alternative is variance-based sensitivity analysis, with Sobol's method as a prominent example. This method offers a global sensitivity analysis approach [124]. Sobol's method allows for the calculation of "total-effect" indices, which quantify the contribution of each parameter to the overall variance of the model output, including the variance arising from interactions with other parameters. For models with analytical tractability, these indices can also be calculated analytically, but commonly Monte Carlo simulations are used for estimation [125]. *Paper II* utilised a variation of Sobol's method to estimate parameter uncertainty, focusing the sensitivity analysis on a limited region around the optimal parameter set.

However, Sobol's method does not directly quantify uncertainty but rather focuses on assessing the sensitivity of the output to changes in the inputs. Probability distributions of the model parameters ($p(\boldsymbol{\theta}|y)$ seen in Equation 5.1), on the other hand, provide a comprehensive picture of the uncertainty. However, quantifying the probability distribution can be challenging, and methods approximating $p(\boldsymbol{\theta}|y)$ with Markov chain Monte Carlo based methods such as the Metropolis–Hasting algorithm [126], Gibbs sampling [127], and particle filters [128] are often used (e.g. in *Paper IV*). To use these methods, $p(y|\boldsymbol{\theta})$ needs to be evaluable. If it is not possible to evaluate $p(y|\boldsymbol{\theta})$, the approximate Bayesian computation (ABC) algorithm (see Section 5.3.6) can instead be used to approximate $p(\boldsymbol{\theta}|y)$, as was done in *Paper III*. However, a model for generating data and sufficient statistics[1] needs to be defined to use the ABC algorithm, which is not always possible. Since these methods provide an approximation of the entire posterior distribution $p(\boldsymbol{\theta}|y)$, they can be used to obtain a maximum a posteriori estimate of the model parameters as well as an associated uncertainty.

[1] A summary of the data that are as informative as the entire dataset itself.

5.3 Optimization Algorithms

While the simplest form of optimisation reduces to finding zeros of the derivative of an analytically tractable function, most real-world problems cannot be described using an analytically tractable function. Instead, different optimisation algorithms are needed to find the optimum for heuristic and probabilistic target functions lacking an analytic solution. Below we describe six important algorithms: the gradient descent algorithm, particle swarm optimisation, the genetic algorithm, the particle filter, as well as the smoothing algorithm for approximating $p(\boldsymbol{\theta}|y)$ when $p(y|\boldsymbol{\theta})$ can be evaluated, and the ABC algorithm for approximating $p(\boldsymbol{\theta}|y)$ without directly evaluating $p(y|\boldsymbol{\theta})$.

An additional layer of complexity arises when optimisation occurs in a dynamic environment. Here, the clinical measurements, and consequently the optimal solution, changes over time. The challenge becomes not only finding the optimum but also to track it as the environment evolves. This is known as a dynamic optimisation problem, which is particularly relevant for estimating changes in model parameters over time, offering valuable insights in many real-world scenarios such as in *Papers II-IV*. A critical challenge when tracking the optimum of the target function in a dynamic optimisation lies in maintaining diversity within the optimisation algorithm. In this work, this translates to diversity in the collection of candidate solutions an optimisation algorithm explores. Here, diversity refers to the variety of parameter sets explored during the search process. Loss of diversity can hinder the ability of the algorithm to find new optima as the target function changes. As a consequence, a significant research focus has been placed on developing methods to maintain population diversity through clever replacement strategies for candidate solutions [129, 130], specifically relevant for *Paper II* and *III*. Solving a dynamic optimisation problem can be achieved using any of the presented algorithms.

The choice of optimisation algorithm depends heavily on the specific problem and the target function at hand. The vast number of optimisation algorithms makes it impossible to cover them all in this thesis. Therefore, this work will focus on and discuss a selection of approaches particularly relevant to optimising parameters within AV node models.

5.3.1 Gradient descent

Perhaps the most widely known optimisation algorithm is gradient descent. It leverages the concept of the gradient, or an approximation of it, to iteratively minimise the error function [131]. In each step, the gradient of the target function is evaluated at the current parameter vector. This gradient indicates the direction with the steepest

descent, guiding the next step of the algorithm towards the minimum of the error function. The update rule for gradient descent is captured by Equation 5.2:

$$\boldsymbol{x}_{n+1} = \boldsymbol{x}_n - \boldsymbol{\gamma}\nabla F(\boldsymbol{x}_n), \tag{5.2}$$

where $\boldsymbol{x}_n$ represents the current parameter vector, $\boldsymbol{x}_{n+1}$ the updated parameter vector after the step, $\nabla F(\boldsymbol{x}_n)$ denotes the gradient of the error function evaluated at $\boldsymbol{x}$, and $\boldsymbol{\gamma}$ the step size, controlling the magnitude of the update step. The simplicity and effectiveness of gradient descent make it a valuable tool when the gradient can be readily calculated. However, it suffers from two main drawbacks. First, it is susceptible to getting trapped in local minima, potentially leading to suboptimal solutions. Hence, the result can be highly dependent on the initial choice of parameter values. Second, the selection of the step size is crucial. A value that is too small can lead to slow convergence, while a value that is too large might cause the algorithm to overshoot the optimum entirely, hindering convergence.

5.3.2 Particle swarm optimisation

Particle swarm optimisation is inspired by swarm intelligence, particularly the movement and social interaction observed in flocks of birds or schools of fish [132, 133]. In the algorithm, a swarm of particles explores the search space, where each particle represents a set of model parameters to be estimated. The algorithm has found applications in various fields in recent years, including optimising the efficiency of solar power towers [134] and aiding decision-making in marine oil spill responses [135]. The particle swarm optimisation algorithm can define different subsets within the search space or among the particles themselves, called topologies. Each particle explores the space independently, guided by its best-found solution and by the best-found solution of its assigned topology; evaluated on the target function. The update rule for the position of a particle is calculated by Equation 5.3.

$$\boldsymbol{v}_{n+1} = w_1\boldsymbol{v}_n + w_2\boldsymbol{r}_1(\boldsymbol{p} - \boldsymbol{x}_n) + w_3\boldsymbol{r}_2(\boldsymbol{g} - \boldsymbol{x}_n). \tag{5.3}$$

Here, $\boldsymbol{v}_n$ represents the velocity of the particle in the previous step; $\boldsymbol{p}$ represents the best-found position of the particle; $\boldsymbol{g}$ the best position found by any particle in the current topology; $\boldsymbol{r}_1$ and $\boldsymbol{r}_2$ are random vectors introduced for stochasticity; w_1, w_2, w_3 are weighting factors that control the influence of previous velocity, the best-found solution of the particle, and the topological best solution, respectively; $\boldsymbol{v}_{n+1}$ represents the velocity update for the next step; and $\boldsymbol{x}_n$ denotes the current parameter set of the particle. Following this velocity update, the position of the particle is calculated using Equation 5.4,

$$\boldsymbol{x}_{n+1} = \boldsymbol{x}_n + \boldsymbol{v}_{n+1}. \tag{5.4}$$

Although versatile, particle swarm optimisation is not guaranteed to find a maximum of the target function. However, the broadness of the search makes it less likely to get stuck in local optima compared to the gradient descent and the genetic algorithm. The nature of the algorithm makes it very suitable for use on dynamic optimisation problems since the particles will move around the error surface when the surface is changing, gradually improving on previously found solutions for slowly changing error surfaces [136, 137].

5.3.3 Genetic algorithm

The genetic algorithm is inspired by biological evolution, specifically Darwin's concept of natural selection [138, 139]. It incorporates elements of mutation, crossover, and selection to achieve optimisation. A genetic algorithm operates on a population of individuals, where each individual represents one set of model parameters. These individuals are here denoted $\boldsymbol{x}_{n,i}$, where n refers to the generation and i indicates a specific individual within a population of I individuals. The initial population is generated randomly. Each of the I individuals is subsequently evaluated using a target function, often referred to as a fitness function in this context. The next generation of individuals is then created through a combination of selection, crossover, and mutation. A pseudocode for a genetic algorithm is shown in Algorithm 1.

Selection mimics natural selection by choosing two "parents" from the existing population. Two common selection methods are tournament selection and roulette wheel selection [140]. In tournament selection, a small group of individuals is randomly chosen, and the individual with the highest fitness score is selected with a certain probability of reproduction. In roulette wheel selection, each individual has a probability of selection that is directly proportional to their fitness score. This means individuals with higher fitness scores occupy a larger portion of the figurative roulette wheel and are therefore more likely to be chosen as parents. Crossover mimics breeding in nature. It combines genetic information from two parents by swapping parts of their chromosomes (parameter values in our case) to create a new offspring for the next generation [141]. This exchange of genetic material allows for the creation of novel solutions that might not have been present in the original population. Mutation, on the other hand, introduces random alterations in the genetic makeup of an individual, promoting diversity and potentially leading to the exploration of new regions in the search space [142]. This interplay between selection, crossover, and mutation drives the population towards improved solutions over successive generations.

Algorithm 1 Pseudocode for a genetic algorithm algorithm

```
Initialization (n=0):
Randomly generate x_{0,i}
while not terminated do
    Evaluate x_{n,i}
    for i = 1:I/2
        Select two individuals from x_{n,i}
        Create two new individuals using crossover (Figure 5.1a)
        Mutate the two new individuals (Figure 5.1b)
    end
    Evaluate termination criteria
    n = n + 1
end
```

An example of selection, crossover, and mutation is illustrated in Figure 5.1. Here, two individuals, $\boldsymbol{x}_{n,i}$ and $\boldsymbol{x}_{n,j}$, are first selected with a probability based on their fitness values. Following selection, two crossover points, c_1 and c_2, are randomly chosen between 1 and the total number of parameters within the individuals (Figure 5.1a). The parameter values between these crossover points are then swapped between the parents to create two offspring, $\boldsymbol{x}_{n+1,i}$ and $\boldsymbol{x}_{n+1,j}$. Further, each parameter within these offspring has a probability of being mutated, as depicted in Figure 5.1b. This process of creating new individuals through selection, crossover, and mutation continues until the next generation $(n+1)$ reaches the same population size as the previous generation. The entire process iterates until a termination criterion is met. Common termination criteria include finding an individual with a fitness value exceeding a predefined threshold, reaching a fixed number of generations, or observing no significant improvement in the best solution over successive generations [143].

Genetic algorithms have been successfully applied to solve complex problems such as designing specialised antennas [144] or predicting the inflation rate [145]. As with particle swarm optimisation, a genetic algorithm cannot guarantee to find the optimal solution. Nevertheless, the ability of the population to adapt to changing environments makes genetic algorithms well-suited for dynamic optimisation problems, where the fitness landscape itself evolves over time, similar to how changes in climate cause real-world animals to evolve. Due to selection and mutation, the individuals in a genetic algorithm can drastically change their parameter values from one generation to the next, making it suitable for tracking optimum in rapidly changing error surfaces in dynamic optimisation problems [136, 137].

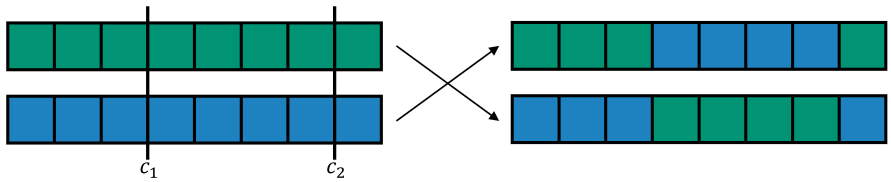

(a) Two point crossover

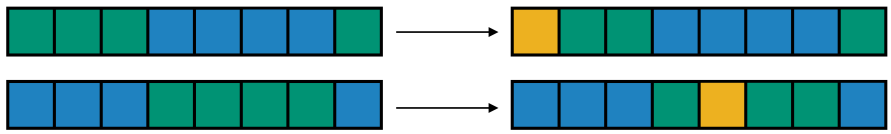

(b) Mutation

Figure 5.1: Figure (a) depicts a schematic representation of crossover in a genetic algorithm, where two individuals (left) are recombined to create two offspring (right). Following this crossover operation, Figure (b) shows a mutation event affecting the offspring individuals.

5.3.4 Particle filters

Using a probabilistic target function (see Section 5.1), it is possible to approximate the posterior probability distribution ($p(\boldsymbol{\theta}|y)$) from the optimisation algorithm. For linear state-space systems with Gaussian noise, the Kalman Filter can be used for parameter estimation [146]. However, this is not the case for the AV node model presented in *Paper I*. Instead, a particle filter can be used to approximate the solutions for the so-called filtering problem – estimating the posterior distribution ($p(\boldsymbol{\theta}|y)$) of the model parameters ($\boldsymbol{\theta}$) based on past and present observations (y).

Particle filters are a type of Monte Carlo method used to approximate $p(\boldsymbol{\theta}|y)$ in potentially non-linear and non-Gaussian state-space systems [128, 147]. Particle filters work by approximating the posterior probability distribution of the system state using a set of weighted particles. These particles represent possible states of the system over time, and their weights reflect how well they agree with the observed data. Using the model presented in *Paper I*, one particle represents one set of model parameters.

The particle filter algorithm can be described by four phases: initialisation, weighting, resampling, and propagation, illustrated in Figure 5.2. Initialisation deals with creating a set of particles representing the prior probability distribution of the system state. The weight of each particle is then updated based on how well it aligns with the latest observation using a probabilistic target function. Each particle is then resampled with

replacement, favouring those with higher weights. Lastly, each particle is propagated forward in time based on a defined dynamics model, describing the system and process noise. These steps are repeated for each new observation to update the posterior distribution. By iteratively executing these steps, the particle filter provides an approximate solution for the filtering problem, allowing for the estimation of system states and their associated uncertainties.

Particle filters have previously been used for cardiac applications such as atrial flutter detection [148], to robustly track heart rate [149], and to automatically annotate ultrasound videos of the fetal heart [150]. For *Paper IV* in this thesis, a particle filter is used to estimate the AV node properties for each heartbeat using a normal distribution centred at the time of a measured heartbeat as the target function.

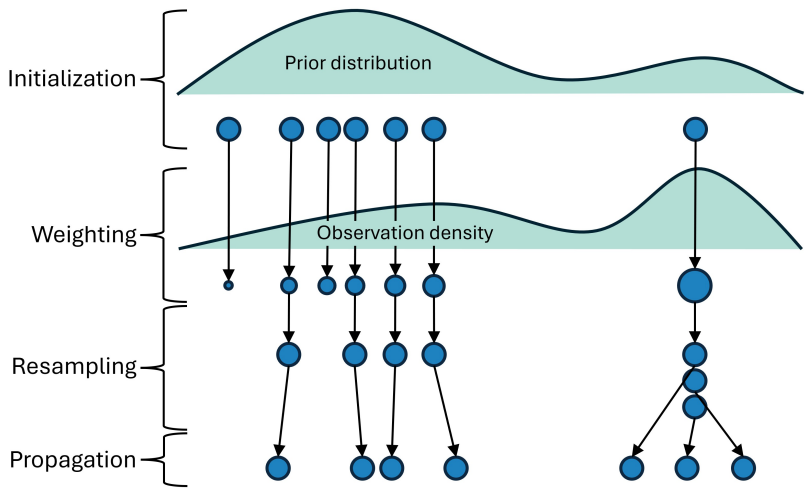

Figure 5.2: The four phases of a particle filter, where the weight of the particles is represented by their size.

5.3.5 Smoothing algorithm

While particle filters address the filtering problem using only past and current observations, smoothing algorithms aim to address the smoothing problem. This estimation incorporates information from both past and *future* observations. Smoothing algorithms become particularly useful when the complete time series of observations is available, and insights into past states might be valuable.

A common smoothing algorithm used in conjunction with particle filters is the forward filtering backward sampling algorithm [151, 152]. This algorithm operates in two passes, the forward and backward pass. The forward pass utilises a standard particle filter to approximate the solutions to the filtering problem for each observation. In the backward pass, a particle is selected from the last observation, based on its weight, and propagated backward in time to the position of one of the particles in the previous observation. Which previous particle that gets selected is based on its original normalised weight (W) in the forward pass, and on the likelihood that the selected particle ($\boldsymbol{\theta}_{t+1}$) was created from the previous ones ($\boldsymbol{\theta}_t$), according to Equation 5.5.

$$\hat{w}_t = W_t \; p_{t+1}(\boldsymbol{\theta}_{t+1}|\boldsymbol{\theta}_t). \tag{5.5}$$

Here, $\hat{w}_t$ is the updated weight at time t, W_t is the original normalised weight at time t, and p_{t+1} denotes the likelihoods that $\boldsymbol{\theta}_{t+1}$ was created from $\boldsymbol{\theta}_t$. Thus, p_{t+1} is the probabilistic target function used in the forward pass (particle filter).

This selecting of a particle and updating of weights is continued for all observations, starting at the last iteration and going backward, to create one entire state trajectory, encompassing the information from past and current observations via the forward pass, and information from future observations via the backward pass. Repeating this process multiple times thus generates an approximate solution for the smoothing problem. As for the particle filter, the target function for a smoothing algorithm also needs to be described as a probability density function. For this thesis, the smoothing problem is solved using a smoothing algorithm in *Paper IV*.

5.3.6 Approximate Bayesian Computation

The ABC algorithm can be used to approximate the posterior probability distribution using a heuristic target function. It provides a framework for approximating the posterior distribution ($p(\boldsymbol{\theta}|y)$) for any target function, as long as the model can generate simulated data [153, 154] and sufficient statistics can be defined. The core idea behind ABC involves comparing simulated data from a model with observed data (y) using a target function (or distance metric in ABC terminology). The algorithm works iteratively. First, data is simulated from the model using a prior distribution ($p(\boldsymbol{\theta})$) for the parameters, as shown in Figure 5.3. Then, the target function is evaluated for each simulation. Based on the results and a predefined threshold, parameter sets that generate simulated data closely resembling the observed data are retained, while the rest are discarded. The posterior distribution of the parameters is updated based on the retained parameter sets. By iteratively performing this process while updating the prior distribution with the previous posterior distribution and iteratively adjusting

the threshold, ABC gradually builds an approximation of the posterior distribution of the parameters.

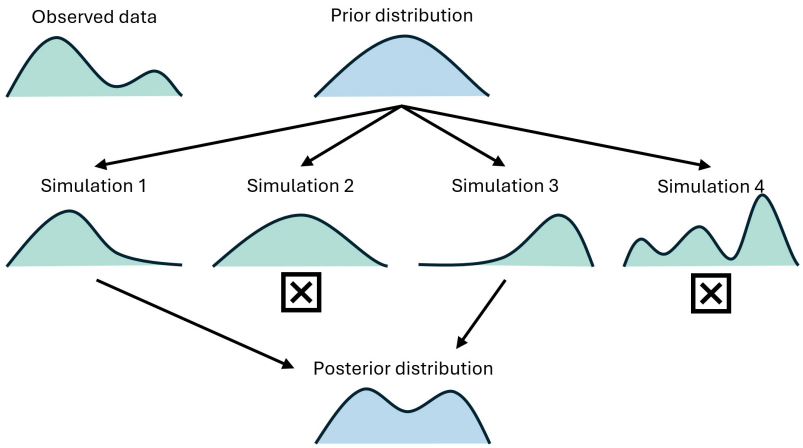

Figure 5.3: One iteration of the ABC algorithm. The distributions in the figure represent the observed and simulated data.

5.4 Mixed-effect Modeling

Estimating parameters in a dynamic optimisation problem leads to estimated model parameter trends, thus a time series of the model parameters. Analysing these trends by fitting them to a model that describes the parameter behavior over time can be valuable. When dealing with biomedical data, which frequently involves multiple patients and drugs, the mixed-effects model structure becomes particularly relevant due to its ability to account for fixed and random effects [155]. A linear mixed-effects model was employed in *Paper II* to estimate the drug-dependent differences in circadian variation within the parameter trends.

A mixed-effects model allows for the separation of the overall drug effect on a population (described by the fixed effects) from the individual response of each patient (captured by the random effects). A linear mixed-effects model can be mathematically represented by Equation 5.6,

$$\boldsymbol{y} = \boldsymbol{X}\boldsymbol{\beta} + \boldsymbol{Z}\boldsymbol{u} + \boldsymbol{\epsilon}, \tag{5.6}$$

where $\boldsymbol{y}$ is the known vector of observations, $\boldsymbol{\beta}$ is the unknown vector of fixed effects, $\boldsymbol{u}$ is the unknown vector of random effects, $\boldsymbol{\epsilon}$ is the unknown vector of random errors,

and $\boldsymbol{X}$ and $\boldsymbol{Z}$ are the known design matrices relating the observations to the fixed and random effects, respectively. Moreover, mixed-effect models have their own set of specialised optimisation algorithms, which the interested reader can find detailed information about in [156, 157].

Chapter 6
Summary of Papers

The four papers included in this thesis address the three aims stated in Section 1.2.

To develop a mathematical model of the AV node that accounts for its electrophysiological properties, is capable of replicating its behaviour during AF, and which computational efficiency allows for patient-specific parameter estimation (aim 1) is addressed in *Paper I*, where a model of the AV node is presented.

To set up a framework for reliable estimation of model parameters based on ECG recordings (aim 2) is addressed in *Papers I-IV*. All frameworks in the included papers are used to estimate the model parameters yielding results with varying degrees of temporal resolution and interoperability. In general, increasing the temporal resolution results in a larger uncertainty in the estimate, and with a larger uncertainty comes an increasing demand to quantify the uncertainty in order to evaluate the reliability of the estimate. The model parameters in *Paper I* are estimated from 15-minute ECG segments and the reliability was analysed by running the framework 200 times for each simulated patient. In *Paper II*, we estimated 24-hour trends of the model parameter, with a resolution of one sample per 1000 RR intervals. Additionally, a variant of Sobol's method [124] was used to derive the uncertainty for each estimated parameter. Further, in *Paper III* the uncertainty was more accurately quantified using the ABC algorithm to approximate the posterior distribution of the model parameters to better quantify the robustness of the estimates. Lastly, in *Paper IV*, a particle filter was used to provide beat-to-beat estimates of the posterior distribution of the model parameters.

To evaluate the applicability of the proposed method in a clinical context by analysing drug-induced and ANS-related changes in AV node conduction properties during AF

(aim 3) is addressed in *Papers II-IV*. In *Paper II*, we analysed the drug-dependent effect on circadian variations in the AV node properties by combining a genetic algorithm with a linear mixed-effects model, showing that β-blockers and calcium channel blockers have slightly different effects on the circadian variation of the AV node properties. In *Paper III-IV* we estimate the trends of the AV node conduction delay and refractory period and associated posterior distributions, rather than the original model parameters, increasing the interpretability, and thereby the applicability, of the results. Moreover, an attempt to predict the average heart rate after drug treatment was made in *Paper III*, which showed that time-variations in the AV node properties correlated with treatment outcome for metoprolol. Furthermore, in *Paper IV* we estimated the AV node conduction delay and refractory period with a beat-to-beat resolution during a tilt test to analyse the influence of the ANS.

6.1 Paper I: Non-invasive Characterization of Human AV-Nodal Conduction Delay and Refractory Period During Atrial Fibrillation

In this study we proposed a novel network model based on the work presented in [71] (the reference model). This novel model, also presented in Section 4.2.6, introduces a coupling node within the network model to address the reference model's shortcomings in representing clinical RR interval series dynamics. The refractory period and conduction delay of the coupling node are independent of the diastolic interval and the other pathway nodes. The paper also presents an associated workflow that utilises a problem-specific target function based on the Poincaré plot, leveraging the dynamics observed in the RR interval series, as well as a problem-specific genetic algorithm for optimisation.

Compared to the reference model, the model proposed in *Paper I* demonstrates the ability to replicate the dynamics present in the RR interval series extracted from ECG recordings. These dynamics are visualised in the Poincaré plot and autocorrelation function depicted in Figure 6.1. As seen in Figure 6.1, the reference model struggled with transmitting an impulse fast following a slow impulse; whereas the proposed model did not. Furthermore, the problem-specific genetic algorithm enabled reliable estimation of the model parameters from ECG recordings. The parameter estimation was evaluated using measured ECG data and simulated data. The estimation results suggested that the proposed model has the potential to assess drug-dependent variations in AV nodal conduction properties.

The model proposed in this paper is fitted to clinical measurements in *Papers II-IV* to estimate the AV node properties. Therefore, this first paper lays the ground for the remaining papers in this thesis.

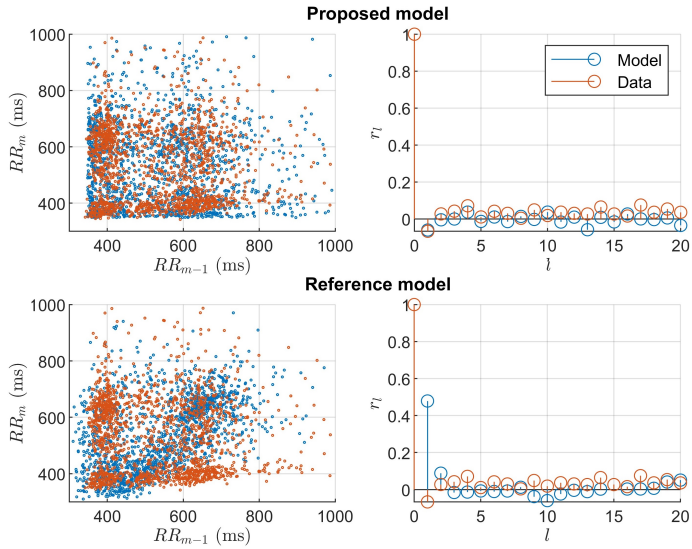

Figure 6.1: A comparison of the Poincaré plot (left) and autocorrelation (right) between the model and workflow proposed in *Paper I* (top), and the reference model and workflow proposed in [71] (bottom).

6.2 Paper II: ECG Based Assessment of Circadian Variation in AV-nodal Conduction During AF — Influence of Rate Control Drugs

In this study we used the model introduced in *Paper I* to investigate circadian variations in the conduction delay and refractory period of the AV node. In contrast to the genetic algorithm utilised in *Paper I*, this paper proposes a problem-specific genetic algorithm designed for dynamic optimisation. This algorithm dynamically adjusts its hyperparameters during optimisation based on changes observed in the RR interval series characteristics. This allows the algorithm to efficiently search for new model parameter sets during periods of rapid change in RR interval characteristics while also effectively converging towards optimal solutions during periods of slower change, allowing 24-hour analysis of the model parameters.

The proposed workflow was employed to estimate trends in the AV node model parameters over 24 hours with a resolution of one estimate per 1000 RR intervals. This analysis utilised ambulatory ECG data from 60 patients, acquired at baseline and under the influence of four different rate control drugs: two calcium channel blockers and two β-blockers [10].

Estimated model parameter trends were used in a mixed-effects model of a cosine to quantify drug-dependent mean (α_m) and circadian variation (β_m) in the AV node properties. This analysis revealed significant drug-dependent differences in the conduction properties, as illustrated in Figure 6.2. Notably, the difference was most pronounced for the maximum prolongation of the conduction delay (ΔD^{FP} and ΔD^{SP}), where β-blockers demonstrated a greater reduction in circadian variation compared to calcium channel blockers [10].

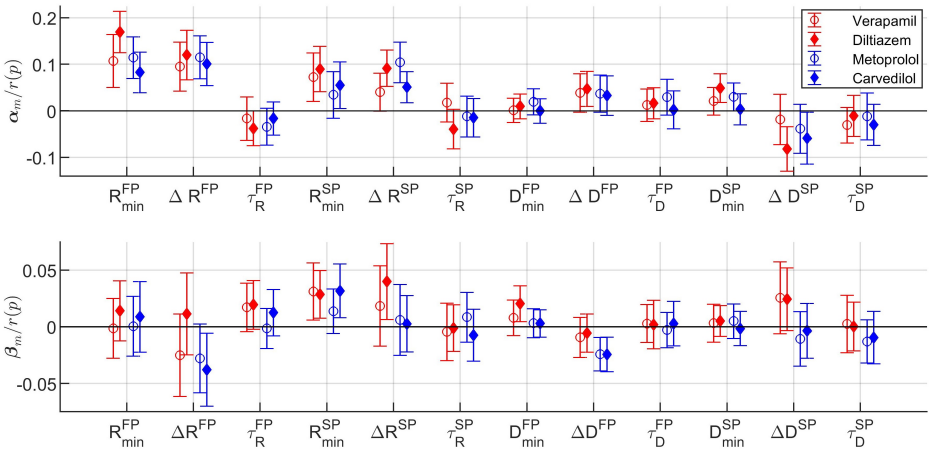

Figure 6.2: The fixed effect deviation from baseline for the linear mixed-effect model with corresponding 95% confidence intervals for the cosinor mean (top) and cosinor amplitude (bottom) for each of the twelve model parameters and four drugs. The confidence intervals not overlapping zero indicate a significant difference from baseline ($p < 0.05$).

6.3 Paper III: Model-based Estimation of AV-nodal Refractory Period and Conduction Delay Trends from ECG

In this study, we used the genetic algorithm presented in *Paper II* combined with an ABC algorithm to estimate the posterior distribution of the model parameters. This allows for a more nuanced interpretation of the results compared to point estimate as the posterior distribution represents a probability distribution over the parameter space. In addition, the characterisation of the AV node in *Paper II* is limited by the 12 model parameters' intrinsic complex dependencies, where a large change in the model parameters could result in a small change in the refractory period or conducting delay of the model nodes, making their interpretation a non-trivial task. Estimates of the refractory period and conduction delay of the slow and fast pathway of the AV node (RP^{FP}, RP^{SP}, CD^{FP}, and CD^{SP}), were therefore used for the analysis instead of using the original 12 model parameter estimates.

Using the same dataset as in *Paper II*, Holter ECG from 51 patients with permanent AF during baseline was analysed, with a resolution of 10 minutes [10]. Furthermore, the predictive power of variations in RP^{FP}, RP^{SP}, CD^{FP}, and CD^{SP} on the resulting heart rate reduction after treatment with four rate control drugs was investigated.

Diurnal variability in RP^{FP}, RP^{SP}, CD^{FP}, and CD^{SP} did not correlate with treatment outcome. Nor were machine learning tools able to predict drug efficacy based on diurnal variability. However, a significant correlation was found between the variability in the 10-minute estimates of RP^{FP} and CD^{FP} and the resulting heart rate reduction using the β-blocker metoprolol.

Reducing the 12 original parameters to four AV node properties facilitates a more comprehensible analysis, which is vital for effective communication of the results. This, combined with estimating the full posterior distribution, makes it possible to provide 24-hour trends of the AV node properties with detailed uncertainty. An example of this is shown in Figure 6.3, where a high variability in the AV node properties can be seen.

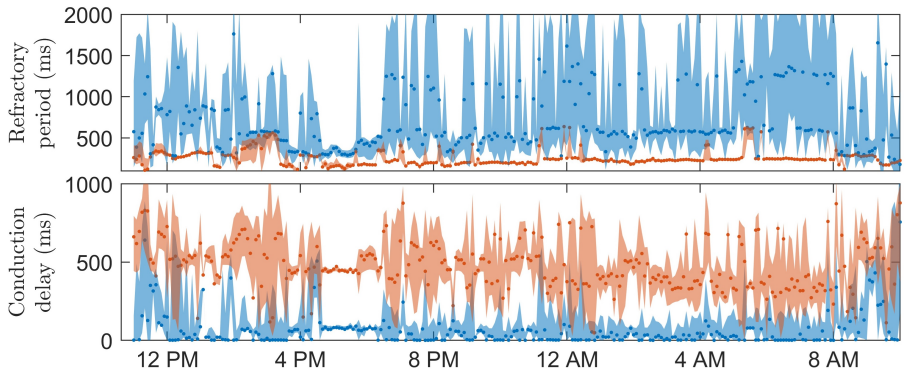

Figure 6.3: The median (dotted) and the 95% credibility region of the estimated refractory period (top) and conduction delay (bottom) for the FP (blue) and SP (red) for one patient.

6.4 Paper IV: ECG-based Beat-to-beat Assessment of AV Node Conduction Properties during AF

Based on the findings in *Paper III*, where the treatment outcome of the β-blocker metoprolol was correlated with variability in the 10-minute AV node property estimates, a natural next step was to investigate changes in AV node conduction properties with a higher temporal resolution. In *Paper III*, the temporal resolution was 10 minutes, which is quite low compared to e.g. the influence of the autonomic nervous system, which is known to modulate AV node conduction with beat-to-beat resolution [158].

Therefore, the fourth paper proposes to estimate the four AV node properties for each heartbeat using a particle filter and a smoothing algorithm. Using this approach, the full posterior distribution of the four AV node properties could be estimated for each heartbeat as shown in Figure 6.4, and high-frequency dynamics in the AV-node conduction properties could be studied.

The four AV node properties were denoted $\boldsymbol{\phi} = [R^{FP}, R^{SP}, D^{FP}, \text{and } D^{SP}]$. Using endocardial (invasive) recordings with simultaneous ECG recordings, the AV node properties for both cases could be estimated and compared. Additionally, simulated data was created allowing comparison to ground truth, showing an especially low error in R^{SP} (mean absolute error of 51 ± 12 ms). Furthermore, the AV node properties based on ECG recordings during a tilt test protocol were also analysed, where a sympathetic dominance of the ANS is assumed during head-tilt-up. From this analysis, R^{FP}, R^{SP}, and D^{FP} decreased significantly ($p < 0.05$) during head-up tilt compared with the horizontal position, which is in accordance with known changes from the literature (see Section 2.3).

By increasing the time resolution while keeping the advantages seen in *Paper III* of estimating the full posterior distribution of the four AV node properties, it was possible to assess changes to the AV node conduction properties at a beat-to-beat resolution of an individual AV node, something not previously possible. These changes capture information of the ANS activity, which could be used to gain new information about the AV node during AF, and possibly guide treatment selection in the future.

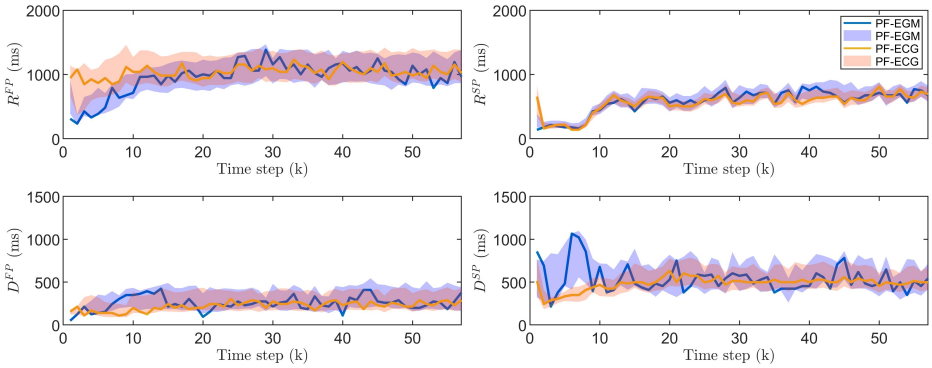

Figure 6.4: Estimates of AV node properties using the particle filter based on endocardial recordings (PF-EGM) and the particle filter based on ECG recordings (PF-ECG). The modes are shown with lines and the 80% credibility region as shaded background.

Chapter 7
Outlook and Conclusion

To conclude this thesis, the three aims stated in Chapter 1 have all been addressed. However, the aims are a way of concretizing the challenge of assisting in personalised treatment selection during AF. As of today, the optimal treatment for a given patient is still often chosen empirically, which can lead to a prolonged time until successful treatment and possibly result in a sub-optimal final choice of drug. We believe that assessing the AV node conduction properties could give insights into the individual AV node, and in turn, assist in treatment selection. The drug-dependent differences from *Paper II* seen in Figure 6.2 indicate a different drug-induced effect between β-blockers and calcium channel blockers on circadian variations. Moreover, the results from *Paper III* indicate an increased effect of the β-blocker metoprolol on the average heart rate for patients with a high 10-minute variability in their AV node properties. These findings hint at a possibility of using time variations of the AV node properties as a guide for treatment selection, however a high inter-patient variability combined with a relatively low number of patients (60 in *Paper II-III*) stresses a need to verify the results in a larger population.

Since *Paper III* indicates a correlation between short-term variability and drug effect, and *Paper IV* introduces a methodology yielding higher temporal resolution, it would be of interest to combine these works. However, applying the methodology from *Paper IV* to the 24-hour ECG segments used in *Paper III* would be difficult from a computational and data-handling viewpoint, and several improvements to the particle filter would need to be addressed. Nevertheless, if possible, it could yield valuable insights into the workings of the AV node during AF.

Another issue with the ECG-based approach is the signal-to-noise ratio in the signals. When estimating properties on a beat-to-beat resolution, the data quality is highly influential. This includes (but is not limited to) motion artifacts in ambulatory ECG,

the accuracy of R peak detection, and analysis of f-waves and signal quality. It can thus be difficult to know if alterations to the AV node properties originate from measurement errors such as these, or actual changes in the AV node. Fortunately, electrodes and the whole ECG system are improving year after year, which hopefully can mitigate this issue. With that said, newer studies also need to be conducted with this new equipment. In *Paper IV*, as an example, we used data from the Intracardiac AF Database [159] recorded in the year 2000, due to the difficulties of accessing invasive and non-invasive recordings of the heart during AF simultaneously.

In this work, ECG has been used as the primary non-invasive measurement. Nonetheless, the rise of PPG recordings from smartwatches is still ongoing. It is possible to extract the RR interval series from PPG recordings, thus basing the AV node estimates solely on the RR interval series could be of interest. Doing so would lose virtually all information about the atria, which is of great importance during AF. Nevertheless, this convenience may be attractive for large-scale studies or applications in the future. However, further research is needed to determine if the loss of atrial information is acceptable for accurate AV node function assessment.

In conclusion, this work has for the first time analysed time-variations in AV node conduction properties based on ECG recordings in a cohort of patients in order to study the drug- and ANS-induced changes. By doing this, quantifiable differences in their effects on conduction properties between β-blockers and calcium channel blockers could be observed (*Paper II*). As previously discussed, there are still improvements that could be made, and additional studies that could be performed. In addition, newer data with higher signal quality could improve the results and improve our understanding of the AV node. Nevertheless, with over 100 years of studies of the AV node, it can yet be identified as a riddle wrapped up in a mystery, inside an enigma [160].

References

[1] M. Karlsson, F. Sandberg, S. R. Ulimoen, and M. Wallman, "Non-invasive characterization of human AV-nodal conduction delay and refractory period during atrial fibrillation," *Frontiers in physiology*, p. 1849, 2021.

[2] M. Karlsson, M. Wallman, P. G. Platonov, S. R. Ulimoen, and F. Sandberg, "ECG based assessment of circadian variation in AV-nodal conduction during AF—influence of rate control drugs," *Frontiers in physiology*, p. 2015, 2022.

[3] M. Karlsson, P. G. Platonov, S. R. Ulimoen, F. Sandberg, and M. Wallman, "Model-based estimation of AV-nodal refractory period and conduction delay trends from ECG," *Frontiers in Physiology*, vol. 14, p. 1287365, 2024.

[4] M. Karlsson, M. Wallman, S. R. Ulimoen, and F. Sandberg, "Non-invasive characterization of atrio-ventricular properties during atrial fibrillation," *2021 Computing in Cardiology (CinC)*, vol. 48, pp. 1–4, 2021.

[5] M. Karlsson, M. Wallman, P. G. Platonov, S. R. Ulimoen, and F. Sandberg, "Drug dependent circadian variations in AV-nodal properties during atrial fibrillation," *2022 Computing in Cardiology (CinC)*, vol. 498, pp. 1–4, 2022.

[6] M. Karlsson, M. Wallman, P. G. Platonov, S. R. Ulimoen, and F. Sandberg, "ECG-based assessment and therapeutic implications of AV nodal conduction dynamics during atrial fibrillation," *2023 Computing in Cardiology (CinC)*, vol. 50, pp. 1–4, 2023.

[7] G. Hindricks, T. Potpara, N. Dagres, E. Arbelo, J. J. Bax, C. Blomström-Lundqvist, G. Boriani, M. Castella, G.-A. Dan, P. E. Dilaveris, *et al.*, "2020 ESC guidelines for the diagnosis and management of atrial fibrillation developed in collaboration with the european association for cardio-thoracic surgery

(EACTS) the task force for the diagnosis and management of atrial fibrillation of the european society of cardiology (ESC) developed with the special contribution of the european heart rhythm association (EHRA) of the ESC," *European heart journal*, vol. 42, no. 5, pp. 373–498, 2021.

[8] E. J. Benjamin, P. A. Wolf, R. B. D'Agostino, H. Silbershatz, W. B. Kannel, and D. Levy, "Impact of atrial fibrillation on the risk of death: the framingham heart study," *Circulation*, vol. 98, no. 10, pp. 946–952, 1998.

[9] N. E. Andrew, A. G. Thrift, and D. A. Cadilhac, "The prevalence, impact and economic implications of atrial fibrillation in stroke: what progress has been made?," *Neuroepidemiology*, vol. 40, no. 4, pp. 227–239, 2013.

[10] S. R. Ulimoen, S. Enger, J. Carlson, P. G. Platonov, A. H. Pripp, M. Abdelnoor, H. Arnesen, K. Gjesdal, and A. Tveit, "Comparison of four single-drug regimens on ventricular rate and arrhythmia-related symptoms in patients with permanent atrial fibrillation," *The American journal of cardiology*, vol. 111, no. 2, pp. 225–230, 2013.

[11] P.-S. Chen, L. S. Chen, M. C. Fishbein, S.-F. Lin, and S. Nattel, "Role of the autonomic nervous system in atrial fibrillation: pathophysiology and therapy," *Circulation research*, vol. 114, no. 9, pp. 1500–1515, 2014.

[12] G. Vanagas, T. Krilavičius, and K. L. Man, "Mathematical modeling and models for optimal decision-making in health care," *Computational and mathematical methods in medicine*, vol. 2019, 2019.

[13] Y. Liu, R. Wu, and A. Yang, "Research on medical problems based on mathematical models," *Mathematics*, vol. 11, no. 13, p. 2842, 2023.

[14] A. Di Carlo, L. Bellino, D. Consoli, F. Mori, A. Zaninelli, M. Baldereschi, A. Cattarinussi, M. G. D'Alfonso, C. Gradia, B. Sgherzi, *et al.*, "Prevalence of atrial fibrillation in the Italian elderly population and projections from 2020 to 2060 for Italy and the European Union: the FAI project," *EP Europace*, vol. 21, no. 10, pp. 1468–1475, 2019.

[15] M. Karlsson, "Model-based analysis of temporal patterns in atrioventricular node conduction during atrial fibrillation [licentiate thesis]," *Lund University*, 2022.

[16] Z. Jiang, M. Pajic, S. Moarref, R. Alur, and R. Mangharam, "Modeling and verification of a dual chamber implantable pacemaker," in *International Conference on Tools and Algorithms for the Construction and Analysis of Systems*, pp. 188–203, Springer, 2012.

[17] J. E. Hall, *Guyton and Hall textbook of medical physiology e-Book*. Elsevier Health Sciences, 2010.

[18] H. Shih, "Anatomy of the action potential in the heart.," *Texas Heart Institute Journal*, vol. 21, no. 1, p. 30, 1994.

[19] T. N. James, "The internodal pathways of the human heart," *Progress in cardiovascular diseases*, vol. 43, no. 6, pp. 495–535, 2001.

[20] G. J. Tortora and B. H. Derrickson, *Introduction to the human body*. John Wiley & Sons, 2017.

[21] O. Monfredi, H. Dobrzynski, T. Mondal, M. R. Boyett, and G. M. Morris, "The anatomy and physiology of the sinoatrial node — a contemporary review," *Pacing and clinical electrophysiology*, vol. 33, no. 11, pp. 1392–1406, 2010.

[22] F. L. Meijler and M. J. Janse, "Morphology and electrophysiology of the mammalian atrioventricular node," *Physiological reviews*, vol. 68, no. 2, pp. 608–647, 1988.

[23] S. A. George, N. R. Faye, A. Murillo-Berlioz, K. B. Lee, G. D. Trachiotis, and I. R. Efimov, "At the atrioventricular crossroads: dual pathway electrophysiology in the atrioventricular node and its underlying heterogeneities," *Arrhythmia & electrophysiology review*, vol. 6, no. 4, p. 179, 2017.

[24] G. K. Moe, J. B. Preston, and H. Burlington, "Physiologic evidence for a dual AV transmission system," *Circulation Research*, vol. 4, no. 4, pp. 357–375, 1956.

[25] T. Kurian, C. Ambrosi, W. Hucker, V. V. Fedorov, and I. R. Efimov, "Anatomy and electrophysiology of the human AV node," *Pacing and clinical electrophysiology*, vol. 33, no. 6, pp. 754–762, 2010.

[26] T. Nikolaidou, O. Aslanidi, H. Zhang, and I. Efimov, "Structure–function relationship in the sinus and atrioventricular nodes," *Pediatric cardiology*, vol. 33, no. 6, pp. 890–899, 2012.

[27] M. D. Gonzalez, J. E. Banchs, T. Moukabary, and J. Rivera, "Ablation of atrioventricular junctional tachycardias: atrioventricular nodal reentry, variants, and focal junctional tachycardia," *Catheter Ablation of Cardiac Arrhythmias: Catheter Ablation of Cardiac Arrhythmias E-Book*, p. 316, 2019.

[28] Y. Zhang, "A jump in the atrioventricular conduction curve is not caused by a switch from fast pathway to slow pathway conduction," *Frontiers in Physiology*, vol. 15, p. 1367509, 2024.

[29] V. V. Fedorov, C. M. Ambrosi, G. Kostecki, W. J. Hucker, A. V. Glukhov, J. P. Wuskell, L. M. Loew, N. Moazami, and I. R. Efimov, "Anatomic localization and autonomic modulation of atrioventricular junctional rhythm in failing human hearts," *Circulation: Arrhythmia and Electrophysiology*, vol. 4, no. 4, pp. 515–525, 2011.

[30] J. Billette, "Atrioventricular nodal activation during periodic premature stimulation of the atrium," *American Journal of Physiology-Heart and Circulatory Physiology*, vol. 252, no. 1, pp. H163–H177, 1987.

[31] A. P. DE Carvalho and D. F. De Almeida, "Spread of activity through the atrioventricular node," *Circulation research*, vol. 8, no. 4, pp. 801–809, 1960.

[32] S. Liu, S. B. Olsson, Y. Yang, E. Hertervig, O. Kongstad, and S. Yuan, "Concealed conduction and dual pathway physiology of the atrioventricular node," *Journal of cardiovascular electrophysiology*, vol. 15, no. 2, pp. 144–149, 2004.

[33] A. Lymperopoulos, G. Rengo, and W. J. Koch, "Adrenergic nervous system in heart failure: pathophysiology and therapy," *Circulation research*, vol. 113, no. 6, pp. 739–753, 2013.

[34] R. Gordan, J. K. Gwathmey, and L.-H. Xie, "Autonomic and endocrine control of cardiovascular function," *World journal of cardiology*, vol. 7, no. 4, p. 204, 2015.

[35] J. W. Lister, E. Stein, B. D. Kosowsky, S. H. Lau, and A. N. Damato, "Atrioventricular conduction in man: Effect of rate, exercise, isoproterenol and atropine on the PR interval," *The American Journal of Cardiology*, vol. 16, no. 4, pp. 516–523, 1965.

[36] R. C. Dhingra, E. Winslow, J. M. Pouget, S. H. Rahimtoola, and K. M. Rosen, "The effect of isoproterenol on atrioventricular and intraventricular conduction," *The American Journal of Cardiology*, vol. 32, no. 5, pp. 629–636, 1973.

[37] F. Morady, S. D. Nelson, W. H. Kou, R. Pratley, S. Schmaltz, M. De Buitleir, and J. B. Halter, "Electrophysiologic effects of epinephrine in humans," *Journal of the American College of Cardiology*, vol. 11, no. 6, pp. 1235–1244, 1988.

[38] S. F. Cossú, S. A. Rothman, I. L. Chmielewski, H. H. Hsia, R. L. Vogel, J. M. Miller, and A. E. Buxton, "The effects of isoproterenol on the cardiac conduction system: Site-specific dose dependence," *Journal of cardiovascular electrophysiology*, vol. 8, no. 8, pp. 847–853, 1997.

[39] E. A. MacDonald, R. A. Rose, and T. A. Quinn, "Neurohumoral control of sinoatrial node activity and heart rate: insight from experimental models and findings from humans," *Frontiers in physiology*, vol. 11, p. 476266, 2020.

[40] K. Pemberton and S. P. Jones, "Inhibition of the L-type calcium channel by the five muscarinic receptors (m1–m5) expressed in NIH 3T3 cells," *Pflügers Archiv*, vol. 433, pp. 505–514, 1997.

[41] B. G. Katzung, S. B. Masters, A. J. Trevor, *et al.*, "Basic & clinical pharmacology," 2004.

[42] F. Holmqvist, M. Stridh, J. E. Waktare, J. Brandt, L. Sörnmo, A. Roijer, and C. J. Meurling, "Rapid fluctuations in atrial fibrillatory electrophysiology detected during controlled respiration," *American Journal of Physiology-Heart and Circulatory Physiology*, vol. 289, no. 2, pp. H754–H760, 2005.

[43] R. Freeman and M. W. Chapleau, "Testing the autonomic nervous system," *Handbook of clinical neurology*, vol. 115, pp. 115–136, 2013.

[44] M. A. Russo, D. M. Santarelli, and D. O'Rourke, "The physiological effects of slow breathing in the healthy human," *Breathe*, vol. 13, no. 4, pp. 298–309, 2017.

[45] K. Efremov, D. Brisinda, A. Venuti, E. Iantorno, C. Cataldi, F. Fioravanti, and R. Fenici, "Heart rate variability analysis during head-up tilt test predicts nitroglycerine-induced syncope," *Open Heart*, vol. 1, no. 1, p. e000063, 2014.

[46] F. Shaffer and J. P. Ginsberg, "An overview of heart rate variability metrics and norms," *Frontiers in public health*, vol. 5, p. 258, 2017.

[47] D. E. Krummen, S. Hebsur, J. Salcedo, S. M. Narayan, G. G. Lalani, and A. A. Schricker, "Mechanisms underlying AF: triggers, rotors, other?," *Current treatment options in cardiovascular medicine*, vol. 17, pp. 1–14, 2015.

[48] M. Haissaguerre, P. Jaïs, D. C. Shah, A. Takahashi, M. Hocini, G. Quiniou, S. Garrigue, A. Le Mouroux, P. Le Métayer, and J. Clémenty, "Spontaneous initiation of atrial fibrillation by ectopic beats originating in the pulmonary veins," *New England Journal of Medicine*, vol. 339, no. 10, pp. 659–666, 1998.

[49] P. Santangeli, E. S. Zado, M. D. Hutchinson, M. P. Riley, D. Lin, D. S. Frankel, G. E. Supple, F. C. Garcia, S. Dixit, D. J. Callans, *et al.*, "Prevalence and distribution of focal triggers in persistent and long-standing persistent atrial fibrillation," *Heart Rhythm*, vol. 13, no. 2, pp. 374–382, 2016.

[50] N. Voigt, J. Heijman, Q. Wang, D. Y. Chiang, N. Li, M. Karck, X. H. Wehrens, S. Nattel, and D. Dobrev, "Cellular and molecular mechanisms of atrial arrhythmogenesis in patients with paroxysmal atrial fibrillation," *Circulation*, vol. 129, no. 2, pp. 145–156, 2014.

[51] L. Sörnmo, *Atrial fibrillation from an engineering perspective*. Springer, 2018.

[52] S. M. Narayan and J. Jalife, "Crosstalk proposal: Rotors have been demonstrated to drive human atrial fibrillation," *The Journal of physiology*, vol. 592, no. pt 15, p. 3163, 2014.

[53] M. Allessie and N. de Groot, "Crosstalk opposing view: Rotors have not been demonstrated to be the drivers of atrial fibrillation," *The Journal of physiology*, vol. 592, no. pt 15, p. 3167, 2014.

[54] R. T. Carrick, B. E. Benson, O. R. Bates, and P. S. Spector, "Competitive drivers of atrial fibrillation: The interplay between focal drivers and multiwavelet reentry," *Frontiers in Physiology*, vol. 12, p. 633643, 2021.

[55] A. Shiroshita-Takeshita, B. J. Brundel, and S. Nattel, "Atrial fibrillation: basic mechanisms, remodeling and triggers," *Journal of Interventional Cardiac Electrophysiology*, vol. 13, no. 3, pp. 181–193, 2005.

[56] M. C. Wijffels, C. J. Kirchhof, R. Dorland, and M. A. Allessie, "Atrial fibrillation begets atrial fibrillation: a study in awake chronically instrumented goats," *Circulation*, vol. 92, no. 7, pp. 1954–1968, 1995.

[57] J. Park, S. Lee, and M. Jeon, "Atrial fibrillation detection by heart rate variability in poincare plot," *Biomedical engineering online*, vol. 8, no. 1, pp. 1–12, 2009.

[58] J. Lee, Y. Nam, D. D. McManus, and K. H. Chon, "Time-varying coherence function for atrial fibrillation detection," *IEEE Transactions on Biomedical Engineering*, vol. 60, no. 10, pp. 2783–2793, 2013.

[59] G. H. Tison, J. M. Sanchez, B. Ballinger, A. Singh, J. E. Olgin, M. J. Pletcher, E. Vittinghoff, E. S. Lee, S. M. Fan, R. A. Gladstone, *et al.*, "Passive detection of atrial fibrillation using a commercially available smartwatch," *JAMA cardiology*, vol. 3, no. 5, pp. 409–416, 2018.

[60] S. Kwon, J. Hong, E.-K. Choi, E. Lee, D. E. Hostallero, W. J. Kang, B. Lee, E.-R. Jeong, B.-K. Koo, S. Oh, *et al.*, "Deep learning approaches to detect atrial fibrillation using photoplethysmographic signals: algorithms development study," *JMIR mHealth and uHealth*, vol. 7, no. 6, p. e12770, 2019.

[61] M. V. Perez, K. W. Mahaffey, H. Hedlin, J. S. Rumsfeld, A. Garcia, T. Ferris, V. Balasubramanian, A. M. Russo, A. Rajmane, L. Cheung, *et al.*, "Large-scale assessment of a smartwatch to identify atrial fibrillation," *New England Journal of Medicine*, vol. 381, no. 20, pp. 1909–1917, 2019.

[62] S. A. Lubitz, A. Z. Faranesh, C. Selvaggi, S. J. Atlas, D. D. McManus, D. E. Singer, S. Pagoto, M. V. McConnell, A. Pantelopoulos, and A. S. Foulkes, "Detection of atrial fibrillation in a large population using wearable devices: the Fitbit Heart Study," *Circulation*, vol. 146, no. 19, pp. 1415–1424, 2022.

[63] J. Park, C. Lee, E. Leshem, I. Blau, S. Kim, J. M. Lee, J.-A. Hwang, B.-I. Choi, M.-H. Lee, and H. J. Hwang, "Early differentiation of long-standing persistent atrial fibrillation using the characteristics of fibrillatory waves in surface ECG multi-leads," *Scientific reports*, vol. 9, no. 1, p. 2746, 2019.

[64] M. Henriksson, A. Petrėnas, V. Marozas, F. Sandberg, and L. Sörnmo, "Model-based assessment of f-wave signal quality in patients with atrial fibrillation," *IEEE Transactions on Biomedical Engineering*, vol. 65, no. 11, pp. 2600–2611, 2018.

[65] M. Abdollahpur, G. Engström, P. G. Platonov, and F. Sandberg, "A subspace projection approach to quantify respiratory variations in the f-wave frequency trend," *Frontiers in Physiology*, vol. 13, p. 976925, 2022.

[66] F. Sandberg, M. Stridh, and L. Sörnmo, "Frequency tracking of atrial fibrillation using hidden markov models," *IEEE Transactions on Biomedical Engineering*, vol. 55, no. 2, pp. 502–511, 2008.

[67] M. Stridh and L. Sörnmo, "Spatiotemporal QRST cancellation techniques for analysis of atrial fibrillation," *IEEE Transactions on Biomedical Engineering*, vol. 48, no. 1, pp. 105–111, 2001.

[68] N. V. Thakor and Y.-S. Zhu, "Applications of adaptive filtering to ECG analysis: noise cancellation and arrhythmia detection," *IEEE transactions on biomedical engineering*, vol. 38, no. 8, pp. 785–794, 1991.

[69] V. Zarzoso and P. Comon, "Robust independent component analysis by iterative maximization of the kurtosis contrast with algebraic optimal step size," *IEEE Transactions on neural networks*, vol. 21, no. 2, pp. 248–261, 2009.

[70] S. Biton, M. Suleiman, N. B. Moshe, L. Sörnmo, and J. A. Behar, "Estimation of f-wave dominant frequency using a voting scheme," *arXiv preprint arXiv:2209.03762*, 2022.

[71] M. Wallman and F. Sandberg, "Characterisation of human AV-nodal properties using a network model," *Medical & biological engineering & computing*, vol. 56, no. 2, pp. 247–259, 2018.

[72] S. Dash, K. Chon, S. Lu, and E. Raeder, "Automatic real time detection of atrial fibrillation," *Annals of biomedical engineering*, vol. 37, no. 9, pp. 1701–1709, 2009.

[73] F. Plappert, M. Wallman, M. Abdollahpur, P. G. Platonov, S. Östenson, and F. Sandberg, "An atrioventricular node model incorporating autonomic tone," *Frontiers in Physiology*, vol. 13, 2022.

[74] G. Moody, "A new method for detecting atrial fibrillation using RR intervals," *Computers in Cardiology*, pp. 227–230, 1983.

[75] A. J. Camm, A. Capucci, S. H. Hohnloser, C. Torp-Pedersen, I. C. Van Gelder, B. Mangal, G. Beatch, and A. Investigators, "A randomized active-controlled study comparing the efficacy and safety of vernakalant to amiodarone in recent-onset atrial fibrillation," *Journal of the American College of Cardiology*, vol. 57, no. 3, pp. 313–321, 2011.

[76] G. C. Markey, N. Salter, and J. Ryan, "Intravenous flecainide for emergency department management of acute atrial fibrillation," *The Journal of Emergency Medicine*, vol. 54, no. 3, pp. 320–327, 2018.

[77] F. J. Martínez-Marcos, J. L. García-Garmendia, A. Ortega-Carpio, J. M. Fernández-Gómez, J. M. Santos, and C. Camacho, "Comparison of intravenous flecainide, propafenone, and amiodarone for conversion of acute atrial fibrillation to sinus rhythm," *The American journal of cardiology*, vol. 86, no. 9, pp. 950–953, 2000.

[78] D. Roy, M. Talajic, S. Nattel, D. G. Wyse, P. Dorian, K. L. Lee, M. G. Bourassa, J. M. O. Arnold, A. E. Buxton, A. J. Camm, *et al.*, "Rhythm control versus rate control for atrial fibrillation and heart failure," *New England Journal of Medicine*, vol. 358, no. 25, pp. 2667–2677, 2008.

[79] B. N. Singh, S. J. Connolly, H. J. Crijns, D. Roy, P. R. Kowey, A. Capucci, D. Radzik, E. M. Aliot, and S. H. Hohnloser, "Dronedarone for maintenance of sinus rhythm in atrial fibrillation or flutter," *New England Journal of Medicine*, vol. 357, no. 10, pp. 987–999, 2007.

[80] L. Mont, F. Bisbal, A. Hernandez-Madrid, N. Perez-Castellano, X. Viñolas, A. Arenal, F. Arribas, I. Fernández-Lozano, A. Bodegas, A. Cobos, *et al.*, "Catheter ablation vs. antiarrhythmic drug treatment of persistent atrial fibrillation: a multicentre, randomized, controlled trial (SARA study)," *European heart journal*, vol. 35, no. 8, pp. 501–507, 2014.

[81] A. N. Ganesan, N. J. Shipp, A. G. Brooks, P. Kuklik, D. H. Lau, H. S. Lim, T. Sullivan, K. C. Roberts-Thomson, and P. Sanders, "Long-term outcomes of catheter ablation of atrial fibrillation: a systematic review and meta-analysis," *Journal of the American Heart Association*, vol. 2, no. 2, p. e004549, 2013.

[82] N. Mujović, M. Marinković, R. Lenarczyk, R. Tilz, and T. S. Potpara, "Catheter ablation of atrial fibrillation: an overview for clinicians," *Advances in therapy*, vol. 34, pp. 1897–1917, 2017.

[83] F. J. Venditti Jr, H. Garan, and J. N. Ruskin, "Electrophysiologic effects of beta blockers in ventricular arrhythmias," *The American Journal of Cardiology*, vol. 60, no. 6, pp. 3–9, 1987.

[84] P. Rizzon, M. Di Biase, A. Chiddo, D. Mastrangelo, and L. Sorgente, "Electrophysiological properties of intravenous metoprolol in man.," *British Heart Journal*, vol. 40, no. 6, p. 650, 1978.

[85] E. M. Kanoupakis, E. G. Manios, H. E. Mavrakis, P. G. Tzerakis, H. K. Mouloudi, and P. E. Vardas, "Comparative effects of carvedilol and amiodarone on conversion and recurrence rates of persistent atrial fibrillation," *The American journal of cardiology*, vol. 94, no. 5, pp. 659–662, 2004.

[86] M. Talajic, R. Lemery, D. Roy, C. Villemaire, R. Cartier, B. Coutu, and S. Nattel, "Rate-dependent effects of diltiazem on human atrioventricular nodal properties.," *Circulation*, vol. 86, no. 3, pp. 870–877, 1992.

[87] J. Leboeuf, J. Lamar, R. Massingham, and J. Ponsonnaille, "Electrophysiological effects of bepridil and its quaternary derivative CERM 11888 in closed chest anaesthetized dogs: a comparison with verapamil and diltiazem.," *British journal of pharmacology*, vol. 98, no. 4, p. 1351, 1989.

[88] I. C. Van Gelder, M. Rienstra, H. J. Crijns, and B. Olshansky, "Rate control in atrial fibrillation," *The Lancet*, vol. 388, no. 10046, pp. 818–828, 2016.

[89] S. M. Al-Khatib, N. M. Allen LaPointe, R. Chatterjee, M. J. Crowley, M. E. Dupre, D. F. Kong, R. D. Lopes, T. J. Povsic, S. S. Raju, B. Shah, *et al.*, "Rate- and rhythm-control therapies in patients with atrial fibrillation: a systematic review," *Annals of internal medicine*, vol. 160, no. 11, pp. 760–773, 2014.

[90] I. Greener, O. Monfredi, S. Inada, N. Chandler, J. Tellez, A. Atkinson, M.-A. Taube, R. Billeter, R. Anderson, I. Efimov, *et al.*, "Molecular architecture of the human specialised atrioventricular conduction axis," *Journal of molecular and cellular cardiology*, vol. 50, no. 4, pp. 642–651, 2011.

[91] S. A. George, N. R. Faye, A. Murillo-Berlioz, K. B. Lee, G. D. Trachiotis, and I. R. Efimov, "At the atrioventricular crossroads: dual pathway electrophysiology in the atrioventricular node and its underlying heterogeneities," *Arrhythmia & electrophysiology review*, vol. 6, no. 4, p. 179, 2017.

[92] F. Philippon, V. J. Plumb, and G. N. KAY, "Differential effect of esmolol on the fast and slow av nodal pathways in patients with av nodal reentrant tachycardia," *Journal of Cardiovascular Electrophysiology*, vol. 5, no. 10, pp. 810–817, 1994.

[93] J. Billette and R. Tadros, "An integrated overview of av node physiology," *Pacing and Clinical Electrophysiology*, vol. 42, no. 7, pp. 805–820, 2019.

[94] D. G. Whittaker, M. Clerx, C. L. Lei, D. J. Christini, and G. R. Mirams, "Calibration of ionic and cellular cardiac electrophysiology models," *Wiley Interdisciplinary Reviews: Systems Biology and Medicine*, vol. 12, no. 4, p. e1482, 2020.

[95] A. L. Hodgkin and A. F. Huxley, "A quantitative description of membrane current and its application to conduction and excitation in nerve," *The Journal of physiology*, vol. 117, no. 4, p. 500, 1952.

[96] D. Noble, "A modification of the Hodgkin—Huxley equations applicable to Purkinje fibre action and pacemaker potentials," *The Journal of physiology*, vol. 160, no. 2, p. 317, 1962.

[97] W. T. Miller and D. B. Geselowitz, "Simulation studies of the electrocardiogram. i. the normal heart.," *Circulation Research*, vol. 43, no. 2, pp. 301–315, 1978.

[98] A. Quarteroni, T. Lassila, S. Rossi, and R. Ruiz-Baier, "Integrated heart—coupling multiscale and multiphysics models for the simulation of the cardiac function," *Computer Methods in Applied Mechanics and Engineering*, vol. 314, pp. 345–407, 2017.

[99] J. Heijman, H. Sutanto, H. J. Crijns, S. Nattel, and N. A. Trayanova, "Computational models of atrial fibrillation: Achievements, challenges, and perspectives for improving clinical care," *Cardiovascular Research*, vol. 117, no. 7, pp. 1682–1699, 2021.

[100] P. Colli Franzone, L. Guerri, and S. Rovida, "Wavefront propagation in an activation model of the anisotropic cardiac tissue: asymptotic analysis and numerical simulations," *Journal of mathematical biology*, vol. 28, pp. 121–176, 1990.

[101] J. P. Keener, "An eikonal-curvature equation for action potential propagation in myocardium," *Journal of mathematical biology*, vol. 29, no. 7, pp. 629–651, 1991.

[102] A. Neic, F. O. Campos, A. J. Prassl, S. A. Niederer, M. J. Bishop, E. J. Vigmond, and G. Plank, "Efficient computation of electrograms and ECGs in human whole heart simulations using a reaction-eikonal model," *Journal of computational physics*, vol. 346, pp. 191–211, 2017.

[103] K. S. McDowell, S. Zahid, F. Vadakkumpadan, J. Blauer, R. S. MacLeod, and N. A. Trayanova, "Virtual electrophysiological study of atrial fibrillation in fibrotic remodeling," *PloS one*, vol. 10, no. 2, p. e0117110, 2015.

[104] B. J. Hansen, J. Zhao, K. M. Helfrich, N. Li, A. Iancau, A. M. Zolotarev, S. O. Zakharkin, A. Kalyanasundaram, M. Subr, N. Dastagir, *et al.*, "Unmasking arrhythmogenic hubs of reentry driving persistent atrial fibrillation for patient-specific treatment," *Journal of the American Heart Association*, vol. 9, no. 19, p. e017789, 2020.

[105] S. Inada, J. Hancox, H. Zhang, and M. Boyett, "One-dimensional mathematical model of the atrioventricular node including atrio-nodal, nodal, and nodal-his cells," *Biophysical journal*, vol. 97, no. 8, pp. 2117–2127, 2009.

[106] M. Ryzhii and E. Ryzhii, "A compact multi-functional model of the rabbit atrioventricular node with dual pathways," *Frontiers in Physiology*, vol. 14, p. 1126648, 2023.

[107] J. Lian, D. Mussig, and V. Lang, "Computer modeling of ventricular rhythm during atrial fibrillation and ventricular pacing," *IEEE transactions on biomedical engineering*, vol. 53, no. 8, pp. 1512–1520, 2006.

[108] A. M. Climent, M. S. Guillem, Y. Zhang, J. Millet, and T. Mazgalev, "Functional mathematical model of dual pathway AV nodal conduction," *American Journal of Physiology-Heart and Circulatory Physiology*, vol. 300, no. 4, pp. H1393–H1401, 2011.

[109] V. D. Corino, F. Sandberg, L. T. Mainardi, and L. Sörnmo, "An atrioventricular node model for analysis of the ventricular response during atrial fibrillation,"

IEEE transactions on biomedical engineering, vol. 58, no. 12, pp. 3386–3395, 2011.

[110] A. Shrier, H. Dubarsky, M. Rosengarten, M. R. Guevara, S. Nattel, and L. Glass, "Prediction of complex atrioventricular conduction rhythms in humans with use of the atrioventricular nodal recovery curve.," *Circulation*, vol. 76, no. 6, pp. 1196–1205, 1987.

[111] J. Billette and S. Nattel, "Dynamic behavior of the atrioventricular node: a functional model of interaction between recovery, facilitation, and fatigue," *Journal of cardiovascular electrophysiology*, vol. 5, no. 1, pp. 90–102, 1994.

[112] J. Sun, F. Amellal, L. Glass, and J. Billette, "Alternans and period-doubling bifurcations in atrioventricular nodal conduc," *Journal of theoretical biology*, vol. 173, no. 1, pp. 79–91, 1995.

[113] P. Jørgensen, C. Schäfer, P. G. Guerra, M. Talajic, S. Nattel, and L. Glass, "A mathematical model of human atrioventricular nodal function incorporating concealed conduction," *Bulletin of mathematical biology*, vol. 64, pp. 1083–1099, 2002.

[114] L. Mangin, A. Vinet, P. Pagé, and L. Glass, "Effects of antiarrhythmic drug therapy on atrioventricular nodal function during atrial fibrillation in humans," *EP Europace*, vol. 7, no. s2, pp. S71–S82, 2005.

[115] M. Masè, L. Glass, M. Disertori, and F. Ravelli, "Nodal recovery, dual pathway physiology, and concealed conduction determine complex av dynamics in human atrial tachyarrhythmias," *American Journal of Physiology-Heart and Circulatory Physiology*, vol. 303, no. 10, pp. H1219–H1228, 2012.

[116] M. Masè, M. Marini, M. Disertori, and F. Ravelli, "Dynamics of AV coupling during human atrial fibrillation: role of atrial rate," *American Journal of Physiology-Heart and Circulatory Physiology*, vol. 309, no. 1, pp. H198–H205, 2015.

[117] R. R. Aliev and A. V. Panfilov, "A simple two-variable model of cardiac excitation," *Chaos, Solitons & Fractals*, vol. 7, no. 3, pp. 293–301, 1996.

[118] V. D. Corino, F. Sandberg, F. Lombardi, L. T. Mainardi, and L. Sörnmo, "Atrioventricular nodal function during atrial fibrillation: Model building and robust estimation," *Biomedical Signal Processing and Control*, vol. 8, no. 6, pp. 1017–1025, 2013.

[119] M. Henriksson, V. D. Corino, L. Sörnmo, and F. Sandberg, "A statistical atrioventricular node model accounting for pathway switching during atrial fibrillation," *IEEE Transactions on Biomedical Engineering*, vol. 63, no. 9, pp. 1842–1849, 2015.

[120] E. W. Dijkstra *et al.*, "A note on two problems in connexion with graphs," *Numerische mathematik*, vol. 1, no. 1, pp. 269–271, 1959.

[121] M. Wallman and F. Sandberg, "Characterization of AV-nodal properties during atrial fibrillation using a multilevel modelling approach," in *2015 Computing in cardiology conference (CinC)*, pp. 477–480, IEEE, 2015.

[122] T. Bayes, "An essay towards solving a problem in the doctrine of chances. by the late Rev. Mr. Bayes, FRS communicated by Mr. Price, in a letter to John Canton, AMFR S," *Philosophical transactions of the Royal Society of London*, no. 53, pp. 370–418, 1763.

[123] E. Borgonovo and E. Plischke, "Sensitivity analysis: a review of recent advances," *European Journal of Operational Research*, vol. 248, no. 3, pp. 869–887, 2016.

[124] I. M. Sobol, "Sensitivity analysis for non-linear mathematical models," *Mathematical modelling and computational experiment*, vol. 1, pp. 407–414, 1993.

[125] I. M. Sobol, "Global sensitivity indices for nonlinear mathematical models and their Monte Carlo estimates," *Mathematics and computers in simulation*, vol. 55, no. 1-3, pp. 271–280, 2001.

[126] S. Chib and E. Greenberg, "Understanding the metropolis-hastings algorithm," *The american statistician*, vol. 49, no. 4, pp. 327–335, 1995.

[127] G. Casella and E. I. George, "Explaining the Gibbs sampler," *The American Statistician*, vol. 46, no. 3, pp. 167–174, 1992.

[128] M. K. Pitt and N. Shephard, "Filtering via simulation: Auxiliary particle filters," *Journal of the American statistical association*, vol. 94, no. 446, pp. 590–599, 1999.

[129] D. Yazdani, R. Cheng, D. Yazdani, J. Branke, Y. Jin, and X. Yao, "A survey of evolutionary continuous dynamic optimization over two decades — part A," *IEEE Transactions on Evolutionary Computation*, vol. 25, no. 4, pp. 609–629, 2021.

[130] D. Yazdani, R. Cheng, D. Yazdani, J. Branke, Y. Jin, and X. Yao, "A survey of evolutionary continuous dynamic optimization over two decades — part B," *IEEE Transactions on Evolutionary Computation*, vol. 25, no. 4, pp. 630–650, 2021.

[131] S. Ruder, "An overview of gradient descent optimization algorithms," *arXiv preprint arXiv:1609.04747*, 2016.

[132] J. Kennedy and R. Eberhart, "Particle swarm optimization," in *Proceedings of ICNN'95-International Conference on Neural Networks*, vol. 4, pp. 1942–1948, IEEE, 1995.

[133] S. Sengupta, S. Basak, and R. A. Peters, "Particle swarm optimization: A survey of historical and recent developments with hybridization perspectives," *Machine Learning and Knowledge Extraction*, vol. 1, no. 1, pp. 157–191, 2018.

[134] O. Farges, J.-J. Bézian, and M. El Hafi, "Global optimization of solar power tower systems using a Monte Carlo algorithm: Application to a redesign of the PS10 solar thermal power plant," *Renewable Energy*, vol. 119, pp. 345–353, 2018.

[135] X. Ye, B. Chen, P. Li, L. Jing, and G. Zeng, "A simulation-based multi-agent particle swarm optimization approach for supporting dynamic decision making in marine oil spill responses," *Ocean & Coastal Management*, vol. 172, pp. 128–136, 2019.

[136] T. T. Nguyen, S. Yang, and J. Branke, "Evolutionary dynamic optimization: A survey of the state of the art," *Swarm and Evolutionary Computation*, vol. 6, pp. 1–24, 2012.

[137] M. Mavrovouniotis, C. Li, and S. Yang, "A survey of swarm intelligence for dynamic optimization: Algorithms and applications," *Swarm and Evolutionary Computation*, vol. 33, pp. 1–17, 2017.

[138] D. Whitley, "A genetic algorithm tutorial," *Statistics and computing*, vol. 4, no. 2, pp. 65–85, 1994.

[139] S. Katoch, S. S. Chauhan, and V. Kumar, "A review on genetic algorithm: past, present, and future," *Multimedia Tools and Applications*, vol. 80, no. 5, pp. 8091–8126, 2021.

[140] A. Shukla, H. M. Pandey, and D. Mehrotra, "Comparative review of selection techniques in genetic algorithm," in *2015 international conference on futuristic trends on computational analysis and knowledge management (ABLAZE)*, pp. 515–519, IEEE, 2015.

[141] A. J. Umbarkar and P. D. Sheth, "Crossover operators in genetic algorithms: a review.," *ICTACT journal on soft computing*, vol. 6, no. 1, 2015.

[142] A. Hassanat, K. Almohammadi, E. Alkafaween, E. Abunawas, A. Hammouri, and V. S. Prasath, "Choosing mutation and crossover ratios for genetic algorithms—a review with a new dynamic approach," *Information*, vol. 10, no. 12, p. 390, 2019.

[143] S. N. Ghoreishi, A. Clausen, and B. N. Jørgensen, "Termination criteria in evolutionary algorithms: A survey.," in *IJCCI*, pp. 373–384, 2017.

[144] G. Hornby, A. Globus, D. Linden, and J. Lohn, "Automated antenna design with evolutionary algorithms," in *Space 2006*, p. 7242, 2006.

[145] F. Dharma, S. Shabrina, A. Noviana, M. Tahir, N. Hendrastuty, and W. Wahyono, "Prediction of indonesian inflation rate using regression model based on genetic algorithms," *Jurnal Online Informatika*, vol. 5, no. 1, pp. 45–52, 2020.

[146] G. Welch, G. Bishop, *et al.*, "An introduction to the kalman filter," 1995.

[147] A. G. Wills and T. B. Schön, "Sequential Monte Carlo: A unified review," *Annual Review of Control, Robotics, and Autonomous Systems*, vol. 6, pp. 159–182, 2023.

[148] J. Lee, D. D. McManus, P. Bourrell, L. Sörnmo, and K. H. Chon, "Atrial flutter and atrial tachycardia detection using Bayesian approach with high resolution time–frequency spectrum from ECG recordings," *Biomedical Signal Processing and Control*, vol. 8, no. 6, pp. 992–999, 2013.

[149] V. Nathan and R. Jafari, "Particle filtering and sensor fusion for robust heart rate monitoring using wearable sensors," *IEEE journal of biomedical and health informatics*, vol. 22, no. 6, pp. 1834–1846, 2017.

[150] C. P. Bridge, C. Ioannou, and J. A. Noble, "Automated annotation and quantitative description of ultrasound videos of the fetal heart," *Medical image analysis*, vol. 36, pp. 147–161, 2017.

[151] R. Douc, A. Garivier, E. Moulines, and J. Olsson, "Sequential Monte Carlo smoothing for general state space hidden markov models," 2011.

[152] N. Chopin, O. Papaspiliopoulos, *et al.*, *An introduction to sequential Monte Carlo*, vol. 4. Springer, 2020.

[153] M. A. Beaumont, J.-M. Cornuet, J.-M. Marin, and C. P. Robert, "Adaptive approximate Bayesian computation," *Biometrika*, vol. 96, no. 4, pp. 983–990, 2009.

[154] B. M. Turner and T. Van Zandt, "A tutorial on approximate Bayesian computation," *Journal of Mathematical Psychology*, vol. 56, no. 2, pp. 69–85, 2012.

[155] L. B. Sheiner and T. H. Grasela, "An introduction to mixed effect modeling: concepts, definitions, and justification," *Journal of pharmacokinetics and biopharmaceutics*, vol. 19, no. 3, pp. S11–S24, 1991.

[156] A. L. Oberg and D. W. Mahoney, "Linear mixed effects models," *Topics in biostatistics*, pp. 213–234, 2007.

[157] X. A. Harrison, L. Donaldson, M. E. Correa-Cano, J. Evans, D. N. Fisher, C. E. Goodwin, B. S. Robinson, D. J. Hodgson, and R. Inger, "A brief introduction to mixed effects modelling and multi-model inference in ecology," *PeerJ*, vol. 6, p. e4794, 2018.

[158] C. T. Leffler, J. P. Saul, and R. J. Cohen, "Rate-related and autonomic effects on atrioventricular conduction assessed through beat-to-beat PR interval and cycle length variability," *Journal of cardiovascular electrophysiology*, vol. 5, no. 1, pp. 2–15, 1994.

[159] A. L. Goldberger, L. A. Amaral, L. Glass, J. M. Hausdorff, P. C. Ivanov, R. G. Mark, J. E. Mietus, G. B. Moody, C.-K. Peng, and H. E. Stanley, "Physiobank, physiotoolkit, and physionet: Components of a new research resource for complex physiologic signals," *Circulation [Online]*, vol. 101, no. 23, pp. e215–e220, 2000.

[160] R. H. Anderson, D. Sánchez-Quintana, S. Mori, Y. Lokhandwala, F. S. Correa, H. J. Wellens, and E. B. Sternick, "Unusual variants of pre-excitation: from anatomy to ablation: Part i—understanding the anatomy of the variants of ventricular pre-excitation," *Journal of Cardiovascular Electrophysiology*, vol. 30, no. 10, pp. 2170–2180, 2019.

Part II

Included Papers

Paper I

frontiers in Physiology

ORIGINAL RESEARCH
published: 28 October 2021
doi: 10.3389/fphys.2021.728955

Non-invasive Characterization of Human AV-Nodal Conduction Delay and Refractory Period During Atrial Fibrillation

Mattias Karlsson[1,2], *Frida Sandberg*[2]*, *Sara R. Ulimoen*[3] *and Mikael Wallman*[1]

[1] *Department of Systems and Data Analysis, Fraunhofer-Chalmers Centre, Gothenburg, Sweden,* [2] *Department of Biomedical Engineering, Lund University, Lund, Sweden,* [3] *Department of Medical Research, Vestre Viken Hospital Trust, Bærum Hospital, Drammen, Norway*

During atrial fibrillation (AF), the heart relies heavily on the atrio-ventricular (AV) node to regulate the heart rate. Thus, characterization of AV-nodal properties may provide valuable information for patient monitoring and prediction of rate control drug effects. In this work we present a network model consisting of the AV node, the bundle of His, and the Purkinje fibers, together with an associated workflow, for robust estimation of the model parameters from ECG. The model consists of two pathways, referred to as the slow and the fast pathway, interconnected at one end. Both pathways are composed of interacting nodes, with separate refractory periods and conduction delays determined by the stimulation history of each node. Together with this model, a fitness function based on the Poincaré plot accounting for dynamics in RR interval series and a problem specific genetic algorithm, are also presented. The robustness of the parameter estimates is evaluated using simulated data, based on clinical measurements from five AF patients. Results show that the proposed model and workflow could estimate the slow pathway parameters for the refractory period, R^{SP}_{min} and ΔR^{SP}, with an error (mean ± std) of 10.3 ± 22 and −12.6 ± 26 ms, respectively, and the parameters for the conduction delay, $D^{SP}_{min,tot}$ and ΔD^{SP}_{tot}, with an error of 7 ± 35 and 4 ± 36 ms. Corresponding results for the fast pathway were 31.7 ± 65, −0.3 ± 77, 17 ± 29, and 43 ± 109 ms. These results suggest that both conduction delay and refractory period can be robustly estimated from non-invasive data with the proposed methodology. Furthermore, as an application example, the methodology was used to analyze ECG data from one patient at baseline and during treatment with Diltiazem, illustrating its potential to assess the effect of rate control drugs.

Keywords: atrial fibrillation, atrioventricular node, rate control, mathematical modeling, genetic algorithm, ECG, cardiac electrophysiology

OPEN ACCESS

Edited by:
Axel Loewe, Karlsruhe Institute of Technology (KIT), Germany

Reviewed by:
Andreu M. Climent, Universitat Politècnica de València, Spain
Eugenio Ricci, University of Bologna, Italy

***Correspondence:**
Frida Sandberg
frida.sandberg@bme.lth.se

Specialty section:
This article was submitted to Cardiac Electrophysiology, a section of the journal Frontiers in Physiology

Received: *22 June 2021*
Accepted: *29 September 2021*
Published: *28 October 2021*

Citation:
Karlsson M, Sandberg F, Ulimoen SR and Wallman M (2021) Non-invasive Characterization of Human AV-Nodal Conduction Delay and Refractory Period During Atrial Fibrillation. Front. Physiol. 12:728955. doi: 10.3389/fphys.2021.728955

1. INTRODUCTION

Atrial fibrillation (AF) is the most widespread sustained cardiac arrhythmia with an estimated prevalence of 2–4% in the adult population (Benjamin et al., 2019). During AF, the electrical activity in the atria is highly disorganized, leading to a rapid and irregular ventricular rhythm. In order to reduce these effects, rate control drugs constitute one of the primary therapeutic options

(Hindricks et al., 2020). These drugs are not designed to terminate AF, but rather to lower the heart rate. They do this by modulating the conduction through the AV node, preventing some electrical signals emanating from the atria from being transmitted to the ventricles, thereby reducing the ventricular activation rate. Thus, rate control is often sufficient to improve AF-related symptoms (Hindricks et al., 2020). The choice of first-line rate control drugs can vary between beta-blockers and non-dihydropyridine calcium channel blockers, with digoxin as a second-line option (Hindricks et al., 2020). However, the current method of finding the best treatment for a given patient is largely based on trial and error (Hindricks et al., 2020). Thus, patient specific characterization of AV node properties would be beneficial to achieve optimal rate control.

Functionally, the AV node consists of two pathways, connected to each other before entering the bundle of His (Kurian et al., 2010). The two pathways are referred to as the slow pathway (SP) and the fast pathway (FP), where the FP conducts impulses faster than SP but has a longer refractory period. During sinus rhythm, the impulses are typically conducted through the FP due to its faster conduction rate. During AF, however, conduction may alternate between SP and FP as a result of the rapid arrival of atrial impulses. This, together with concealed conduction, i.e., impulses inside the AV node that do not lead to ventricular activation but still affect the conduction characteristics of following impulses, gives rise to the complex blocking and delay behavior the AV node has been shown to possess.

In order to understand this blocking and delay behavior, mathematical modeling has become an increasingly important tool. Several models of the AV node and its function during AF have previously been proposed, including various descriptions of the conduction delay (Jørgensen et al., 2002; Mangin et al., 2005; Climent et al., 2011) and the refractory period (Rashidi and Khodarahmi, 2005). A model for simulating the ventricular activation capable of replicating both conduction delay and refractory period during AF was proposed by Lian et al. (2006). Another model capable of replicating both conduction delay and refractory period, based on the action potential of the AV node cells and modeled by ordinary differential equations, was proposed by Inada et al. (2009).

However, none of these models were developed with the purpose of ECG based estimation of AV node parameters on a patient specific basis. The models presented in Rashidi and Khodarahmi (2005) and Lian et al. (2006) did not fit parameter values to data, the models presented in Climent et al. (2011) and Inada et al. (2009) were fitted to data from rabbits. The models presented in Jørgensen et al. (2002) and Mangin et al. (2005) were fitted to AF patients, but invasive data was required. To make a model useful in a clinical setting, it should ideally allow for fitting to non-invasive data such as surface electrocardiogram (ECG). A statistical model developed for estimation of AV node parameters from ECG data during AF was first presented in Corino et al. (2011). This model has later been updated and proven to replicate patient specific histograms of the time series between two successive R waves on the ECG (RR interval series) extracted from ECG data, as well as to assess the effect of rate control drugs on the AV node (Henriksson et al., 2015). It is a lumped model structure that still accounts for concealed conduction, relative refractoriness, and dual pathways. However, it lumps conduction delay and refractory period together, making the estimated model parameters difficult to interpret.

In this work we present a network model of the AV node, able to estimate patient specific conduction delay and refractory period from ECG, building on previous work presented in Wallman and Sandberg (2018). The model consists of interconnected nodes forming two pathways, providing a balance between complexity and computational efficiency, and represents both spatial and temporal dynamics of the AV-node. With novel additions to the model structure by including effects from the bundle of His and Purkinje fibers, as well as a tailored workflow taking advantage of dynamics in the data, the model allows for estimation of parameters governing both refractory period and conduction delay in a robust manner from non-invasive data during AF. The ultimate aim of this work is to monitor and predict the outcome of treatment with rate control drugs in clinical settings to assist in treatment selection. In order to do this, a robust characterization of the AV node is needed, and thus the purpose of this study is to: (1) Describe and motivate the model; (2) Present a tailored workflow for estimation of parameters; (3) Demonstrate that presented combination of model and workflow leads to robust parameter estimates that mimic measured data well.

2. MATERIALS AND METHODS

The model of the AV node will be explained in section 2.1, followed by a description of the data used to evaluate said model in sections 2.2 and 2.3. In section 2.4, the methodology for model parameter estimation is explained; which combined with the optimization algorithm described in section 2.5 constitutes the workflow.

2.1. Network Model of the Human AV Node

The model of the AV node, shown in **Figure 1**, consists of a network of nodes and is based on the model presented in Wallman and Sandberg (2018). The model consists of two pathways, representing the SP and the FP, connected with a coupling node. Each pathway is modeled with 10 nodes, where each node corresponds to a localized part of the AV node. Each node can block incoming impulses or send them through adding a conduction delay. All nodes but the coupling node sends impulses to all other nodes connected to it, whereas the coupling node only receives impulses. A new refractory period $[R_i(n)]$ and conduction delay $[D_i(n)]$ are calculated every time a node (i) receives a new impulse (n). The refractory period and conduction delay are based on the stimulation history of the node and are described using exponential functions. These exponential functions have previously been used to fit AV node characteristics (Shrier et al., 1987; Lian et al., 2006; Wallman and Sandberg, 2018), and can be seen in Equations (1–3).

$$R_i(n) = R_{min} + \Delta R(1 - e^{-\tilde{I}_i(n)/\tau_R}) \quad (1)$$

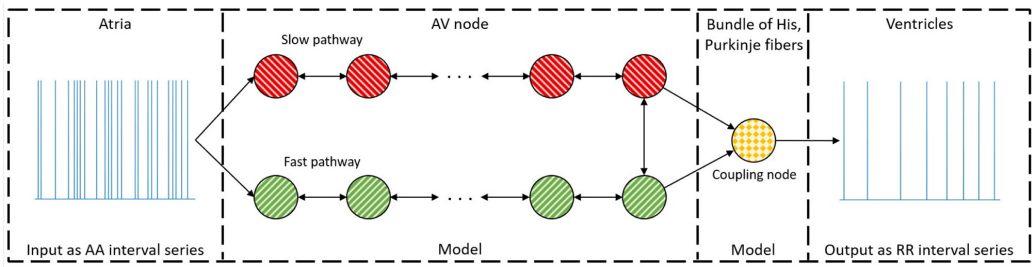

FIGURE 1 | A schematic representation of the proposed model. The arrow indicates the direction an impulse can conduct, and the colors represent nodes with the same parameter sets. For simplicity, only a subset of the ten nodes in each pathway are showed.

$$D_i(n) = D_{min} + \Delta D e^{-\tilde{t}_i(n)/\tau_D} \tag{2}$$

$$\tilde{t}_i(n) = t_i(n) - t_i(n-1) - R_i(n-1) \tag{3}$$

Here $\tilde{t}_i(n)$ refers to diastolic interval preceding impulse n, $t_i(n)$ the arrival time of impulse n at node i, and $t_i(n-1)$ and $R_i(n-1)$ the arrival time and refractory period of impulse $n-1$ at node i, respectively. If $\tilde{t}_i(n)$ is negative, the node will still be in its refractory period and thus the impulse will be blocked. The model parameters defining minimum refractory period, R_{min}; maximum prolongation of refractory period, ΔR; time constant τ_R; minimum conduction delay, D_{min}; maximum prolongation of conduction delay, ΔD; and the time constant τ_D, are assumed to be fixed for the nodes in the SP and FP, respectively.

The coupling node models the total refractoriness and conduction delay introduced by the connection between the AV node and the bundle of His, the Purkinje fibers, and the bundle of His. This node has a separate set of parameters, representing separate functional properties, and will be denoted the His and Purkinje (HP) node. The refractory period for the Purkinje fibers is assumed to not affect the ventricular activation during AF. Thus, the whole refractory period for the HP node is determined by the bundle of His. However, the conduction delay for the HP node is viewed as the time it takes an impulse to travel from the start of the bundle of His to the end of the Purkinje fibers. The conduction delay from the start of the bundle of His until the end of the Purkinje fibers has clinically been showed to have a mean of 60 ms with a standard deviation of 10 ms for patients suffering from AF (Deshmukh et al., 2000). Thus, the conduction delay for the HP node is fixed at 60 ms. The HP node's refractory period is estimated by the mean of the ten shortest RR intervals, RR_{min}.

This results in 12 free parameters for the proposed model, denoted as a parameter vector $\theta = [R^{FP}_{min}, \Delta R^{FP}, \tau^{FP}_R, R^{SP}_{min}, \Delta R^{SP}, \tau^{SP}_R, D^{FP}_{min}, \Delta D^{FP}, \tau^{FP}_D, D^{SP}_{min}, \Delta D^{SP}, \tau^{SP}_D]$. It is assumed that the first node of each pathway is simultaneously stimulated for incoming impulses from the atria. The model can then be used to produce a RR interval series with minimal computational demands using a modified version of Dijkstra's algorithm (Wallman and Sandberg, 2018). A link to the code for the model together with a basic user example can be found at section 5. The total minimum conduction delay and maximum prolongation, defined as $D^{FP}_{min,tot} = N_n D^{FP}_{min}$; $\Delta D^{FP}_{tot} = N_n \Delta D^{FP}$; $D^{SP}_{min,tot} = N_n D^{SP}_{min}$; $\Delta D^{SP}_{tot} = N_n \Delta D^{SP}$; where $N_n = 10$ are the number of nodes in each pathway, are introduced for convenience of presentation.

2.2. ECG Data

This study was based on ambulatory ECG data from the RATe control in Atrial Fibrillation (RATAF) study, which is approved by the regional ethics committee and the Norwegian medicines agency and was conducted in accordance with the Helsinki Declaration (Ulimoen et al., 2013). The RATAF study contains 24-h Holter recordings of 60 patients under baseline and during treatment with four different rate reducing drugs. All patients had permanent AF, no heart failure or symptomatic ischemic heart disease, an age of 71 ± 9 (mean ± std), and 70% were men. To evaluate the presented model, we selected 15 min ECG segments, one for each of five patients, obtained under baseline conditions between 1:00 and 3:00 pm. These five patients were selected to be representative for the whole data set, with varying RR interval series characteristics and an average heart rate ranging between 63 and 140 bpm. In addition, corresponding ECG data obtained during treatment with Diltiazem was also used for one of the five patients.

The RR interval series were extracted from the ECG signals by first detecting the R peaks, before removing RR intervals preceding and following ectopic beats identified based on heartbeat morphology (Lagerholm et al., 2000). Along with this, the mean arrival rate of the atrium-to-atrium (AA) intervals was estimated from the f-waves in the ECG by first extracting the atrial activity from the ECG using spatiotemporal QRST cancellation (Stridh and Sornmo, 2001), before tracking the atrial fibrillatory rate (AFR) using a method based on a hidden Markov model (Sandberg et al., 2008). Finally, correction of the atrial fibrillatory rate by taking the atrial depolarization time into account was used to obtain an estimate of the arrival rate. Here, we denote the true mean arrival rate λ, and the estimated mean arrival rate $\hat{\lambda}$. One value of $\hat{\lambda}$ was obtained for each ECG segment (Corino et al., 2013).

TABLE 1 | Characteristics of the data extracted from ECG and the simulated data, respectively, for all five patients.

Parameter	Patient 1	Patient 2	Patient 3	Patient 4	Patient 5
MEASURED DATA					
Average HR (ms)	76.4	62.7	90.6	111.9	139.9
$\hat{\lambda}$ (Hz)	8.45	9.13	6.73	9.03	10.04
SIMULATED DATA					
Average HR (bpm)	75.3	62.3	93.1	110.5	139.5
λ (Hz)	8.45	9.13	6.73	9.03	10.04
SP ratio (%)	54	60	85	77	92
R_{min}^{FP} (ms)	210	390	379	465	378
ΔR^{FP} (ms)	516	475	594	1.47	383
τ_R^{FP} (ms)	168	217	222	113	145
R_{min}^{SP} (ms)	205	313	280	257	287
ΔR^{SP} (ms)	469	422	233	0.00	103
τ_R^{SP} (ms)	220	40	204	172	227
D_{min}^{FP} (ms)	4.77	1.13	1.44	9.05	6.43
ΔD^{FP} (ms)	11.2	20.6	16.0	20.3	34.4
τ_D^{FP} (ms)	155	237	40.0	40.0	145
D_{min}^{SP} (ms)	21.1	25.4	21.7	16.0	20.2
ΔD^{SP} (ms)	51.9	15.1	4.62	3.74	2.47
τ_D^{SP} (ms)	89.9	232	166	91.1	165

2.3. Simulated Data

Simulated data were created by fitting the model to the RR interval series from the five patients, cf. section 2.5, and using the resulting estimated model parameters to simulate an RR interval series of 20 min. The sequence of atrial impulses arriving to the AV node, and thus the input to the model, were simulated using a Poisson process with the mean arrival rate set to the value of $\hat{\lambda}$ estimated for each patient (Corino et al., 2011; Henriksson et al., 2015). The parameter values used for the simulated data, along with average heart rate of the simulated RR interval series, are summarized in **Table 1**.

2.4. Model Parameter Estimation

To evaluate how well the model matches the extracted RR interval series, a fitness function comparing the model output to the RR interval series is used. In order to take the dynamics of the RR interval series into account, the Poincaré plot is used as a basis for the fitness function. The Poincaré plot is a scatter plot of successive pairs of RR intervals. To use the Poincaré plot as a fitness function, the RR interval series is binned into two dimensional bins centered between 250 and 1,800 ms in steps of 50 ms, resulting in $N = 961$ bins. The error function is computed according to Equation (4).

$$\epsilon = \frac{1}{N}\sum_{i=1}^{N}\left((x_i - \tilde{x}_i)^2/\sqrt{\tilde{x}_i}\right) \tag{4}$$

Here ϵ is the error value, and $\tilde{x}_i$ and x_i the number of RR intervals, in the i-th bin, of the measured data and model output, respectively. The normalization by $\sqrt{\tilde{x}_i}$ is introduced to avoid bins with a large number of data points to dominate the optimization. The square root is used as a trade-off between no normalization, making the bins with a large number of data points dominate, and normalization with the whole measured bin counts, making the accuracy of every bin have the same weight regardless of how much of the data are in that bin. A schematic representation of the parameter estimation process can be seen in **Figure 2**.

2.5. Genetic Algorithm

An initial study of how ϵ varies with varying model parameter values revealed a highly chaotic structure with a large number of local minima. This prompted us to minimize ϵ using a genetic algorithm (GA). A brief description of the algorithm is given below, with more detailed information in the **Supplementary Section 1**. Due to the high dimensional parameter space and the risk of premature convergence early in the optimization, a variant of an island model was used (Wahde, 2008). A schematic representation of the GA is shown in **Figure 3**. As visible in the figure, the full GA can be divided into two sections. The first section consists of five separate GA. This was implemented by restarting the algorithm five times with 300 individuals in each generation. The individuals in each starting run were initialized using a latin hypercube sampling in the ranges: $\{R_{min}^{SP}, R_{min}^{FP}\} \in [250, 600]$ *ms*; $\{\Delta R^{SP}, \Delta R^{FP}\} \in [0, 600]$ *ms*, $\{\tau_R^{SP}, \tau_R^{FP}\} \in [50, 300]$ *ms*; $\{D_{min}^{SP}, D_{min}^{FP}\} \in [0, 30]$ *ms*; $\{\Delta D^{SP}, \Delta D^{FP}\} \in [0, 75]$ *ms*; $\{\tau_D^{SP}, \tau_D^{FP}\} \in [50, 300]$ *ms*. These starting runs last for six generations, and after each run the best 150 of the individuals are saved and used in the second section, the main GA. Thus, the main GA uses a population

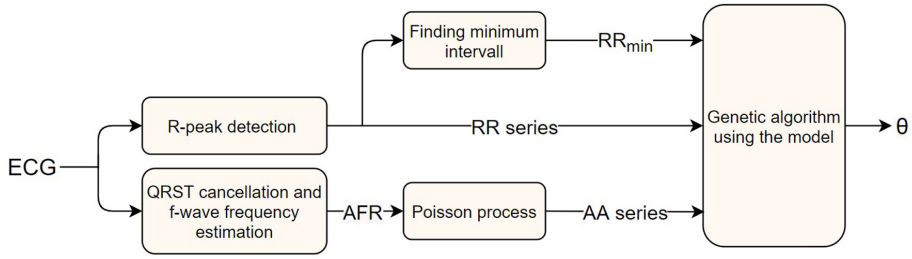

FIGURE 2 | A block diagram of the AV node model parameter estimation workflow, starting with a measured ECG signal and ending with estimated parameters.

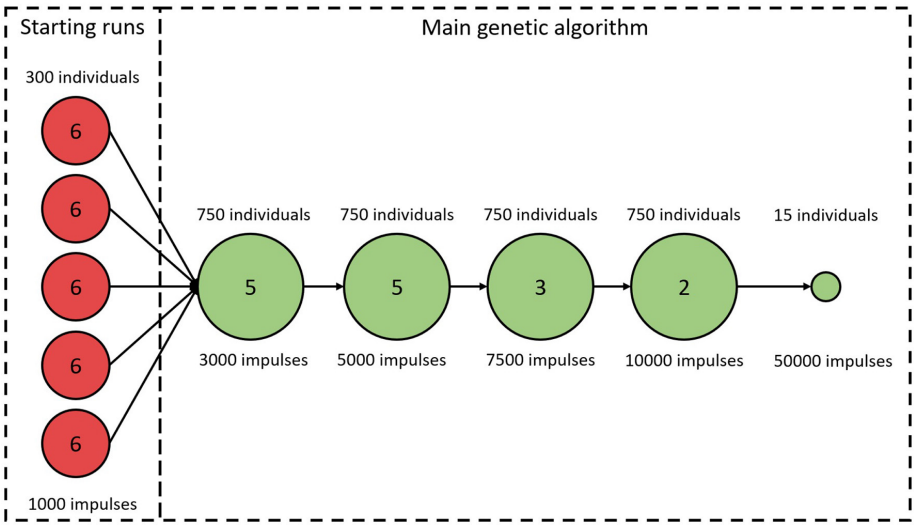

FIGURE 3 | A schematic representation of the genetic algorithm. Circles represent stages of the algorithm with constant number of individuals and L_{RR}. Numbers in circles correspond to the number of iterations before proceeding to the next stage. The last stage is always used, even if the GA terminates early.

of 750 individuals in each generation. For both the starting runs and the main GA, the 2.5% fittest individuals in each generation survives into the next generation unchanged, whereas the remaining individuals are created via tournament selection, two-point crossover, and creep mutation (Wahde, 2008). In order to avoid premature convergence, both incest prevention in the form of mating restriction between too similar individuals during crossover, and a varying mutation rate depending on the diversity of the individuals in each generation were implemented (Wahde, 2008). This process of selection, crossover, and mutation is then continued until termination. The termination of the starting runs always occurs after six generations. The termination for the main GA occurs either when ϵ for the fittest individual in each generation does not change for three generations, or when 15 generations have been run. The fittest individual for the k-th generation, $\hat{\epsilon}_k$, is deemed to have changed if the difference between $\bar{\hat{\epsilon}}(k)$ and $\bar{\hat{\epsilon}}(k-2)$, seen in Equation (5), is lower than 25.

$$\bar{\hat{\epsilon}}(k) = \frac{\hat{\epsilon}_k + \hat{\epsilon}_{k-1} + \hat{\epsilon}_{k-2}}{3} \tag{5}$$

As described in section 2.3, a Poisson process with mean arrival rate $\hat{\lambda}$ was used as input to the model, and due to the stochastic nature of the Poisson process, ϵ varies between realizations. The magnitude of this variation was analyzed by finding a parameter set replicating the extracted RR interval series from patient 3 well, before simulating that parameter set with different lengths of the resulting RR interval series, L_{RR}, as seen in **Figure 4**, left panel. Each L_{RR} was simulated 1,000 times. Moreover, six more

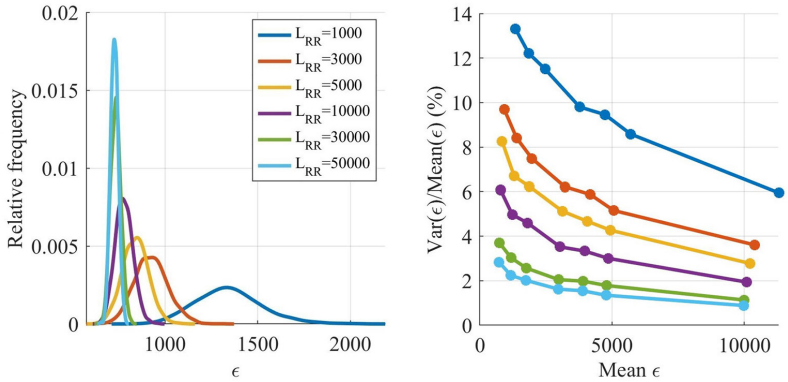

FIGURE 4 | Estimated distribution of ϵ as a function of L_{RR} **(left)**. Variance of ϵ divided by mean of ϵ as a function of the mean of ϵ **(right)**.

parameter sets with increasing ϵ were also simulated 1,000 times with the same L_{RR}, as seen in **Figure 4**, right panel.

The ϵ variation is decreasing with larger L_{RR}, however, the running time for the model is linearly increasing with L_{RR}, and thus shorter outputs are preferable. The variation of ϵ is not as important early in the optimization since the variation relative ϵ is smaller for larger ϵ, see **Figure 4**, right panel. However, after several generations most of the ϵ for individuals found by the GA are low, and thus the variability in ϵ has a larger impact on the algorithm. Therefore, L_{RR} is increased throughout the optimization.

As seen in **Figure 3**, the L_{RR} for all generations in the starting runs were 1,000 impulses. For the main GA, the first five generations used a L_{RR} of 3,000 impulses, the following five generations a L_{RR} of 5,000 impulses, followed by three generations with length of 7,500 impulses, before ending with two 10,000 impulses long generations. To obtain a robust estimate of $\bar{\hat{\epsilon}}(k)$, the individual with the best fit in each generation is evaluated again with a L_{RR} of 10,000. After termination for the main GA, the 15 fittest individuals were tested again, with a L_{RR} of 50,000; this in order to select the fittest individual with a low variation in ϵ.

3. RESULTS

The RR interval series extracted from the ECG along with the simulated data, cf. sections 2.2 and 2.3, are used to evaluate the proposed methodology. In section 3.1, the proposed approach for optimization is compared to using only the main GA with fixed L_{RR}. The robustness and precision of the parameter estimation are evaluated using simulated data in section 3.2. Further, the robustness of the estimates is set in perspective by using the model to estimate AV node characteristics for one of the patients during both baseline and under influence of the calcium channel blocker drug Diltiazem. In section 3.3, the proposed model is compared to the model presented in Wallman and Sandberg (2018).

3.1. Genetic Algorithm

The effect of using an island based start together with varying L_{RR} was evaluated by comparing it to using only the main GA, as described in section 2.5, with L_{RR} fixed at 5,000. The initialization for this fixed GA was the same as for the starting runs, a latin hypercube sampling in the same ranges, and the population size was again 750. Performances of the two methods were evaluated by comparing the error value of the fittest individual for each generation, $\hat{\epsilon}_k$ with the cumulative L_{RR} used for the evaluations, i.e., the accumulated total number of impulses in each generation. For the different starting runs, all runs were computed in parallel so that $\hat{\epsilon}_k$ during this stage is the lowest value out of all the five starting runs. The average results from comparing the two versions of the GA on all five patients, each 100 times, are shown in **Figure 5**. From this it is possible to see that a lower $\hat{\epsilon}_k$, and thus a better fit to the RR interval series, can be found in less computational time using the proposed methodology. For reference, estimating the parameters for one patient using a single core on a standard desktop computer (Intel® Core™ i7-6600U Processor, @ 2.60GHz) requires on average 20 min, with variations due to the different terminating requirements for the GA. It is also possible to see that the termination criteria for a maximum number of generations stated in section 2.5 is typically achieved after the GA has converged.

3.2. Parameter Estimation Robustness

Simulated RR interval series were used to evaluate the robustness of the model parameter estimates. The results from optimizing the model 200 times for the five simulated RR interval series can be seen in **Table 2**, where the mean and standard deviation for each of the 12 estimated parameters, for each of the five patients, are listed. Moreover, the mean error, defined as the difference between the mean value of the estimated parameter

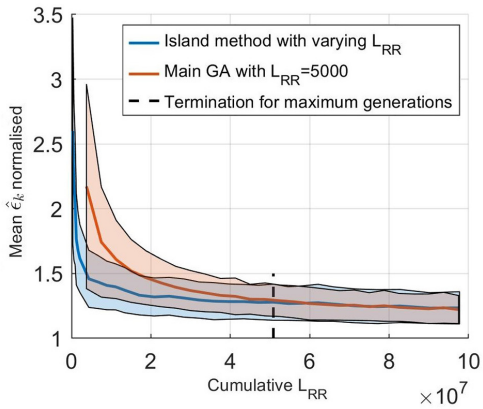

FIGURE 5 | (solid line) Mean normalized $\hat{\epsilon}_k$ of 100 optimizations of the five set of patient data as a function of cumulative L_{RR} for (blue) the island start optimization with varying L_{RR} and (orange) only the main GA with a fix L_{RR} at 5,000. The shaded background represents one standard deviation. Here, $\hat{\epsilon}_k$ is normalized with the best ϵ found for each patient, to account for the fact that the model can not fit each RR interval series equally well.

and the ground truth, averaged over the five patients, are also listed. Furthermore, the mean and standard deviation of the error normalized with respect to the parameter ranges, cf. section 2.5, are presented. From the SP ratio it is evident that the SP is used more for transmission, and from the normalized error, it is evident that the parameters associated with the SP are more robustly estimated. The histogram and Poincaré plots for the five simulated patients with the transmission pathway for each RR interval marked out can be seen in **Supplementary Section 3**, together with the simulated histograms showing the effect of changes to λ.

To set the robustness in perspective, the AV nodal properties were estimated 200 times for a single patient during baseline and under the influence of the non-dihydropyridine calcium channel blocker rate control drug Diltiazem. The results, shown in **Figure 6**, indicate that the uncertainty in the parameter estimation is sufficiently low in order to reveal the drug effect.

3.3. Model Comparison

To evaluate the ability of the model and proposed workflow to represent AF data and to have a frame of reference, the proposed model is compared with the model presented in Wallman and Sandberg (2018); henceforth denoted the reference model. Both models were fitted to the RR interval series from one example patient, and the properties of the resulting simulated RR interval series are shown in the form of histograms, Poincaré plots, and autocorrelations, as seen in **Figure 7**. For both models, the optimizer was run until no change in error value for the fittest individual during ten generations occurred, to assure convergence. Both models used the optimizer described in section 2.5, but the reference model uses a fitness function based on the histogram (Wallman and Sandberg, 2018). It is clear from both the Poincaré plots and the autocorrelation plots that the proposed model can better replicate the dynamics of the RR interval series. The fit to the Poincaré plot can be quantified by the resulting ϵ, which for the proposed model was 1,360, compared to 6,740 for the reference model. Similarly, the value for the first lag autocorrelation was −0.07 for the proposed model and 0.52 for the reference, compared to the ground truth at −0.07.

4. DISCUSSION

In this study, a mathematical model of the AV node, bundle of His, and Purkinje network has been presented together with a fitness function accounting for RR interval dynamics and genetic algorithm tailored to the model. The model and workflow have been evaluated with respect to robustness, accuracy, and ability to represent data, using both measured and simulated data.

Ten nodes in each pathway were used as a trade-off between detail and computation time. A small number of nodes can make the conduction delay larger than the refractory period, allowing impulses to bounce back and forth, whereas a large number of nodes leads to a higher computational demand. The inclusion of a last node in the model as functionally distinct from the SP and FP has previously been used in other models of the AV node (Inada et al., 2009). The incorporation of separate conduction properties for the connecting node introduced both new refractory period and conduction delay parameters. However, literature data suggests that inter-patient variability in conduction time over the bundle of His and the Purkinje network is around 10 ms (Deshmukh et al., 2000), indicating that the parameters representing the conduction delay could be reasonably approximated by a constant value. Furthermore, an initial study was conducted in which the refractory period of the HP node was represented by Equation (1), with three free parameters. This study showed that the parameter values representing the refractory period in the HP node found after optimization matched a constant value of RR_{min}, independent of $\tilde{t}_i(n)$, well; indicating a good approximation (data not shown). For more details about the parameter values of the HP node during the optimizations, see **Supplementary Section 2**.

Reducing the number of free parameters reduces the parameter space in which the GA operates, and in turn decreases the running time as well as increases the robustness for the optimization. The parameters for the HP node were especially advantageous to fix or estimate directly from data. This was partly because the clinical data and analysis of the optimization made it possible, and partly because the most interesting information regarding the AV node is contained in the parameters governing SP and FP. Thus, setting the parameters corresponding to the bundle of His and Purkinje fibers to fixed values enhanced the ability of our method to estimate AV node properties.

The optimizer in this work utilized the fact that the model could be used with varying speed and precision by changing the output length, with higher speed and lower precision at the start and shifting it during the optimization. This change

TABLE 2 | The mean parameter values ± standard deviation of 200 optimizations for the five simulated data sets, together with the mean error ± mean standard deviation for each parameter.

Parameter	Patient 1	Patient 2	Patient 3	Patient 4	Patient 5	Error	Normalized error (%)
R_{min}^{FP} (ms)	311 ± 104	394 ± 53	430 ± 49	424 ± 45	419 ± 72	31.7 ± 65	7.9 ± 16
ΔR^{FP} (ms)	436 ± 74	495 ± 57	479 ± 55	164 ± 131	393 ± 69	-0.3 ± 77	-0.1 ± 12
τ_R^{FP} (ms)	184 ± 38	211 ± 35	168 ± 39	183 ± 63	167 ± 53	9.4 ± 45	3.6 ± 17
R_{min}^{SP} (ms)	225 ± 17	369 ± 71	271 ± 11	247 ± 8	281 ± 5	10.3 ± 22	2.6 ± 6
ΔR^{SP} (ms)	430 ± 26	358 ± 60	247 ± 14	28 ± 20	101 ± 4	-12.6 ± 26	-1.9 ± 4
τ_R^{SP} (ms)	201 ± 29	56 ± 10	216 ± 26	204 ± 55	198 ± 41	2.2 ± 32	0.8 ± 12
$D_{min,tot}^{FP}$ (ms)	65 ± 31	36 ± 22	53 ± 21	69 ± 39	92 ± 38	17 ± 29	5.7 ± 10
ΔD_{tot}^{FP} (ms)	188 ± 92	273 ± 9.6	193 ± 95	248 ± 119	336 ± 145	43 ± 109	5.7 ± 15
τ_D^{FP} (ms)	132 ± 48	150 ± 43	133 ± 47	135 ± 47	154 ± 47	17 ± 46	7.1 ± 19
$D_{min,tot}^{SP}$ (ms)	184 ± 36	245 ± 25	246 ± 23	197 ± 47	209 ± 43	7 ± 35	2.5 ± 12
ΔD_{tot}^{SP} (ms)	395 ± 73	214 ± 45	88 ± 19	66 ± 31	35 ± 11	4 ± 36	0.5 ± 5
τ_D^{SP} (ms)	173 ± 33	187 ± 42	167 ± 39	179 ± 55	183 ± 47	29 ± 43	12 ± 18
Average HR (bpm)	75.3 ± 0.7	62.6 ± 0.5	93.6 ± 0.7	110.9 ± 1	139.2 ± 1	0.2 ± 0.8	-
SP ratio (%)	54	60	85	77	92	-	-

The normalized error ± standard deviation as well as the ratio of impulses passing through the SP are also presented.

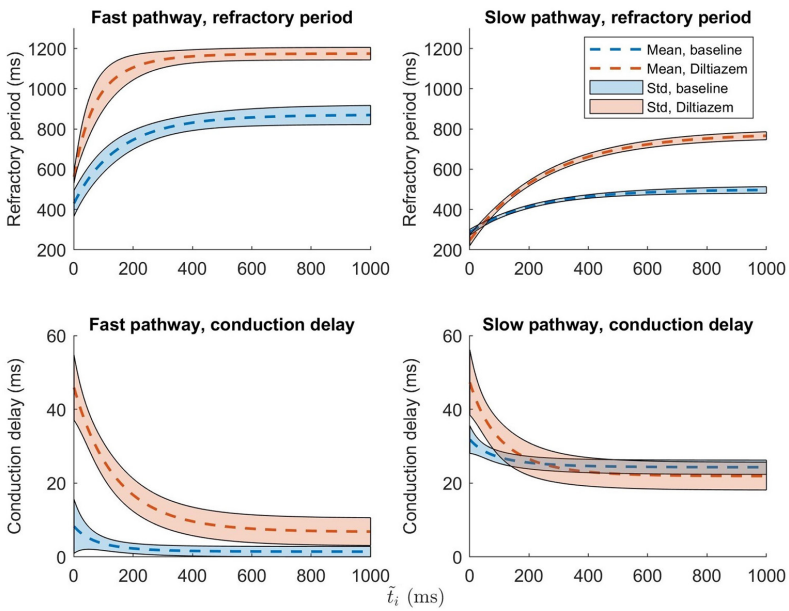

FIGURE 6 | The mean ± one standard deviation, indicated by the shaded background, of the estimate refractory period and conduction delay from Equation (1) and (2), after 200 runs, are plotted for both baseline (blue) and Diltiazem (orange).

in output length also made it possible to run a broad search of the parameter space fast at the start of the optimization by restarting it several times; reducing the risk that a parameter set producing a good fit to the RR interval series was missed. This led to finding parameter sets matching the data faster, as shown in **Figure 5**. With a computing time of 20 min on a standard desktop computer in order to estimate the parameters, it possible to utilize the model without the use of any cloud computing or supercomputer, making it suitable for routine off-line analysis of Holter recordings.

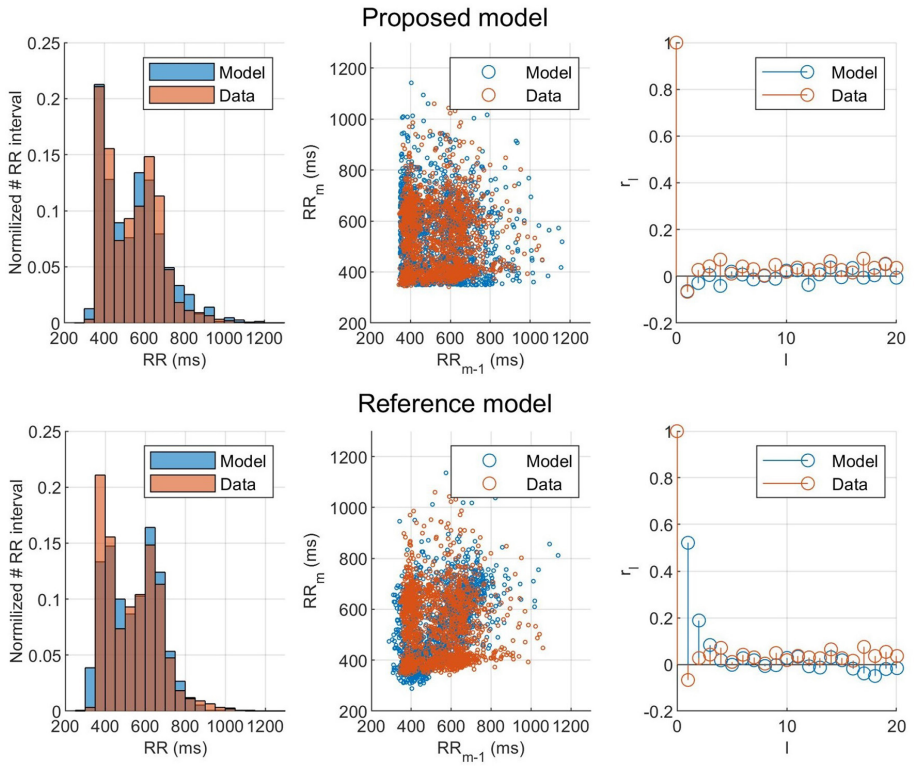

FIGURE 7 | Histogram, Poincaré plot, and autocorrelation representation of the (orange) observed and (blue) modeled RR interval series for **(top)** the fitted proposed model and **(bottom)** the fitted reference model.

The result of taking the RR interval series dynamics into account during the optimization can clearly be seen in **Figure 7**, where the proposed model and fitness function could represent the Poincaré plot with an ϵ five times as low as the reference model. This shows that matching the histograms well, as both models did, does not necessarily mean that the model represents the RR interval dynamics well. Using the Poincaré plot as basis for the fitness function, it was possible to account for the RR interval distribution and the one-step autocorrelation at the same time. It should be noted that the information from the histogram is still indirectly included in the Poincaré plot, which is likely the reason why the proposed fitness function also gave well matched histograms.

Since no ground truth of the estimated parameters is available for the clinical data, it is not possible to directly verify their correctness. However, it is still possible to verify that the parameter values lay within ranges reported in literature. The conduction delay for the HP node is fixed based on clinical data, thus it lies within reasonable ranges by default. The refractory period for the HP node was estimated using RR_{min}, and for the five patients used in this study the range was [292, 655] ms. Comparing this to the bundle branch refractory period of [305, 520] ms, and the His-Purkinje system relative refractory period of [330, 460] ms, reported in Denes et al. (1974), it seems reasonable.

It is difficult to assess AV conduction delay during AF, due to problems in determining which atrial impulse activated the ventricles. However, the total minimum and maximum prolongation of conduction delay parameters of the AV node, $D^{FP}_{min,tot}$, ΔD^{FP}_{tot}, $D^{SP}_{min,tot}$, and ΔD^{SP}_{tot}, have previously been estimated by mathematical models utilizing the relationship between diastolic interval and delay in Equation (2). One such example is the model by Mangin et al. (2005), which uses invasive data, for which the ranges of $D_{min,tot}$, ΔD_{tot}, and τ_D were [80,300], [15,125], and [80,340], respectively. These ranges are of the same order of magnitude as the values obtained for $D_{min,tot}$, ΔD_{tot}, and τ_D in the present study, cf **Table 2**. It should be noted that the present model, contrary to the Mangin model, has two pathways where shorter delays are expected for the FP than for the SP.

The maximum refractory period, defined as the sum of R_{min} and ΔR, can be compared with electrophysiological measurements of the AV node effective refractory period. The values obtained in the present study were in the ranges [466, 973] and [257, 735] ms for the FP and SP, respectively. AV node effective refractory periods from patients with reentrant tachycardia have been reported in the ranges 361 ± 57 and 283 ± 48 ms for the FP and SP, respectively (Natale et al., 1994). As expected, the FP has larger values in both model and measurements.

The use of simulated data was necessary in order to have a ground truth to compare the estimated parameters with and in turn evaluate the methodology. From these five simulated data sets, it is clear that all of them primarily used the SP, cf. **Table 2**, although the SP ratio differed. This higher usage of the SP may be a contributing factor to that the parameters representing the SP were more accurately estimated than the parameters representing the FP. Moreover, the parameters τ_R^{SP}, τ_R^{FP}, τ_D^{SP}, and τ_D^{FP} all have a larger error, which might imply that they have smaller overall effect on the model output. Further, histograms and Poincaré plots highlighting the transmission pathway for the RR intervals (cf. **Supplementary Section 3**) show that longer RR intervals tend to be transmitted via the FP, which is to be expected given its lower total conduction time. More interestingly, it is evident that different histogram peaks generated by the model are not created solely from one pathway, but stem from complex interaction between both the FP and SP. Moreover, it should also be noted that the difference in heart rate between the observed RR interval series and the RR series produced by the fitted model was less than one beat per minute.

It is evident from the example in **Figure 6** that the uncertainty in conduction delay and refractory period introduced by the parameter estimation is generally lower than the effect of the drug, thus suggesting that it is possible to assess the effect of rate control drugs on the AV node from non-invasive data. For the example patient, the difference in conduction delay for the SP between baseline and Diltiazem is minimal for $\tilde{t}_i > 200$ ms. However, one patient is not enough to know if this is a feature specific to this particular patient, a property of the investigated drug, or an artifact of the model formulation. The effect of rate control drugs on the AV node refractory period have previously been investigated (Sandberg et al., 2015), and with the proposed methodology a similar investigation can be done for AV node conduction delay.

4.1. Limitations and Future Work

The main limitation of the present study is the lack of comparison between the estimated parameter and the ground truth AV node characteristics, making the results more difficult to evaluate. Although simulated data was used as a substitute, it is not fully known how closely it matches reality. Another limitation is the assumption that both pathways are activated simultaneously, an assumption that may not be valid, since the electrical activity in the atria is highly disorganized. The variation in output originating from the stochastic input sequence can also be seen as a limitation to the proposed model, since the output for a single set of parameters can vary depending on the realization of the input sequence. However, without electrical measurements in the atria, it is not possible to model the exact behavior of the AV node.

Moreover, due to the computational time of estimating the parameters for each simulated RR interval series 200 times, only a subset of RATAF was used. However, the five patients were selected to ensure a representative subset based on their RR interval series characteristics. It should be noted that the focus of the present study is to evaluate the robustness in parameter estimation rather than analysis of the RATAF data set. Using the model to analyze the entire RATAF data set, including all patients, drugs, and time segments for outcome prediction forms a natural next step in this line of inquiry, and efforts toward this goal are ongoing at the time of writing.

Example results, cf. **Figure 6**, suggest that the estimates of refractory period and conduction delay are sufficiently robust to detect changes in response to treatment with rate control drugs. However, this needs to be verified in a larger study population. By using the model to simulate the treatment effect of different drugs in a patient-specific setting, it might be possible to predict the outcome of the drug treatment and thus assist in treatment selection. Furthermore, it could also be useful in drug development, by aiding in understanding what AV node properties are affected by a novel compound, and in what way.

5. CONCLUSION

We have described and motivated a network model of the AV node, bundle of His, and Purkinje network. The model is demonstrated to be able to represent RR interval series extracted from ECG data well, both in the forms of histograms, Poincaré plots, and autocorrelation. This was made possible using the presented problem specific fitness function and optimization algorithm, taking advantage of the model's ability to increase running speed at the cost of precision. The robustness in parameter estimation enabled fitting of delay specific parameters from the AV node solely based on the ECG. It also made it possible to detect changes to the model parameters originating from the use of a rate control drug.

In summary, the combination of model and parameter estimation workflow presented here constitutes a significant improvement on previous AV node modeling efforts, suggesting the possibility to use ECG measurements to analyze drug effect on the AV node on a patient specific level.

DATA AVAILABILITY STATEMENT

The simulated data supporting the conclusions for this article will be available from the authors upon request. The measured data are owned by Vestre Viken Hospital Trust, and requests for access can be made to Sara R. Ulimoen. The code for the model together with an user example can be found at https://github.com/FraunhoferChalmersCentre/AV-node-model.

ETHICS STATEMENT

The studies involving human participants were reviewed and approved by the Norwegian Medicines Agency. The patients/participants provided their written informed consent to participate in this study.

AUTHOR CONTRIBUTIONS

MK, FS, and MW contributed to conception and design of the study. SU gathered and organized all raw data. FS computed and organized all RR interval series and λ. MK designed the changes to the model as well as the genetic algorithm with advice, suggestions, and supervision from FS and MW, and wrote the manuscript. FS and MW supervised the project and revised the manuscript during all the writing process. All authors contributed to manuscript revision, read, and approved the submitted version.

FUNDING

This work was supported by the Swedish Foundation for Strategic Research (Grant FID18-0023), the Swedish Research Council (Grant VR2019-04272), and the Crafoord Foundation (Grant 20200605).

SUPPLEMENTARY MATERIAL

The Supplementary Material for this article can be found online at: https://www.frontiersin.org/articles/10.3389/fphys.2021.728955/full#supplementary-material

REFERENCES

Benjamin, E. J., Muntner, P., Alonso, A., Bittencourt, M. S., Callaway, C. W., Carson, A. P., et al. (2019). Heart disease and stroke statistics-2019 update a report from the american heart association. *Circulation* 139, e56–e528. doi: 10.1161/CIR.0000000000000659

Climent, A. M., Guillem, M. S., Zhang, Y., Millet, J., and Mazgalev, T. (2011). Functional mathematical model of dual pathway AV nodal conduction. *Am. J. Physiol. Heart Circ. Physiol.* 300, H1393–H1401. doi: 10.1152/ajpheart.01175.2010

Corino, V. D., Sandberg, F., Lombardi, F., Mainardi, L. T., and Sörnmo, L. (2013). Atrioventricular nodal function during atrial fibrillation: model building and robust estimation. *Biomed. Signal Process. Control* 8, 1017–1025. doi: 10.1016/j.bspc.2012.10.006

Corino, V. D., Sandberg, F., Mainardi, L. T., and Sornmo, L. (2011). An atrioventricular node model for analysis of the ventricular response during atrial fibrillation. *IEEE Trans. Biomed. Eng.* 58, 3386–3395. doi: 10.1109/TBME.2011.2166262

Denes, P., Wu, D., Dhingra, R., Pietras, R. J., and Rosen, K. M. (1974). The effects of cycle length on cardiac refractory periods in man. *Circulation* 49, 32–41. doi: 10.1161/01.CIR.49.1.32

Deshmukh, P., Casavant, D. A., Romanyshyn, M., and Anderson, K. (2000). Permanent, direct his-bundle pacing: a novel approach to cardiac pacing in patients with normal his-Purkinje activation. *Circulation* 101, 869–877. doi: 10.1161/01.CIR.101.8.869

Henriksson, M., Corino, V. D., Sörnmo, L., and Sandberg, F. (2015). A statistical atrioventricular node model accounting for pathway switching during atrial fibrillation. *IEEE Trans. Biomed. Eng.* 63, 1842–1849. doi: 10.1109/TBME.2015.2503562

Hindricks, G., Potpara, T., Dagres, N., Arbelo, E., Bax, J. J., Blomström-Lundqvist, C., et al. (2020). 2020 ESC guidelines for the diagnosis and management of atrial fibrillation developed in collaboration with the European Association of Cardio-Thoracic Surgery (EACTS) the Task Force for the Diagnosis and Management of Atrial Fibrillation of the European Society of Cardiology (ESC) developed with the special contribution of the European Heart Rhythm Association (EHRA) of the ESC. *Eur. Heart J.* 42, 373–498. doi: 10.1093/eurheartj/ehaa612

Inada, S., Hancox, J., Zhang, H., and Boyett, M. (2009). One-dimensional mathematical model of the atrioventricular node including atrio-nodal, nodal, and nodal-his cells. *Biophys. J.* 97, 2117–2127. doi: 10.1016/j.bpj.2009.06.056

Jørgensen, P., Schäfer, C., Guerra, P. G., Talajic, M., Nattel, S., and Glass, L. (2002). A mathematical model of human atrioventricular nodal function incorporating concealed conduction. *Bull. Math. Biol.* 64, 1083–1099. doi: 10.1006/bulm.2002.0313

Kurian, T., Ambrosi, C., Hucker, W., Fedorov, V. V., and Efimov, I. R. (2010). Anatomy and electrophysiology of the human AV node. *Pacing Clin. Electrophysiol.* 33, 754–762. doi: 10.1111/j.1540-8159.2010.02699.x

Lagerholm, M., Peterson, C., Braccini, G., Edenbrandt, L., and Sornmo, L. (2000). Clustering ECG complexes using hermite functions and self-organizing maps. *IEEE Trans. Biomed. Eng.* 47, 838–848. doi: 10.1109/10.846677

Lian, J., Mussig, D., and Lang, V. (2006). Computer modeling of ventricular rhythm during atrial fibrillation and ventricular pacing. *IEEE Trans. Biomed. Eng.* 53, 1512–1520. doi: 10.1109/TBME.2006.876627

Mangin, L., Vinet, A., Pagé, P., and Glass, L. (2005). Effects of antiarrhythmic drug therapy on atrioventricular nodal function during atrial fibrillation in humans. *Europace* 7, S71–S82. doi: 10.1016/j.eupc.2005.03.016

Natale, A., Klein, G., Yee, R., and Thakur, R. (1994). Shortening of fast pathway refractoriness after slow pathway ablation. effects of autonomic blockade. *Circulation* 89, 1103–1108. doi: 10.1161/01.CIR.89.3.1103

Rashidi, A., and Khodarahmi, I. (2005). Nonlinear modeling of the atrioventricular node physiology in atrial fibrillation. *J. Theoret. Biol.* 232, 545–549. doi: 10.1016/j.jtbi.2004.08.033

Sandberg, F., Corino, V. D., Mainardi, L. T., Ulimoen, S. R., Enger, S., Tveit, A., et al. (2015). Non-invasive assessment of the effect of beta blockers and calcium channel blockers on the AV node during permanent atrial fibrillation. *J. Electrocardiol.* 48, 861–866. doi: 10.1016/j.jelectrocard.2015.07.019

Sandberg, F., Stridh, M., and Sornmo, L. (2008). Frequency tracking of atrial fibrillation using hidden Markov models. *IEEE Trans. Biomed. Eng.* 55, 502–511. doi: 10.1109/TBME.2007.905488

Shrier, A., Dubarsky, H., Rosengarten, M., Guevara, M., Nattel, S., and Glass, L. (1987). Prediction of complex atrioventricular conduction rhythms in humans with use of the atrioventricular nodal recovery curve. *Circulation* 76, 1196–1205. doi: 10.1161/01.CIR.76.6.1196

Stridh, M., and Sornmo, L. (2001). Spatiotemporal QRST cancellation techniques for analysis of atrial fibrillation. *IEEE Trans. Biomed. Eng.* 48, 105–111. doi: 10.1109/10.900266

Ulimoen, S. R., Enger, S., Carlson, J., Platonov, P. G., Pripp, A. H., Abdelnoor, M., et al. (2013). Comparison of four single-drug regimens on ventricular rate and arrhythmia-related symptoms in patients with permanent atrial fibrillation. *Am. J. Cardiol.* 111, 225–230. doi: 10.1016/j.amjcard.2012.09.020

Wahde, M. (2008). *Biologically Inspired Optimization Methods: An Introduction*. Gothenburg: WIT Press.

Wallman, M., and Sandberg, F. (2018). Characterisation of human AV-nodal properties using a network model. *Med. Biol. Eng. Comput.* 56, 247–259. doi: 10.1007/s11517-017-1684-0

Conflict of Interest: The authors declare that the research was conducted in the absence of any commercial or financial relationships that could be construed as a potential conflict of interest.

Publisher's Note: All claims expressed in this article are solely those of the authors and do not necessarily represent those of their affiliated organizations, or those of the publisher, the editors and the reviewers. Any product that may be evaluated in this article, or claim that may be made by its manufacturer, is not guaranteed or endorsed by the publisher.

Paper II

frontiers | Frontiers in Physiology

TYPE Original Research
PUBLISHED 04 October 2022
DOI 10.3389/fphys.2022.976526

OPEN ACCESS

EDITED BY
Axel Loewe,
Karlsruhe Institute of Technology,
Germany

REVIEWED BY
Haibo Ni,
University of California, Davis,
United States
Michela Masè,
Institute of Mountain Emergency
Medicine, Eurac Research, Italy

*CORRESPONDENCE
Frida Sandberg,
frida.sandberg@bme.lth.se

SPECIALTY SECTION
This article was submitted to Cardiac
Electrophysiology,
a section of the journal
Frontiers in Physiology

RECEIVED 23 June 2022
ACCEPTED 05 September 2022
PUBLISHED 04 October 2022

CITATION
Karlsson M, Wallman M, Platonov PG,
Ulimoen SR and Sandberg F (2022), ECG
based assessment of circadian variation
in AV-nodal conduction during
AF—Influence of rate control drugs.
Front. Physiol. 13:976526.
doi: 10.3389/fphys.2022.976526

ECG based assessment of circadian variation in AV-nodal conduction during AF—Influence of rate control drugs

Mattias Karlsson[1,2], Mikael Wallman[1], Pyotr G. Platonov[3], Sara R. Ulimoen[4] and Frida Sandberg[2]*

[1]Department of Systems and Data Analysis, Fraunhofer-Chalmers Centre, Gothenburg, Sweden, [2]Department of Biomedical Engineering, Lund University, Lund, Sweden, [3]Department of Cardiology, Clinical Sciences, Lund University, Lund, Sweden, [4]Vestre Viken Hospital Trust, Department of Medical Research, Bærum Hospital, Drammen, Norway

The heart rate during atrial fibrillation (AF) is highly dependent on the conduction properties of the atrioventricular (AV) node. These properties can be affected using β-blockers or calcium channel blockers, mainly chosen empirically. Characterization of individual AV-nodal conduction could assist in personalized treatment selection during AF. Individual AV nodal refractory periods and conduction delays were characterized based on 24-hour ambulatory ECGs from 60 patients with permanent AF. This was done by estimating model parameters from a previously created mathematical network model of the AV node using a problem-specific genetic algorithm. Based on the estimated model parameters, the circadian variation and its drug-dependent difference between treatment with two β-blockers and two calcium channel blockers were quantified on a population level by means of cosinor analysis using a linear mixed-effect approach. The mixed-effects analysis indicated increased refractoriness relative to baseline for all drugs. An additional decrease in circadian variation for parameters representing conduction delay was observed for the β-blockers. This indicates that the two drug types have quantifiable differences in their effects on AV-nodal conduction properties. These differences could be important in treatment outcome, and thus quantifying them could assist in treatment selection.

KEYWORDS

atrial fibrillation, atrioventricular node, circadian variation, mathematical modeling, genetic algorithm, mixed effect modeling, ECG, rate control drugs

1 Introduction

Atrial fibrillation (AF) is the most common arrhythmia in the world, with a prevalence of 2–4% in the adult population Benjamin et al. (2019), reaching 7% for those aged 65 and above Di Carlo et al. (2019). It is characterized by rapid and irregular contraction of the atria, originating from highly disorganized electrical activity, and associated with an increased risk of mortality, mainly due to stroke or heart failure Hindricks et al. (2021).

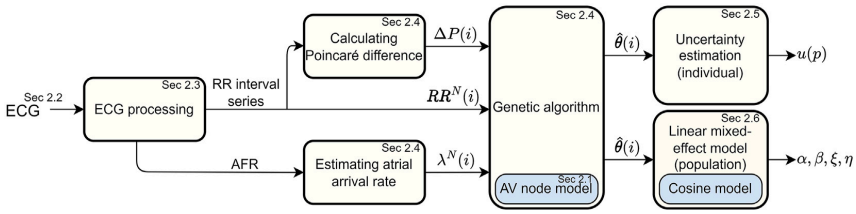

FIGURE 1
A flowchart of the overall framework for estimating AV node conduction properties on an individual and a population level.

The electrical impulses in the atria are conducted via the atrioventricular (AV) node to reach and activate the ventricles. The AV node can block and delay incoming impulses based on its refractory period and conduction delay properties. During AF - when the AV node is bombarded with impulses from the atria - blocking of impulses prevents the heart from racing, but may not be sufficient to maintain a normal heart rate and will still result in significant beat-to-beat variability in the ventricular activation Corino et al. (2015b); Mase et al. (2017).

To remedy this, rate control drugs can be used in order to modify the conduction properties of the AV node. There are two main types of rate control drugs used for AF treatment; β-blockers and calcium channel blockers Hindricks et al. (2021). As the name suggests, β-blockers block the β-receptors in AV node cells, decreasing the effect of the sympathetic nervous system, whereas calcium channel blockers prevent the L-type calcium channels from opening, thereby reducing the conduction in the AV node cells. Both types of drugs have been shown effective in reducing the heart rate during AF Ulimoen et al. (2013). However, the optimal treatment for a given patient is often chosen empirically. Since the two drug types have different physiological effects on the AV node conduction properties, assessing the drug-induced changes in these AV node properties could provide an important step toward personalized treatment. One of the main differences between the two drug types is the effect on the sympathetic nervous system, which can be quantified by the circadian variation in the AV node conduction properties. Furthermore, previous studies have shown a significant difference in the predominant RR interval between day and night, without a difference in dominant atrial cycle length, suggesting circadian variation in the AV node conduction properties Climent et al. (2010).

Conduction properties of the AV node have previously been characterized using mathematical models based on measurements of the electrical activity in the heart Shrier et al. (1987); Billette and Nattel (1994); Sun et al. (1995). Several models of the AV node during AF have been proposed; both based on invasive data from rabbits Inada et al. (2009); Climent et al. (2011) and humans Jørgensen et al. (2002); Mangin et al. (2005); Masè et al. (2012, 2015), and on non-invasive data from humans Corino et al. (2011, 2013); Henriksson et al. (2015). We have previously presented a network model of the AV node capable of assessing the refractory period and the conduction delay of the AV node from 20-min ECG segments Karlsson et al. (2021). However, continuous assessment of AV conduction delay and refractoriness from 24-hour ECG recordings has not previously been performed; such assessment enables analysis of long-term variations in AV conduction properties.

The aim of the present study is to develop a framework for long-term ECG-based assessment of conduction properties in the AV node, and to utilize this framework for analysis of circadian variation and its drug-induced changes in a cohort of 60 patients with persistent AF Ulimoen et al. (2013). To accomplish this, we propose a problem-specific optimization algorithm able to continuously estimate the model parameters from the previously presented network model Karlsson et al. (2021). Furthermore, the uncertainty of the parameter estimates is assessed using a variant of Sobol's method Sobol (2001), and the drug-induced differences in circadian variation between β-blockers and calcium channel blockers on a population level are quantified using a linear mixed-effect model.

2 Materials and methods

A schematic overview of the methodology is given in Figure 1. The ECG data (Section 2.2) is first processed in order to extract a RR interval series and an atrial fibrillatory rate (AFR) trend, as described in Section 2.3. The RR interval series is then divided into segments of length N, and the AFR trend is used to estimate the atrial arrival rate in the corresponding time interval. The AV node model (Section 2.1) is fitted to the ECG-derived data using a tailored optimization algorithm, as described in Section 2.4, in order to obtain model parameter estimates. Furthermore, the Poincaré plot difference, which quantifies the rate of change of RR series characteristics, is used to tune hyper-parameters in the optimization algorithm during parameter estimation. The uncertainty of the estimated model

parameters is investigated using a variant of Sobol's method, as described in Section 2.5. Finally, cosinor analysis is used to quantify circadian variation in the model parameter trends, and a linear mixed effects modeling approach is used to investigate drug-dependent differences on a population level, as described in Section 2.6.

2.1 AV node model

A network model of the human AV node, shown in Figure 2, is used to characterize the conduction delay and refractory period. A brief description of the model is given here, for more details, see Karlsson et al. (2021). The model describes the AV node as an interconnected network of nodes, each capable of transmitting incoming impulses. The model consists of 21 nodes; divided into a fast pathway (FP) with ten nodes, a slow pathway (SP) with ten nodes, and a coupling node. The nodes can react to an incoming impulse either by blocking - if the node is in its refractory state - or by conducting it to all adjacent nodes after adding a conduction delay, after which the node returns to its refractory state. The refractory period ($R_j(n)$) and the conduction delay ($D_j(n)$) of node j following an impulse n are given by,

$$R_j(n) = R_{min} + \Delta R\left(1 - e^{\frac{-\tilde{t}_j(n)}{\tau_R}}\right) \quad (1)$$

$$D_j(n) = D_{min} + \Delta D e^{\frac{-\tilde{t}_j(n)}{\tau_D}}, \quad (2)$$

where $\tilde{t}_j(n)$ is the diastolic interval preceding impulse n,

$$\tilde{t}_j(n) = t_j(n) - t_j(n-1) - R_j(n-1), \quad (3)$$

and $t_j(n)$ is the arrival time of impulse n at node j. When $\tilde{t}_j(n)$ is negative, the impulse will be blocked since the node is in its refractory state. The parameters $R_{\min}$, ΔR, τ_R, $D_{\min}$, ΔD, and τ_D are fixed for all nodes in the SP and the FP, respectively. This results in the 12 model parameters

TABLE 1 The interpretation of the model parameters. Superscripts indicating the pathway (SP, FP) are omitted to avoid redundancy.

Parameter	Parameter description
$R_{\min}$	Minimum refractory period, attained for short diastolic intervals
ΔR	Maximum prolongation of the refractory period, attained for long diastolic intervals.
τ_R	Time constant for the refractory period, determining the impact of the diastolic interval
$D_{\min}$	Minimum conduction delay, attained for short diastolic intervals
ΔD	Maximum prolongation of the conduction delay, attained for long diastolic intervals.
τ_D	Time constant for the conduction delay, determining the impact of the diastolic interval

$\boldsymbol{\theta} = [R_{\min}^{FP}, \Delta R^{FP}, \tau_R^{FP}, R_{\min}^{SP}, \Delta R^{SP}, \tau_R^{SP}, D_{\min}^{FP}, \Delta D^{FP}, \tau_D^{FP}, D_{\min}^{SP}, \Delta D^{SP}, \tau_D^{SP}]$. For convenience, the interpretation of the model parameters are given in Table 1. For the coupling node, the delay is fixed to 60 ms, and the refractory period is fixed to the mean of the ten shortest RR intervals in the data used for model parameter estimation, $RR_{\min}$.

The input to the model - representing impulses arriving from the atria - is created using a Poisson process with mean arrival rate λ. The output of the model represents the time points for ventricular activation, and thus the differences between adjacent elements in the output vector represent the RR intervals.

2.2 ECG data

The RATe control in Atrial Fibrillation (RATAF) study Ulimoen et al. (2013) acquired 24-hour ambulatory ECGs during baseline and under the influence of four rate control drugs; the two calcium channel blockers verapamil and diltiazem, and the two β-blockers metoprolol and carvedilol. The study population consists of 60 patients with permanent AF, no heart failure, or symptomatic ischemic heart disease. The study was approved by the regional ethics

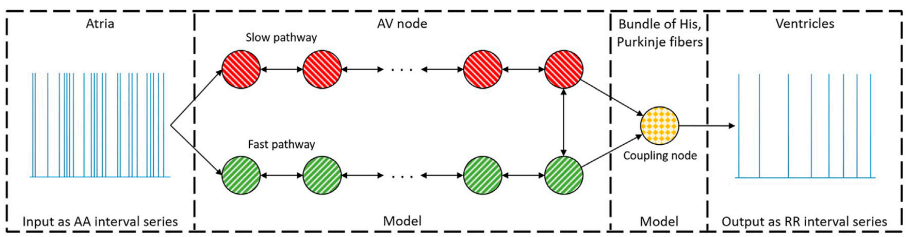

FIGURE 2
A schematic representation of the network model where the yellow node represents the coupling node, the red nodes the SP, the green nodes the FP, and arrows the direction for impulse conduction. For readability, only a subset of the 21 nodes is shown.

committee and the Norwegian Medicines Agency and conducted in accordance with the Helsinki Declaration. The trend in the AV node refractory period and conduction delay from these five 24-hour ECG recordings per patient is assessed by estimations of the trends in $\boldsymbol{\theta}$.

2.3 ECG processing

The RR interval series is extracted from the ECG, where RR intervals following and preceding QRS-complexes with deviating morphology are excluded from the series Lagerholm et al. (2000). Due to excessive noise in the ECGs, some RR intervals are missed, leading to an unrealistically low heart rate. Thus, the data are divided into minute-long non-overlapping segments, and all segments with a heart rate lower than 20 bpm are removed, occasionally resulting in gaps in the signals. The signals with a total duration shorter than 12 h or with less than 20 h between start and end are excluded from further analysis. After excluding data according to these criteria, data from 59 patients remained for inclusion in this study. The number of patients with data considered to be of sufficient duration for analysis and the average duration of these recordings for the different treatments are shown in Table 2.

The f-waves in the ECG are extracted using spatiotemporal QRST cancellation Stridh and Sornmo (2001). The AFR trends are then estimated by tracking the fundamental frequency of the extracted f-wave signal using a hidden Markov model-based approach Sandberg et al. (2008); resulting in a resolution for the AFR trends of one minute.

2.4 Parameter estimation

The atrial arrival rate, λ, is estimated by correcting the AFR trend, taking the atrial depolarization time into account Corino et al. (2013). Outliers in the estimated λ trends are excluded based on visual inspection guided by cluster analysis. The resulting trends are low-pass filtered using a sliding triangular window filter with a width equal to 70.

The model parameters $\boldsymbol{\theta}$ are assumed to vary over time, making this a dynamic optimization problem. Thus, the data are first divided into overlapping data segments of $N = 1000$ RR intervals; where N is chosen to give a good balance between resolution and robustness of the estimates. Each data segment contains one segment-specific mean arrival rate $\lambda^N(i)$ calculated as the mean of the λ trend in the segment starting at RR interval i, as well as one RR interval series, $\boldsymbol{RR}^N(i)$. The estimated parameters of a data segment starting at RR interval i is denoted by $\hat{\boldsymbol{\theta}}(i)$.

A fitness function based on the Poincaré plot - a scatter plot of successive pairs of RR intervals - is used to quantify the difference between observed and simulated RR series. The Poincaré plots are binned into two-dimensional bins with a width of 50 m, centered between 250 and 1800 m, forming a two-dimensional histogram. The error function (ϵ), i.e., the inverse fitness function, is then calculated from the number of samples in the bins according to Eq. 4,

$$\epsilon = \frac{1}{K}\sum_{k=1}^{K}\frac{\left(x_k^N - \frac{N}{N_{sim}}\tilde{x}_k^{N_{sim}}\right)^2}{\sqrt{\frac{N}{N_{sim}}\tilde{x}_k^{N_{sim}}}}, \tag{4}$$

where K is the number of bins, N_{sim} is the number of RR intervals simulated with the model, and x_k^N and $\tilde{x}_k^{N_{sim}}$ are the numbers of RR intervals in the k-th bin of the observed data and model output, respectively.

A genetic algorithm (GA) is used to search for the values of $\boldsymbol{\theta}$ yielding the minimum ϵ. A GA consists of a population of individuals that evolves based on their fitness value towards a solution using selection, crossover, and mutation Wahde (2008).

By assuming that a large change in the Poincaré plot relates to a large change in parameter values, it is possible before starting the optimization to decide when the optimization algorithm should focus on exploration or exploitation. As a heuristic for this, we introduce the difference in the Poincaré plots ($\Delta P(i)$), according to Eq. 5,

TABLE 2 The number of recordings and recording length (mean ± std) analyzed in this study following exclusion of recordings with insufficient signal quality, as described in Section 2.3.

Drug	Number of recordings	Recordings length (h)
Baseline	51	20.88 ± 2.85
Verapamil	53	21.92 ± 2.39
Diltiazem	56	21.71 ± 2.44
Metoprolol	53	21.87 ± 1.98
Carvedilol	57	21.23 ± 2.65
Total	270	21.52 ± 2.59

$$\Delta P(i) = \frac{1}{K}\sum_{k=1}^{K}\left(x_k^{N_{\Delta P}}(i) - x_k^{N_{\Delta P}}(i+1000)\right)^2, \quad (5)$$

where $x_k^{N_{\Delta P}}(i)$ and $x_k^{N_{\Delta P}}(i+1000)$ are the number of RR intervals in the k-th bin of the Poincaré plot for the RR interval series starting at interval i and $i + 1000$, respectively. Moreover, the segment length $N_{\Delta P}$ is set to 2000. The Poincaré plot difference, $\Delta P(i)$, is used to tune hyper-parameters in the optimization algorithm.

The GA used for estimating $\hat{\boldsymbol{\theta}}(i)$ has a population size of 400 individuals - where each individual is a vector of values for $\boldsymbol{\theta}$ - and uses tournament selection, a two-point crossover, and creep mutation Wahde (2008). The number of generations the GA runs before switching to the next data segment varies from 1 when $\Delta P(i) < 800$; to 2 when $800 \leq \Delta P(i) < 2000$; to 3 when $\Delta P(i) \geq 2000$. The step size for the sliding windows is determined by the trade-off between the resolution and the computing cost, and is set to 108 s; resulting in 800 steps for full 24-hour measurements. Thus, there will be 800 estimated $\hat{\boldsymbol{\theta}}(i)$ for a 24-hour measurement. As noted previously, there are also gaps in the data. Thus, the step size will partly vary to match the start and end of the RR segments, to ensure that all data are used. For reference, estimating the $\hat{\boldsymbol{\theta}}(i)$ trend from a 24-hour RR and λ series using a single core on a standard desktop computer (Intel® Core™ i7-6600U Processor, @ 2.60 GHz) requires on average 4 hours.

Since the Poisson process used to create the model input is stochastic, ϵ varies between realizations. This variation is dependent on the number of RR intervals generated from the model, where more RR intervals reduce the variation but require more computing power. To have a good balance between computing power and stability, N_{sim} is set to 1500. However, the ten fittest individuals in each generation are re-evaluated, with $N_{sim} = 5000$, before the individual with the best fit for each data segment, $\hat{\boldsymbol{\theta}}(i)$, is saved.

The individuals for the first generation are randomly initialized using a latin hypercube sampling in the ranges: $\{R_{\min}^{SP}, R_{\min}^{FP}\} \in [150, 650]\ ms$; $\{\Delta R^{SP},\ \Delta R^{FP}\} \in [0,\ 700]\ ms$; $\{\tau_R^{SP}, \tau_R^{FP}\} \in [40, 300]\ ms$; $\{D_{\min}^{SP}, D_{\min}^{FP}\} \in [0, 30]\ ms$; $\{\Delta D^{SP},\ \Delta D^{FP}\} \in [0,\ 75]\ ms$; $\{\tau_D^{SP}, \tau_D^{FP}\} \in [40, 300]\ ms$. These values are also used as boundaries for the model parameters. Hence, the difference between the upper bound and the lower bound for the parameters is the range that the parameters can vary within, here denoted $r(p)$ and in vector form $\boldsymbol{r}$, where p is the parameter index ordered as in $\boldsymbol{\theta}$.

To reduce the risk of premature convergence and to maintain a good diversity in the population, immigrants - individuals not created from the current population - are used. These immigrants are created using three different methods; 1) by saving and then re-using the ten most fit individuals and their model output per generation; 2) by running eight computationally faster GA, using only 16 individuals and $N_{sim} = 750$, simultaneously; and 3), by random sampling. The number of immigrants is dependent on $\Delta P(i)$ and is created in equal proportion using the three different creation methods. These new individuals are then introduced into the population at the start of every new data segment by replacing the individuals with the lowest fitness. More specific details about the GA are found in Supplementary Material, Section 1.

2.5 Parameter uncertainty estimation

A variant of Sobol's method Sobol (2001) is used to derive the uncertainty for each estimated parameter set $\hat{\boldsymbol{\theta}}(i)$. The contribution to the output variance ($v(p)$) for a parameter p, including the variation caused by its interaction with all the other parameters, is estimated by the following procedure. Firstly, two 30 x 12 matrices ($\boldsymbol{A}$ and $\boldsymbol{B}$), where 30 is the number of sampled parameter vectors, are generated by samples from a quasi Monte Carlo procedure based on the Latin hypercube design. Unlike Sobol's method - which samples in the whole parameter range - these samples are generated within $\hat{\boldsymbol{\theta}}(i) \pm 0.075\boldsymbol{r}$, hence within a hyper-rectangle covering 15% of the total range of each parameter. Secondly, 12 new matrices, $\boldsymbol{AB}_p$ are created by replacing the p-th column in $\boldsymbol{A}$ with the p-th from $\boldsymbol{B}$. Thirdly, ϵ is calculated for each parameter set in the matrices by running the model, before the expected value of the contribution to the output variance is estimated according to Eq. 6 Sobol (2001).

$$\hat{v}(p) = \frac{1}{2\cdot 30}\sum_{q=1}^{30}\left(\epsilon_{A_q} - \epsilon_{AB_{pq}}\right)^2. \quad (6)$$

Here ϵ_{A_q} and $\epsilon_{AB_{pq}}$ quantifies the difference between the observed RR series and the model output as given in Eq. 4, for the parameter sets in $\boldsymbol{A}$ and $\boldsymbol{AB}_p$, respectively.

The estimated $\hat{v}(p)$ are then, together with the mean ($\bar{\epsilon}$) and standard deviation (σ_ϵ) of the 30 realizations of $\hat{\boldsymbol{\theta}}(i)$, used to calculate a parameter uncertainty estimate according to Eq. 7.

$$u(p) = \frac{0.15r(p)}{\sqrt{\hat{v}(p)} - \sigma_\epsilon}0.1\bar{\epsilon}. \quad (7)$$

Here $0.15r(p)$ originates from the distance between $\hat{\boldsymbol{\theta}}(i)$ and the border of the sampled hyper-space, and $\sqrt{\hat{v}(p)} - \sigma_\epsilon$ from the difference between the error variation inside the hyper-space and at $\hat{\boldsymbol{\theta}}(i)$. Hence, the fraction relates to the slope-intercept between the parameter distance and the uncertainty. The remaining product relates this slope to 10% of the mean error for $\hat{\boldsymbol{\theta}}(i)$. Thus, the interpretation of $u(p)$ is: 'Assuming interaction between all model parameters, how large a step can be taken for parameter p before the contribution to ϵ for $\hat{\boldsymbol{\theta}}(i)$ is increased by 10%'. This was then repeated for all $\hat{\boldsymbol{\theta}}(i)$ for all patients and drugs.

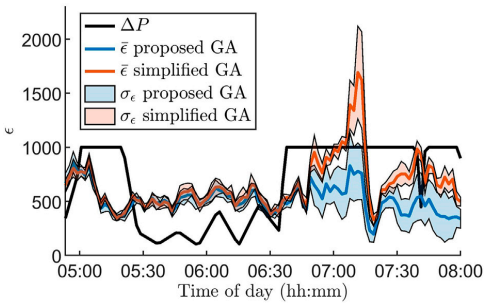

FIGURE 3
Mean (colored lines) and standard deviation (colored areas) of the error ϵ for 100 segments for the proposed genetic algorithm (blue) and a standard genetic algorithm (red) together with the Poincare difference $\Delta P(i)$ (black line), defined in Eq. 5, for data from one patient at baseline during 3 hours. The standard deviation and mean are based on ten runs of the algorithms. Note that $\Delta P(i)$ is scaled with $\frac{1}{5}$ for readability.

2.6 Circadian variation

The drug-dependent circadian variation for the estimated AV node parameters is quantified using linear mixed-effect modeling, i.e., using a statistical model comprising both fixed effects and random effects. The model used consists of a 24-hour periodic cosine with mean $\boldsymbol{m}$, amplitude $\boldsymbol{a}$, and phase $\boldsymbol{\phi}$, as seen in Eqs. 8, 9, and 10.

$$\boldsymbol{y}_{pat,m}(t) = \boldsymbol{m}_{pat,m} + \boldsymbol{a}_{pat,m} \cos\left(\frac{2\pi}{24}t + \boldsymbol{\phi}\right) \tag{8}$$

$$\boldsymbol{m}_{pat,m} = \boldsymbol{\alpha} + \boldsymbol{\alpha}_m + \boldsymbol{\eta}_{pat} + \boldsymbol{\eta}_{pat,m} \tag{9}$$

$$\boldsymbol{a}_{pat,m} = \boldsymbol{\beta} + \boldsymbol{\beta}_m + \boldsymbol{\xi}_{pat} + \boldsymbol{\xi}_{pat,m} \tag{10}$$

Here $\boldsymbol{y}_{pat,m}(t)$ represents the estimated parameter trends of patient *pat* during treatment $m \in$ {Baseline, Verapamil, Diltiazem, Metoprolol, Carvedilol}. Moreover, t corresponds to the time of the day, in hours, of the RR interval i that the estimated $\hat{\boldsymbol{\theta}}(i)$ relates to. Furthermore, $\boldsymbol{\alpha}$, $\boldsymbol{\alpha}_m$, $\boldsymbol{\beta}$, and $\boldsymbol{\beta}_m$ represent the fixed-effects; with $\boldsymbol{\alpha}$ and $\boldsymbol{\beta}$ corresponding to the mean value for the mean and amplitude during baseline, and $\boldsymbol{\alpha}_m$ and $\boldsymbol{\beta}_m$ to the average deviation from the baseline values, caused by the drugs. The random effects $\boldsymbol{\eta}_{pat}$, $\boldsymbol{\eta}_{pat,m}$, $\boldsymbol{\xi}_{pat}$, and $\boldsymbol{\xi}_{pat,m}$ correspond to the individual deviation from the fixed-effects, and are assumed to be sampled from a zero-mean gaussian distribution. During baseline, $\boldsymbol{\alpha}_m$, $\boldsymbol{\beta}_m$ and $\boldsymbol{\eta}_{pat,m}$, $\boldsymbol{\xi}_{pat,m}$ are assumed to be zero. For a given individual, $\boldsymbol{\phi}$ is assumed to be equal for all 12 model parameters and is estimated by means of principal component analysis of the $\hat{\boldsymbol{\theta}}(i)$ trends. The 12 vectors created by projecting the data onto the 12 principal components are fitted to a cosine with mean m_c, amplitude a_c, and phase ϕ_c, where c indicates the c-th principal component, using the simplex search method Lagarias et al. (1998). The phase, ϕ, is set equal to the ϕ_c associated with the highest a_c. Moreover, for cases where $\boldsymbol{a}_{pat,m}$ is negative, a phase-shift of π is added to ensure that all the amplitudes are positive.

With $\boldsymbol{\phi}$ estimated, $\boldsymbol{\alpha}$, $\boldsymbol{\alpha}_m$, $\boldsymbol{\beta}$, $\boldsymbol{\beta}_m$, $\boldsymbol{\eta}_{pat}$, $\boldsymbol{\eta}_{pat,m}$, $\boldsymbol{\xi}_{pat}$, and $\boldsymbol{\xi}_{pat,m}$ are fitted using the linear mixed-effects model function 'fitlme ()' in MATLAB (The MathWorks Inc. Version R2019b); using the full covariance matrix with the Cholesky parameterization and the maximum likelihood for estimating parameters of the linear mixed-effects model with trust region based quasi-Newton optimizer as settings.

An assessment of the goodness of fit for the linear mixed-effect model is calculated as the RMSE between the modeled cosine and the estimated parameters. For easier comparison between parameters, the RMSE for each parameter is weighted by their respective range, $r(p)$.

2.7 Statistic analysis

The estimated parameters $\hat{\boldsymbol{\theta}}(i)$, as well as AFR and HR, were averaged for each recording, and significant difference between the averages at baseline and under the four drugs were assessed one-by-one using the paired two-sided Wilcoxon signed rank test Woolson (2007) with the Benjamini–Hochberg correction Benjamini and Hochberg (1995). Patients with missing recordings (cf. Table 2) at baseline or the drug in question were excluded from the analysis. A p-value below 0.05 after correction was considered significant.

3 Results

Figure 3 illustrates the advantages of using the GA proposed in Section 2.4 for parameter estimation by comparing it to a standard version of the GA. For the standard GA, all hyper-parameters, as well as the number of generations per data segment, are fixed and thus do not take advantage of $\Delta P(i)$. To highlight the differences between the algorithms, we zoom in on a three hour long segment where the RR series characteristics change rapidly. It is clear that ϵ increases along with $\Delta P(i)$ for the standard GA, in contrast to the proposed GA.

From the GA we acquire one estimate per data segment, for all 59 patients and all drugs, resulting in a total of 175,640 $\hat{\boldsymbol{\theta}}(i)$. To give the reader a sense of the match between the model output and RR interval series obtained from the ECG, we present two examples of Poincaré plots and histograms together with the associated RR interval series. One corresponds to the median ϵ, and one where ϵ is higher than 95% of all ϵ, as shown in Figure 4. It is evident that the histograms and Poincaré plots from the model output and data are similar for both cases, indicating a good match to data in most data segments. However, there is a considerable difference on a beat-to-beat level, as indicated by the RR interval series. Moreover, $\hat{\boldsymbol{\theta}}(i)$ for one patient at baseline is shown in Figure 5, where clear changes over time can be seen.

TABLE 3 Recording averages of estimated model parameters, AFR, and HR at baseline and during treatment with the four different drugs (mean ± standard deviation). Differences from baseline are evaluated using the Wilcoxon signed rank test with the Benjamini–Hochberg correction; significant difference from baseline for the drugs, with false discovery rate at 0.05, is indicated with *.

Parameter	Baseline	Verapamil	Diltiazem	Metoprolol	Carvedilol
$R^{FP}_{\min}$ (ms)	435 ± 139	488 ± 134*	518 ± 118*	489 ± 126*	476 ± 123*
ΔR^{FP} (ms)	403 ± 195	478 ± 190*	488 ± 202*	495 ± 180*	483 ± 172*
τ^{FP}_{R} (ms)	175 ± 59	165 ± 63	163 ± 64	162 ± 58	167 ± 57
$R^{SP}_{\min}$ (ms)	241 ± 102	280 ± 125*	287 ± 124*	260 ± 114	269 ± 123
ΔR^{SP} (ms)	231 ± 176	274 ± 201	301 ± 215*	312 ± 187*	274 ± 186*
τ^{SP}_{R} (ms)	180 ± 60	183 ± 62	171 ± 63	176 ± 62	176 ± 63
$D^{FP}_{\min}$ (ms)	5.3 ± 4.5	5.4 ± 4.8	5.4 ± 4.7	5.9 ± 4.5	5.3 ± 4.5
ΔD^{FP} (ms)	18.9 ± 16.9	21.7 ± 17.2	22.1 ± 17.3	21.8 ± 16.7	21.4 ± 16.9
τ^{FP}_{D} (ms)	141 ± 54	144 ± 50	145 ± 53	149 ± 50	142 ± 53
$D^{SP}_{\min}$ (ms)	21.0 ± 5.3	21.6 ± 5.1	22.5 ± 5.2*	21.7 ± 4.8	21 ± 5.2
ΔD^{SP} (ms)	26.3 ± 21.4	23.8 ± 20.9	19.6 ± 20.7*	22.6 ± 21.2	21.5 ± 20.8
τ^{SP}_{D} (ms)	185 ± 68	184 ± 57	183 ± 65	186 ± 58	180 ± 65
HR (bpm)	95 ± 13	80 ± 12*	74 ± 10*	81 ± 10*	84 ± 11*
AFR (Hz)	4.96 ± 0.34	4.56 ± 0.45*	4.71 ± 0.44*	4.86 ± 0.40*	4.81 ± 0.51*

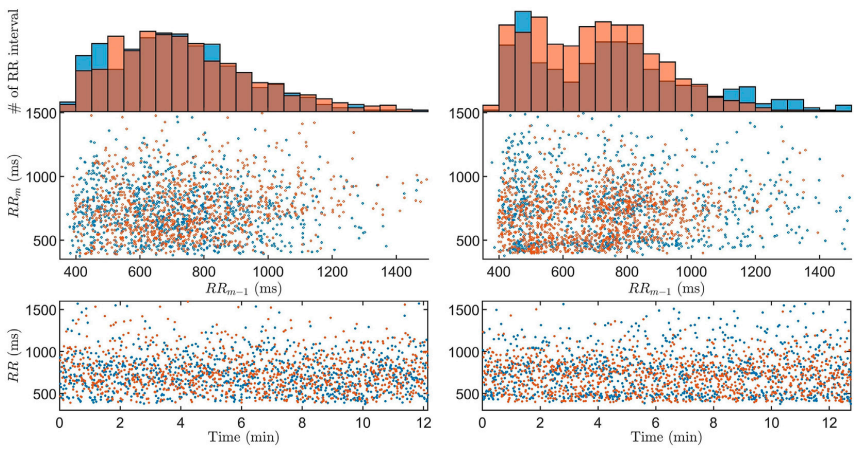

FIGURE 4
The Poincaré plot with associated histogram and RR interval series of data (blue) and model output (orange) for the $\hat{\theta}(i)$ corresponding to the median ϵ (left) and to the $\hat{\theta}(i)$ which ϵ is higher than 95% of all ϵ (right).

Recording averages of estimated model parameters, AFR, and HR at baseline and during treatment with the four different drugs are shown in Table 3. Significant differences, as described in Section 2.7, are indicated in the table by "*". This shows a significant increase in the refractory period in the FP for all drugs, as well as a significant decrease in heart rate and AFR for all drugs.

3.1 Uncertainty estimation

The average $u(p)$, as explained in Eq. 7, normalized with $r(p)$, are shown in Figure 6. From this, it is evident that the model parameters relating to the SP are more robustly estimated than their FP counterpart, and that the model parameters relating to the

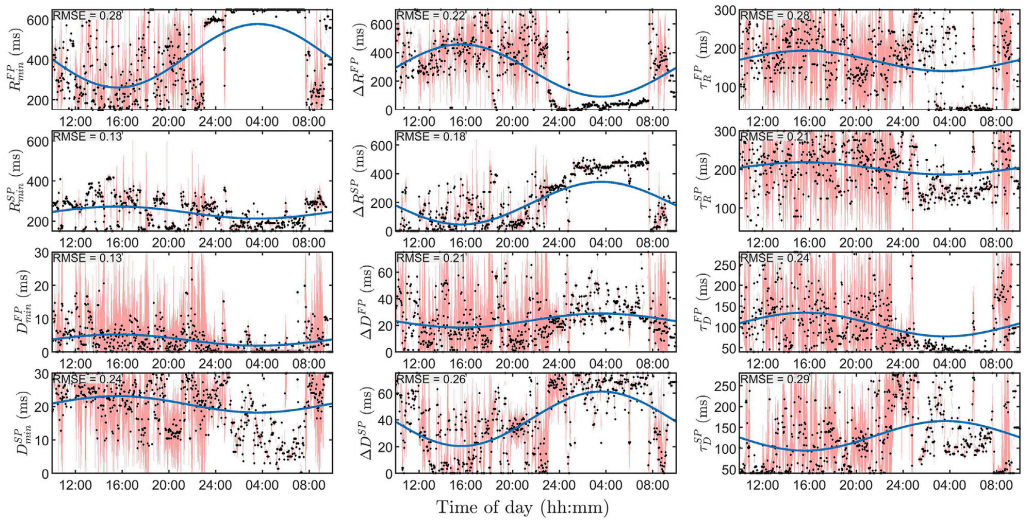

FIGURE 5
Estimated model parameters $\hat{\boldsymbol{\theta}}(i)$ (black dots), with corresponding uncertainty estimates *PU* (red areas), along with the fitted cosine (blue lines) used for the circadian variation, for one patient during baseline. In each panel, the RMSE is reported as a measure of goodness of fit between $\hat{\boldsymbol{\theta}}(i)$ and the fitted cosine. Left column shows the parameters relating to the minimum conduction delay or refractory period, the middle column the parameters relating to the maximum prolongation, and the right column to the time constants. For further explanation of the model parameters, see Table 1.

refractory period are more robustly estimated than their conduction delay counterpart. Most noteworthy is the lower uncertainty for R^{SP}_{min} and ΔR^{SP}, suggesting a higher impact on the output of the model.

The uncertainty estimates, $u(p)$, for one patient are shown as red background for each $\hat{\boldsymbol{\theta}}(i)$ in Figure 5, where again $u(p)$ for the refractory parameters in the SP is lower. There is also a clear difference in $u(p)$ between nighttime and daytime, where the uncertainty is much lower at night.

3.2 Circadian variation

In Figure 5 we also show an example of the circadian variation (blue lines) for the aforementioned patient, as explained in Eqs. 8, 9, and 10, where a clear distinction between night and day can be seen for most parameters. The average RMSE for the 12 model parameters seen in Figure 5 is 0.22, which can be compared with the average RMSE for all patients and treatment of 0.16 ± 0.03 (mean ± std).

The mean and standard deviation of the circadian variation phase ϕ was 1.03 ± 0.74 rad; corresponding to an extreme value at approximately 04:00 am ± 2.8 h.

The fixed-effects $\boldsymbol{\alpha}_m$ and $\boldsymbol{\beta}_m$ and their respective 95% confidence interval, normalized with $r(p)$, are shown in Figure 7, where the fixed-effects represent the average difference in effect with respect to baseline that the drugs have on the population. It is evident from $\boldsymbol{\alpha}_m$ in Figure 7 (top panel) that all rate control drugs on average increase the refractory period in both pathways; with a significant increase ($p < 0.05$) in R^{FP}_{min} and Δ^{FP} for all drugs, in R^{SP}_{min} for all but metoprolol, and in ΔR^{SP} for all but verapamil. Moreover, differences between the β-blockers and the calcium channel blockers can be observed. Most noticeably for the amplitude ($\boldsymbol{\beta}_m$) of ΔD^{FP} and ΔD^{SP}, where the two β-blockers have a distinctly negative effect in comparison with the two calcium channel blockers.

Detailed results for the estimated fixed and random effects can be found in the Supplementary Material, Section 2.

4 Discussion

In this study, we have presented a mathematical framework able to continuously estimate model parameters representing the conduction delay and refractory period of the AV node during 24 h for patients with permanent AF from ECG data. Trends in the estimated model parameters were analyzed using a mixed-effects model to study the circadian variation, where drug-dependent differences could be seen.

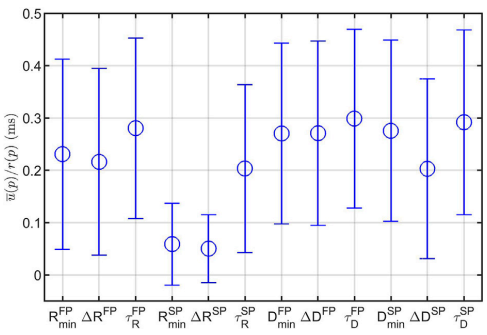

FIGURE 6
Mean (circles) ± one standard deviation (bars) of the parameter uncertainty estimates $u(p)$ over all recordings and all patients, normalized with the parameter ranges $r(p)$. Note that the model parameters R^{SP}_{min} and ΔR^{SP} have a lower uncertainty, indicating a higher impact on the resulting model outcome.

The model has previously been shown to be able to represent measured data in the form of histograms and Poincaré plots for 20-min long segments Karlsson et al. (2021). However, continuously estimating model parameters representing the refractory period and conduction delay in the AV node has previously not been possible. A previous study of the RR interval series has indicated that one interval delay in the autocorrelation gives sufficient information to replicate the dynamics of the RR interval series Karlsson et al. (2021). Hence, the Poincaré plot was chosen as a basis for the fitness function in order to take the one interval delay of the RR interval series into account, something that is not possible with an one-dimensional distribution representation such as the histogram. Moreover, since the model describes the impulses from the atria as a stochastic process, it is not possible to have a beat-to-beat level of detail in the fitness function, as evident by the RR interval series in Figure 4.

The choice of segment length N is a trade-off between robustness and time-resolution. The segment length N was set to 1000 RR intervals, corresponding to a time duration of 11 : 53 ± 03 : 28 (mm:ss), to capture changes in RR series characteristics on this time-scale while allowing sufficient estimation accuracy. As a consequence of the choice of N = 1000, the bin size of 50 m was used for the Poincaré plot-based error function. A smaller bin size would allow a more detailed match between model output and data, but would require more RR intervals.

From Figure 4, it is evident that the model and workflow can replicate the histogram and Poincaré plot of obtained RR interval series even for the case with the 95% highest ϵ. This was made possible by using the problem-specific GA presented in Section 2.4. Evolutionary algorithms - such as GA - and particle swarm optimization are the most common optimization algorithms used for solving dynamic optimization problems Yazdani et al. (2021); Mavrovouniotis et al. (2017).

One of the main challenges with dynamic optimization problems is the balance between exploration and exploitation, i.e., between searching for different promising regions of the search space, or searching for the optimal solutions within an already promising region. To keep a good level of exploration, the diversity in the population - usually defined as the average Euclidean distance between the individuals in the population - is often monitored. Thus, diversity loss is one of the most critical challenges Yazdani et al. (2021). A great number of methods have been developed to address this diversity loss, often based on randomizing individuals in the population that are too similar to others. For example, crowding - letting new individuals replace

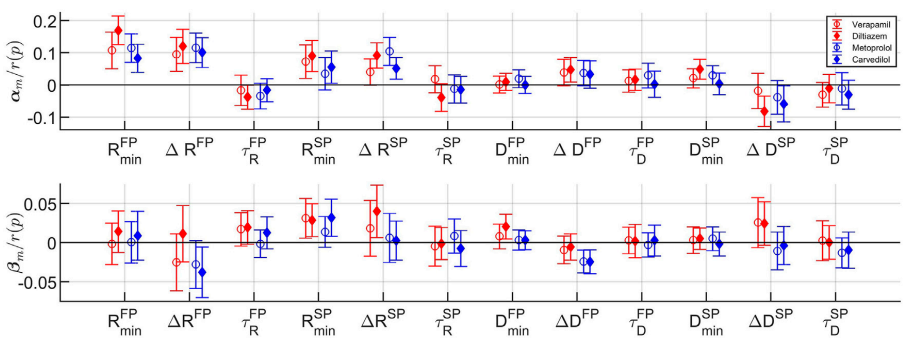

FIGURE 7
The fixed effects with corresponding 95% confidence intervals for the cosinor mean ***m*** (top) and cosinor amplitude ***a*** (bottom) for each model parameter (cf. Table 1) and drug. Confidence intervals not overlapping zero indicate significant difference from baseline (p <0.05).

the most similar individual in the population Kordestani et al. (2014) - or based on the age of the individuals Das et al. (2013). For GA, it is also possible to combat diversity loss by regulating the mutation rate. However, maintaining a good level of exploration using diversity does not take any information about the data into account. In contrast, changing the mutation rate, the number of immigrants, and the number of generations per segment using $\Delta P(i)$ - as was done in this study - takes information about the data directly into account. Additionally, the number of immigrants in the proposed GA ranges from 10–70%, which limits the initialization's effect on the overall results. Moreover, the results in Figure 3 indicate that the proposed problem-specific optimization method yields a better fit compared to the standard approach when the characteristics of the data change rapidly. On the other hand, when the characteristics of the data change slowly, the performance is similar even though the proposed algorithm is using fewer generations per segment. The number of RR intervals simulated with the model for each parameter set, N_{sim}, was set to 1500 in the GA based on a trade-off between computational complexity and variation based on the stochastic input sequence to the model. A simulation study relating the variation in ϵ and N_{sim} which was used to guide the decision is shown in the Supplementary Material, Section 1. Moreover, the thresholds for ΔP to determine how many generations are to be run per data segment were set so that approximately 55% are run for 1 generation, 30% are run for 2 generations, and the remaining 15% are run for 3.

A variation of Sobol's method was used to estimate the contribution to output variance for each model parameter, which was related to an increase in error by 10%. This more complex methodology was preferred over a one-at-a-time approach due to the large effect that interaction between model parameters has on the model output. Note that, unlike more traditional uncertainty estimates, this is not directly connected to a probability, since the error function used does not have a proper probabilistic interpretation. Thus, the uncertainty shall only be interpreted as a relative measure between the model parameters, between patients, and between the time of day. For example, it is evident in Figure 5 that the uncertainty for this patient is much lower during nighttime than daytime.

A linear mixed-effect model based on a cosinor analysis was used to derive the circadian variations. This method was used to quantify the circadian variation for the different drugs over the whole population, as well as the individual response to the drugs. The focus of this study is on the population effects of the different drug types in order to understand the drug-dependent differences in the conduction properties, something that needs to be understood before the method could be applicable on an individual level. Even though the focus of this study is on the population level, the individual responses are still of interest, especially for future work. For example, to predict individual responses to different drugs. As shown in Figure 5, the individual match is not optimal, thus a better tool for capturing the circadian variation is believed to be needed before robust analysis on an individual level is feasible. However, the cosinor analysis is an established model for characterizing circadian variation and has previously been used on the RATAF data-set to study heart rate variation Corino et al. (2015a).

From Table 3, in the parameters $R^{FP}_{\min}$ and ΔR^{FP}, we see a significantly increased refractory period relative to baseline in the FP for all four drugs. In addition, a significant increase in the SP for either $R^{SP}_{\min}$, or ΔR^{SP} could also be seen for all drugs. This increase is also visible in the fixed effect parameters $\boldsymbol{\alpha}_m$ in Figure 7, top panel. Electrophysiological studies of the two calcium channel blockers verapamil and diltiazem as well as the β-blocker metoprolol have shown that the drugs increase the refractoriness in the AV node Leboeuf et al. (1989); Talajic et al. (1992); Rizzon et al. (1978). Moreover, carvedilol has been shown to increase the effective refractory period in the atria during AF Kanoupakis et al. (2004). However, to the best of our knowledge, no studies have been conducted to determine the effect of carvedilol specifically for the refractory period in the AV node. Furthermore, conduction properties in the atria influence the model through the mean arrival rate λ, and thus affect the estimated parameters.

In addition, from Figure 7 bottom panel, it is shown that the two β-blockers reduce the circadian variation of the conduction delay more than the calcium channel blockers, as evident by ΔD^{FP} and ΔD^{SP}. Stimulation of the β_1-receptors - regulated by the autonomic nervous system - have been shown to increase the conduction velocity in the AV node Gordan et al. (2015). Hence, blocking this receptor using β-blocking drugs might decrease the autonomic nervous system effect, and thus reduce the circadian variation, yielding the presented results.

Also seen in Figure 7, the model parameters for the two β-blockers often behave similarly. However, the model parameters for the calcium channel blockers verapamil and diltiazem do not always align. In fact, the values for $\boldsymbol{\alpha}_m$ and $\boldsymbol{\beta}_m$ for verapamil are in several cases - most noticeably for $R^{FP}_{\min}$ for $\boldsymbol{\alpha}_m$ and ΔR^{FP}, ΔR^{SP}, and $D^{FP}_{\min}$ for $\boldsymbol{\beta}_m$ - similar to those of the two β-blockers. Interestingly, it has previously been proposed that the pharmacological effects of verapamil may partly be due to some degree of β-blockade Drici et al. (1993).

Moreover, the large confidence intervals in Figure 7, where the majority includes zero, are most likely due to the high inter-patient variability in parameter values. A confidence interval that includes zero would indicate that there is no significant difference from baseline. The high inertia and simplicity of the cosine are other factors in this. For example, some patients have more than one section with parameter values close to those during the night - possibly due to periods of sleep during the day - which a cosine with a period of 24 h could not capture.

4.1 Study limitations and future perspectives

The present model of the AV node accounts for dual pathway physiology and rate dependent changes in conduction delay and refractoriness and can simulate retrograde conduction. However, it is not able to simulate some physiological interesting phenomena such as AV node re-entry.

A limited range for the model parameters was used to make the optimization more efficient. The choice of the boundaries was guided by electrophysiological measurements from previous clinical studies while keeping a conservative range to not exclude realistic values. The maximal refractory period for the model - given as the sum of $R_{\min}$ and ΔR - lies in the range [150, 1350] ms and was set to include the effective refractory period of the AV node, which has been reported as 361 ± 57 and 283 ± 48 m for the FP and SP, respectively Natale et al. (1994). Furthermore, the conduction delay of the whole model is given by the sum of $D_{\min}$ and ΔD multiplied by the number of nodes, which lies in the range [0, 1050] ms. Thus, it includes all realistic PR intervals, which rarely exceed 200 m Schumacher et al. (2017). Even though the boundaries were conservatively chosen, we cannot exclude the possibility that a different choice would have affected the resulting parameter values. Moreover, since the parameters might be hard to interpret, combining the model parameters associated with the same conduction property, i.e., the two refractory periods and the two conduction delays, to create more interpretable representations, is interesting.

As mentioned before, high inertia and simplicity of the cosine are limiting factors for the assessment of circadian variation. However, the cosinor analysis is an established model for characterizing circadian variation and is thus important for clear and interpretable results. Using the estimated uncertainty to weight the estimated parameters is one possible approach to make the cosine fit the estimates better. Other methods to capture the differences in the AV node parameters over time, such as time-frequency analysis of the estimated parameter trends, should also be investigated.

It should be noted that the estimated model parameters are not clinically validated for assessment of AV node refractoriness and conduction delay. Hence, the clinical significance of the results should be interpreted with caution. However, the overall findings for the different drugs on the whole population are, as discussed above, in accordance with electrophysiological studies. Another limitation is the sample size of 60 patients in combination with the high inter-patient variability in parameter values, as seen in the large standard deviation in Table 3. This makes the population estimates more uncertain, partly causing the large confidence intervals seen in Figure 7.

A natural continuation of this work is to analyze the estimated model parameters during baseline, possible in combinations with other factors such as age or gender, to predict the mean heart rate under the influence of the different drugs. This in turn could be used to assist in personalized treatment selection during AF.

5 Conclusion

We have presented a framework - including a mathematical model and a genetic algorithm - which for the first time enables characterization of the refractory period and the conduction delay of the AV node during 24 h for patients with permanent AF, solely based on non-invasive data.

With ECG from AF patients during baseline and under the influence of different rate control drugs, a mixed-model framework was used on the estimated model parameters to compare the impact on circadian variation between drugs. From this, differences in conduction delay could be identified between β-blockers and calcium channel blockers, which was previously unknown.

Data availability statement

The data analyzed in this study is subject to the following licenses/restrictions: The estimated model parameters $\boldsymbol{\theta}_{(i)}$ and associated uncertainty estimate u(p) supporting the conclusions for this article will be available from MK upon request. The ECG data are owned by Vestre Viken Hospital Trust, and requests for access can be made to SU. The code for the model together with an user example can be found at https://github.com/FraunhoferChalmersCentre/AV-node-model.

Ethics statement

The studies involving human participants were reviewed and approved by Regional ethics committee and the Norwegian Medicines Agency. The patients/participants provided their written informed consent to participate in this study.

Author contributions

MK, FS, and MW contributed to the conception and design of the study. SU was responsible for the clinical study. FS was responsible for the ECG pre-processing and estimation of the RR interval series and AFR trends. MK wrote the manuscript and designed the genetic algorithm, the method for the uncertainty estimation, and the circadian variation model, with advice, suggestions, and supervision from FS and MW. PP and SU analyzed and gave medical interpretations of the results. FS and MW supervised the project and reviewed the manuscript during the whole writing process. All authors contributed to manuscript revision, read, and approved the submitted version.

Funding

This work was supported by the Swedish Foundation for Strategic Research (Grant FID18-0023), the Swedish Research Council (Grant VR 2019–04272), and the Crafoord Foundation (Grant 20200605).

Conflict of interest

The authors declare that the research was conducted in the absence of any commercial or financial relationships that could be construed as a potential conflict of interest.

Publisher's note

Supplementary material

The Supplementary Material for this article can be found online at: https://www.frontiersin.org/articles/10.3389/fphys.2022.976526/full#supplementary-material

References

Benjamin, E. J., Muntner, P., Alonso, A., Bittencourt, M. S., Callaway, C. W., Carson, A. P., et al. (2019). Heart disease and stroke statistics-2019 update a report from the American heart association. *Circulation* 139, e56–e528. doi:10.1161/CIR.0000000000000659

Benjamini, Y., and Hochberg, Y. (1995). Controlling the false discovery rate: A practical and powerful approach to multiple testing. *J. R. Stat. Soc. Ser. B Methodol.* 57, 289–300. doi:10.1111/j.2517-6161.1995.tb02031.x

Billette, J., and Nattel, S. (1994). Dynamic behavior of the atrioventricular node: A functional model of interaction between recovery, facilitation, and fatigue. *J. Cardiovasc. Electrophysiol.* 5, 90–102. doi:10.1111/j.1540-8167.1994.tb01117.x

Climent, A. M., Guillem, M. S., Husser, D., Castells, F., Millet, J., and Bollmann, A. (2010). Role of the atrial rate as a factor modulating ventricular response during atrial fibrillation. *Pacing Clin. Electrophysiol.* 33, 1510–1517. doi:10.1111/j.1540-8159.2010.02837.x

Climent, A. M., Guillem, M. S., Zhang, Y., Millet, J., and Mazgalev, T. (2011). Functional mathematical model of dual pathway av nodal conduction. *Am. J. Physiol. Heart Circ. Physiol.* 300, H1393–H1401. doi:10.1152/ajpheart.01175.2010

Corino, V. D., Platonov, P. G., Enger, S., Tveit, A., and Ulimoen, S. R. (2015a). Circadian variation of variability and irregularity of heart rate in patients with permanent atrial fibrillation: Relation to symptoms and rate control drugs. *Am. J. Physiol. Heart Circ. Physiol.* 309, H2152–H2157. doi:10.1152/ajpheart.00300.2015

Corino, V. D., Sandberg, F., Lombardi, F., Mainardi, L. T., and Sörnmo, L. (2013). Atrioventricular nodal function during atrial fibrillation: Model building and robust estimation. *Biomed. Signal Process. Control* 8, 1017–1025. doi:10.1016/j.bspc.2012.10.006

Corino, V. D., Sandberg, F., Mainardi, L. T., and Sornmo, L. (2011). An atrioventricular node model for analysis of the ventricular response during atrial fibrillation. *IEEE Trans. Biomed. Eng.* 58, 3386–3395. doi:10.1109/TBME.2011.2166262

Corino, V. D., Ulimoen, S. R., Enger, S., Mainardi, L. T., Tveit, A., and Platonov, P. G. (2015b). Rate-control drugs affect variability and irregularity measures of rr intervals in patients with permanent atrial fibrillation. *J. Cardiovasc. Electrophysiol.* 26, 137–141. doi:10.1111/jce.12580

Das, S., Mandal, A., and Mukherjee, R. (2013). An adaptive differential evolution algorithm for global optimization in dynamic environments. *IEEE Trans. Cybern.* 44, 966–978. doi:10.1109/TCYB.2013.2278188

Di Carlo, A., Bellino, L., Consoli, D., Mori, F., Zaninelli, A., Baldereschi, M., et al. (2019). Prevalence of atrial fibrillation in the Italian elderly population and projections from 2020 to 2060 for Italy and the European Union: The fai project. *Europace* 21, 1468–1475. doi:10.1093/europace/euz141

Drici, M., Jacomet, Y., Iacono, P., and Lapalus, P. (1993). Is verapamil also a non-selective beta blocker? *Int. J. Clin. Pharmacol. Ther. Toxicol.* 31, 27–30.

Gordan, R., Gwathmey, J. K., and Xie, L.-H. (2015). Autonomic and endocrine control of cardiovascular function. *World J. Cardiol.* 7, 204–214. doi:10.4330/wjc.v7.i4.204

Henriksson, M., Corino, V. D., Sörnmo, L., and Sandberg, F. (2015). A statistical atrioventricular node model accounting for pathway switching during atrial fibrillation. *IEEE Trans. Biomed. Eng.* 63, 1842–1849. doi:10.1109/TBME.2015.2503562

Hindricks, G., Potpara, T., Dagres, N., Arbelo, E., Bax, J. J., Blomström-Lundqvist, C., et al. (2021). 2020 ESC guidelines for the diagnosis and management of atrial fibrillation developed in collaboration with the European association for cardio-thoracic surgery (EACTS) the task force for the diagnosis and management of atrial fibrillation of the European society of cardiology (ESC) developed with the special contribution of the European heart rhythm association (EHRA) of the ESC. *Eur. Heart J.* 42, 373–498. doi:10.1093/eurheartj/ehaa612

Inada, S., Hancox, J., Zhang, H., and Boyett, M. (2009). One-dimensional mathematical model of the atrioventricular node including atrio-nodal, nodal, and nodal-his cells. *Biophys. J.* 97, 2117–2127. doi:10.1016/j.bpj.2009.06.056

Jørgensen, P., Schäfer, C., Guerra, P. G., Talajic, M., Nattel, S., and Glass, L. (2002). A mathematical model of human atrioventricular nodal function incorporating concealed conduction. *Bull. Math. Biol.* 64, 1083–1099. doi:10.1006/bulm.2002.0313

Kanoupakis, E. M., Manios, E. G., Mavrakis, H. E., Tzerakis, P. G., Mouloudi, H. K., and Vardas, P. E. (2004). Comparative effects of carvedilol and amiodarone on conversion and recurrence rates of persistent atrial fibrillation. *Am. J. Cardiol.* 94, 659–662. doi:10.1016/j.amjcard.2004.05.037

Karlsson, M., Sandberg, F., Ulimoen, S. R., and Wallman, M. (2021). Non-invasive characterization of human av-nodal conduction delay and refractory period during atrial fibrillation. *Front. Physiol.* 12, 728955. doi:10.3389/fphys.2021.728955

Kordestani, J. K., Rezvanian, A., and Meybodi, M. R. (2014). Cdepso: A bi-population hybrid approach for dynamic optimization problems. *Appl. Intell. (Dordr).* 40, 682–694. doi:10.1007/s10489-013-0483-z

Lagarias, J. C., Reeds, J. A., Wright, M. H., and Wright, P. E. (1998). Convergence properties of the Nelder–Mead simplex method in low dimensions. *SIAM J. Optim.* 9, 112–147. doi:10.1137/s1052623496303470

Lagerholm, M., Peterson, C., Braccini, G., Edenbrandt, L., and Sornmo, L. (2000). Clustering ecg complexes using hermite functions and self-organizing maps. *IEEE Trans. Biomed. Eng.* 47, 838–848. doi:10.1109/10.846677

Leboeuf, J., Lamar, J., Massingham, R., and Ponsonnaille, J. (1989). Electrophysiological effects of bepridil and its quaternary derivative cerm 11888 in closed chest anaesthetized dogs: A comparison with verapamil and diltiazem. *Br. J. Pharmacol.* 98, 1351–1359. doi:10.1111/j.1476-5381.1989.tb12684.x

Mangin, L., Vinet, A., Pagé, P., and Glass, L. (2005). Effects of antiarrhythmic drug therapy on atrioventricular nodal function during atrial fibrillation in humans. *Europace* 7, S71–S82. doi:10.1016/j.eupc.2005.03.016

Mase, M., Disertori, M., Marini, M., and Ravelli, F. (2017). Characterization of rate and regularity of ventricular response during atrial tachyarrhythmias. insight on atrial and nodal determinants. *Physiol. Meas.* 38, 800–818. doi:10.1088/1361-6579/aa6388

Masè, M., Glass, L., Disertori, M., and Ravelli, F. (2012). Nodal recovery, dual pathway physiology, and concealed conduction determine complex av dynamics in human atrial tachyarrhythmias. *Am. J. Physiol. Heart Circ. Physiol.* 303, H1219–H1228. doi:10.1152/ajpheart.00228.2012

Masè, M., Marini, M., Disertori, M., and Ravelli, F. (2015). Dynamics of av coupling during human atrial fibrillation: Role of atrial rate. *Am. J. Physiol. Heart Circ. Physiol.* 309, H198–H205. doi:10.1152/ajpheart.00726.2014

Mavrovouniotis, M., Li, C., and Yang, S. (2017). A survey of swarm intelligence for dynamic optimization: Algorithms and applications. *Swarm Evol. Comput.* 33, 1–17. doi:10.1016/j.swevo.2016.12.005

Natale, A., Klein, G., Yee, R., and Thakur, R. (1994). Shortening of fast pathway refractoriness after slow pathway ablation. effects of autonomic blockade. *Circulation* 89, 1103–1108. doi:10.1161/01.cir.89.3.1103

Rizzon, P., Di Biase, M., Chiddo, A., Mastrangelo, D., and Sorgente, L. (1978). Electrophysiological properties of intravenous metoprolol in man. *Br. Heart J.* 40, 650–655. doi:10.1136/hrt.40.6.650

Sandberg, F., Stridh, M., and Sornmo, L. (2008). Frequency tracking of atrial fibrillation using hidden markov models. *IEEE Trans. Biomed. Eng.* 55, 502–511. doi:10.1109/TBME.2007.905488

Schumacher, K., Dagres, N., Hindricks, G., Husser, D., Bollmann, A., and Kornej, J. (2017). Characteristics of pr interval as predictor for atrial fibrillation: Association with biomarkers and outcomes. *Clin. Res. Cardiol.* 106, 767–775. doi:10.1007/s00392-017-1109-y

Shrier, A., Dubarsky, H., Rosengarten, M., Guevara, M. R., Nattel, S., and Glass, L. (1987). Prediction of complex atrioventricular conduction rhythms in humans with use of the atrioventricular nodal recovery curve. *Circulation* 76, 1196–1205. doi:10.1161/01.cir.76.6.1196

Sobol, I. M. (2001). Global sensitivity indices for nonlinear mathematical models and their Monte Carlo estimates. *Math. Comput. Simul.* 55, 271–280. doi:10.1016/s0378-4754(00)00270-6

Stridh, M., and Sornmo, L. (2001). Spatiotemporal qrst cancellation techniques for analysis of atrial fibrillation. *IEEE Trans. Biomed. Eng.* 48, 105–111. doi:10.1109/10.900266

Sun, J., Amellal, F., Glass, L., and Billette, J. (1995). Alternans and period-doubling bifurcations in atrioventricular nodal conduction. *J. Theor. Biol.* 173, 79–91. doi:10.1006/jtbi.1995.0045

Talajic, M., Lemery, R., Roy, D., Villemaire, C., Cartier, R., Coutu, B., et al. (1992). Rate-dependent effects of diltiazem on human atrioventricular nodal properties. *Circulation* 86, 870–877. doi:10.1161/01.cir.86.3.870

Ulimoen, S. R., Enger, S., Carlson, J., Platonov, P. G., Pripp, A. H., Abdelnoor, M., et al. (2013). Comparison of four single-drug regimens on ventricular rate and arrhythmia-related symptoms in patients with permanent atrial fibrillation. *Am. J. Cardiol.* 111, 225–230. doi:10.1016/j.amjcard.2012.09.020

Wahde, M. (2008). *Biologically inspired optimization methods: An introduction*. Southampton: WIT press.

Woolson, R. F. (2007). *Wilcoxon signed-rank test*. Wiley encyclopedia of clinical trials, 1–3.

Yazdani, D., Cheng, R., Yazdani, D., Branke, J., Jin, Y., and Yao, X. (2021). A survey of evolutionary continuous dynamic optimization over two decades—Part a. *IEEE Trans. Evol. Comput.* 25, 609–629. doi:10.1109/tevc.2021.3060014

Paper III

frontiers | Frontiers in Physiology

TYPE Original Research
PUBLISHED 12 January 2024
DOI 10.3389/fphys.2023.1287365

OPEN ACCESS

EDITED BY
Xin Li,
University of Leicester, United Kingdom

REVIEWED BY
Michela Masè,
University of Trento, Italy
Elena Ryzhii,
Fukushima Medical University, Japan

*CORRESPONDENCE
Frida Sandberg,
frida.sandberg@bme.lth.se

†These authors share last authorship

RECEIVED 01 September 2023
ACCEPTED 18 December 2023
PUBLISHED 12 January 2024

CITATION
Karlsson M, Platonov PG, Ulimoen SR, Sandberg F and Wallman M (2024), Model-based estimation of AV-nodal refractory period and conduction delay trends from ECG.
Front. Physiol. 14:1287365.
doi: 10.3389/fphys.2023.1287365

Model-based estimation of AV-nodal refractory period and conduction delay trends from ECG

Mattias Karlsson[1,2], Pyotr G. Platonov[3], Sara R. Ulimoen[4], Frida Sandberg[2]*† and Mikael Wallman[1†]

[1]Department of Systems and Data Analysis, Fraunhofer-Chalmers Centre, Gothenburg, Sweden, [2]Department of Biomedical Engineering, Lund University, Lund, Sweden, [3]Department of Cardiology, Clinical Sciences, Lund University, Lund, Sweden, [4]Department of Medical Research, Vestre Viken Hospital Trust, Bærum Hospital, Drammen, Norway

Introduction: Atrial fibrillation (AF) is the most common arrhythmia, associated with significant burdens to patients and the healthcare system. The atrioventricular (AV) node plays a vital role in regulating heart rate during AF by filtering electrical impulses from the atria. However, it is often insufficient in regards to maintaining a healthy heart rate, thus the AV node properties are modified using rate-control drugs. Moreover, treatment selection during permanent AF is currently done empirically. Quantifying individual differences in diurnal and short-term variability of AV-nodal function could aid in personalized treatment selection.

Methods: This study presents a novel methodology for estimating the refractory period (RP) and conduction delay (CD) trends, and their uncertainty in the two pathways of the AV node during 24 h using non-invasive data. This was achieved by utilizing a network model together with a problem-specific genetic algorithm and an approximate Bayesian computation algorithm. Diurnal variability in the estimated RP and CD was quantified by the difference between the daytime and nighttime estimates, and short-term variability was quantified by the Kolmogorov-Smirnov distance between adjacent 10-min segments in the 24-h trends. Additionally, the predictive value of the derived parameter trends regarding drug outcome was investigated using several machine learning tools.

Results: Holter electrocardiograms from 51 patients with permanent AF during baseline were analyzed, and the predictive power of variations in RP and CD on the resulting heart rate reduction after treatment with four rate control drugs was investigated. Diurnal variability yielded no correlation to treatment outcome, and no prediction of drug outcome was possible using the machine learning tools. However, a correlation between the short-term variability for the RP and CD in the fast pathway and resulting heart rate reduction during treatment with metoprolol ($\rho = 0.48, p < 0.005$ in RP, $\rho = 0.35, p < 0.05$ in CD) were found.

Discussion: The proposed methodology enables non-invasive estimation of the AV node properties during 24 h, which—indicated by the correlation between the

short-term variability and heart rate reduction—may have the potential to assist in treatment selection.

KEYWORDS

AV node model, atrial fibrillation, atrioventricular node, mathematical modeling, genetic algorithm, approximate Bayesian computation, ECG, rate control drugs

1 Introduction

Atrial fibrillation (AF) is the most common sustained cardiac arrhythmia and a significant burden for patients and the healthcare system Hindricks et al. (2020). The prevalence of AF is currently estimated to be between 2% and 4% worldwide Benjamin et al. (2019). In addition, the number of AF cases in the European Union is estimated to increase by 89% between 2016 and 2060 Di Carlo et al. (2019). Atrial fibrillation is characterized by disorganized electrical activity in the atria, leading to rapid and irregular contraction, and is associated with an increased risk of mortality, predominantly due to heart failure or stroke Andrew et al. (2013).

The atrioventricular (AV) node acts as the only electrical connection between the atria and ventricles and partly protects the ventricles from the rapid and irregular electrical activity in the atria during AF. It can be functionally divided into two pathways, the fast pathway (FP) and the slow pathway (SP), interconnected at the Bundle of His Kurian et al. (2010). The AV node either blocks an incoming impulse, based on its refractory period (RP), or sends it through with a delay, based on its conduction delay (CD). The AV node is thus the most essential part in regulating the heart rate during AF, and the RP and CD are the two most important properties of the AV node, deciding its filtering capability.

The AV node during permanent AF is in many cases insufficient in regards to maintaining a healthy heart rate. Therefore, the AV node properties are often modified by treatment with rate control drugs, with β-blockers and calcium channel blockers recommended as first-line treatment Hindricks et al. (2020). Common β-blockers for AF treatment are metoprolol and carvedilol, which block the $\beta 1$ receptors in the heart in order to reduce the effect of the sympathetic nervous system on the heart Dorian (2005). Common calcium channel blockers are verapamil and diltiazem, which prevent the L-type calcium channels in the cardiac myocytes from opening in order to reduce conduction in the AV node Eisenberg et al. (2004). However, due to the significant and poorly understood individual variability, the choice of drug is currently made empirically for each patient Hindricks et al. (2020). This could lead to a prolonged time until successful treatment, and possibly result in a suboptimal final choice of drug. Since the two recommended first-line treatments have different physiological effects on the AV node, assessing the patient-specific properties of the AV node has the potential to assist in treatment selection. Specifically, we hypothesize that β-blockers would exhibit an increased effect (more reduced heart rate) when variations in the AV node properties are prominent since β-blockers reduce the effect of the sympathetic nervous system.

The AV node has previously been studied using several mathematical models based on invasive data from humans and animals Billette and Nattel (1994); Jørgensen et al. (2002); Mangin et al. (2005); Inada et al. (2009); Climent et al. (2011a); Masè et al. (2012), Masè et al. (2015); Ryzhii and Ryzhii (2023). However, in order for a model to be clinically applicable on an individual level, the model parameters should ideally be identifiable from non-invasive data, such as the electrocardiogram (ECG). A statistical model of the AV node with dual pathway physiology using the RR interval series and the atrial fibrillatory rate (AFR) for model fitting has been proposed Corino et al. (2011), Corino et al. (2013); Henriksson et al. (2015). However, the model lumps RP and CD together, limiting its interpretability.

We have previously proposed a network model of the AV node capable of distinguishing the RP and CD in each pathway Karlsson et al. (2021), together with a framework for continuously estimating its twelve model parameters from 24-h Holter ECG Karlsson et al. (2022). Although promising, the characterization of the AV node was still limited by the number of model parameters and their intrinsic complex dependencies, where a large change in the model parameters could result in a very small change in the RP or CD, thus, making their interpretation a non-trivial task. For a modeling approach to gain acceptance in a clinical context, the outcome should be readily interpretable by medical professionals; a fact that has become especially relevant with the increasing use of advanced modeling and machine learning techniques Teng et al. (2022); Trayanova et al. (2021). Additionally, in Karlsson et al. (2022), a version of Sobol's method was applied to quantify uncertainty in the parameter estimates. However, these uncertainty estimates were not directly interpretable as probabilities and could thus only be used as a relative measure between the model parameters, between patients, or between different times of the day. When the extent of the uncertainty is unknown, uncertain estimates have the potential to mislead decision-making processes or further analysis of the trends. A proper quantification of the uncertainty is thus advantageous in order to fully understand the estimates.

In the present study, we propose a novel methodology for estimating the RP and CD of both pathways of the AV node and the associated uncertainty continuously over 24 h. The methodology comprises a genetic algorithm (GA) for initial model parameter estimation and an approximate Bayesian computation (ABC) algorithm to refine the estimates, together with a simulation approach to map model parameters to RP and CD in order to increase interpretability. In addition to refining the estimates, the ABC algorithm provides samples from the Bayesian posterior distribution of the AV node properties, hereafter denoted the posterior, enabling proper quantification of the uncertainty of the estimated properties. We use these novel tools in an exploratory manner to analyze Holter ECGs from 51 patients during baseline in combination with their respective drug responses to identify potential markers for differences in drug response. Specifically, we analyze the correlation between diurnal and short-term variability and drug outcomes, as well as train several machine learning models to predict drug outcomes.

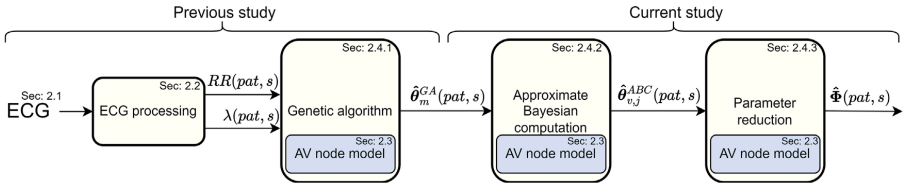

FIGURE 1
A schematic overview of the methodology, from ECG to estimations of the RP and CD. $\hat{\theta}_m^{GA}(pat,s)$ referees to the estimates found by the GA, as described in Section 2.4.1; $\hat{\theta}_{v,j}^{ABC}(pat,s)$ referees to the estimates found by the ABC algorithm, as described in Section 2.4.2; and $\hat{\Phi}(pat,s)$ referees to the full estimates of R^{FP}, R^{SP}, D^{FP}, D^{SP}, as described in Section 2.4.3. Previous study refers to Karlsson et al. (2022).

2 Materials and methods

The overall method for assessing the RP and CD of the two pathways in the AV node for each patient (*pat*) can be divided into four stages, as shown in Figure 1. Firstly, 24-h Holter ECGs are processed to extract RR interval series and AFR trends, divided into 10-min segments (s) with a 50% overlap, as described in Sections 2.1, 2.2. Secondly, the parameters for the network model of the AV node, described in Section 2.3, are fitted to the RR interval series and AFR in each segment using a problem-specific dynamic GA as described in Section 2.4.1. The GA-derived estimates are subsequently used as inputs to an ABC algorithm to refine the estimates and estimate the posterior of the model parameters, as described in Section 2.4.2. Additionally, a simulation study was performed to evaluate parameter estimates produced by the ABC algorithm in relation to those produced by the GA, described in Supplementary Material S1. These model parameter estimates are finally used to simulate data with the model while tracking the RP and CD used for the two pathways, as described in Section 2.4.3. This results in a distribution of the RP and CD in the FP and the SP for each 10-min segment. Finally, the possibility to predict treatment outcomes using the estimated distributions is evaluated, as described in Section 2.5.

2.1 ECG data

Data from the Rate Control in Atrial Fibrillation (RATAF) study, a randomized, investigator-blind, crossover study, approved by the regional ethics committee and the Norwegian Medicines Agency and conducted in accordance with the Helsinki Declaration, is analyzed in this study Ulimoen et al. (2013). Specifically, 24-h ambulatory ECGs from 60 patients (mean age 71 ± 9 years, 18 women) with permanent AF, no heart failure, or symptomatic ischemic heart disease, recorded during baseline, are used for the estimation of patient-specific AV node properties. In addition to the baseline ECG, the relative change in the 24-h average heart rate (ΔHR) for treatment with the two calcium channel blockers verapamil and diltiazem and the two β-blockers metoprolol and carvedilol are used to evaluate the therapeutic implications of the estimated AV node properties. The calculation of ΔHR is based on the RR interval series extracted from the ECG, as explained in Section 2.2.

2.2 ECG processing

The RR interval series is extracted from the ECG for each patient and divided into 10-min segments with a 50% overlap ($\boldsymbol{RR}(pat,s)$), where RR intervals following and preceding QRS-complexes with deviating morphology are excluded from the series Lagerholm et al. (2000). Segments with excessive noise can lead to a large number of undetected beats and thus an unrealistically low heart rate. Hence, each 10-min segment is divided into minute-long non-overlapping intervals, and the whole 10-min segment is excluded from further analysis if any 1-min interval has fewer than 20 detected beats. Patients with RR interval series with a total duration shorter than 12 h are excluded from further analysis. The RR interval series corresponding to the four rate control drugs are calculated equivalently.

Spatiotemporal QRST cancellation is employed to extract the f-waves from the ECG Stridh et al. (2001). Subsequently, the fundamental frequency of the extracted f-waves is tracked using a hidden Markov model-based method to extract an AFR trend for each patient with a resolution of 1 minute Sandberg et al. (2008). For time segments where the AFR could not be obtained due to excessive noise, but the RR interval series could, the AFR is set to the closest observed AFR value.

2.3 Network model of the AV node

Our network model of the AV node, introduced in Karlsson et al. (2021), describes the AV node as two pathways (the SP and the FP) comprising 10 nodes each. The last nodes of each pathway are connected with each other and with a coupling node, as illustrated in Figure 2. Each pathway node corresponds physiologically to a localized section of the respective pathway, and the interconnection of the modeled pathways represents the interconnection between the two pathways seen in the AV node Kurian et al. (2010). Furthermore, the coupling node corresponds physiologically to the Purkinje fibers and Bundle of His.

Atrial impulses are modeled by a Poisson process with mean arrival rate λ. The impulses are assumed to reach the first nodes of SP and FP simultaneously. Each network node can be either in a refractory state or in a non-refractory state. A node in its refractory state will block incoming impulses, and a node in its non-refractory

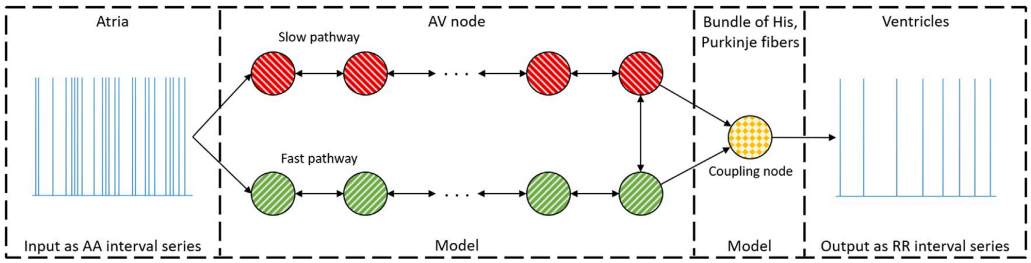

FIGURE 2
A schematic representation of the network model where the yellow node represents the coupling node, the red nodes the SP, the green nodes the FP, and arrows the direction for impulse conduction. For readability, only a subset of the 21 nodes is shown. Reproduced from Karlsson et al. (2021), licensed under CC BY 4.0.

state will transmit an incoming impulse to all adjacent nodes with an added conduction delay before entering its refractory state. The RP ($R_i(n)$) and CD ($D_i(n)$) for node i are updated for each incoming impulse n according to Eqs 1–3,

$$R_i(n) = R_{min} + \Delta R\left(1 - e^{-\tilde{t}_i(n)/\tau_R}\right) \tag{1}$$

$$D_i(n) = D_{min} + \Delta D e^{-\tilde{t}_i(n)/\tau_D}, \tag{2}$$

$$\tilde{t}_i(n) = t_i(n) - \left(t_i(n-1) + R_i(n-1)\right), \tag{3}$$

where, $\tilde{t}_i(n)$ is the diastolic interval preceding impulse n and $t_i(n)$ is the arrival time of impulse n at node i. When $\tilde{t}_i(n) < 0$, the node is in its refractory state and will block incoming impulses. All parameters are fixed for each pathway, resulting in three model parameters for the RP in the FP (R^{FP}_{min}, ΔR^{FP}, τ^{FP}_R); three model parameters for the CD in the FP (D^{FP}_{min}, ΔD^{FP}, τ^{FP}_D); three model parameters for the RP in the SP (R^{SP}_{min}, ΔR^{SP}, τ^{SP}_R); three model parameters for the CD in the SP (D^{SP}_{min}, ΔD^{SP}, τ^{SP}_D). These twelve model parameters constitute the mode parameter vector $\boldsymbol{\theta}$. In addition, the RP in the coupling node is fixed to the mean of the ten shortest RR intervals in the data, and its CD is fixed at 60 ms Karlsson et al. (2021).

2.4 Parameter estimation

For each 10-min segment, the mean arrival rate for the Poisson process λ is estimated as the mean of the AFR trend ($\hat{\lambda}(pat,s)$), and the model parameters $\hat{\boldsymbol{\theta}}(pat,s)$ are estimated using a GA together with an ABC algorithm.

An error function (ϵ) based on the Poincaré plot, i.e., a scatter plot of successive pairs of RR intervals, is used to quantify the difference between $\boldsymbol{RR}(pat,s)$ and a simulated RR interval series ($\tilde{\boldsymbol{RR}}$). The successive pairs of RR intervals for $\boldsymbol{RR}(pat,s)$ and $\tilde{\boldsymbol{RR}}$ are placed in two-dimensional bins covering the interval between 250 and 1,800 ms in steps of 50 ms, resulting in $K = 961$ bins, which we refer to as the Poincaré histogram. The error function, based on the work presented in Karlsson et al. (2021), is computed according to Eq. 4,

$$\epsilon = \frac{1}{K}\sum_{k=1}^{K}\frac{\left(x_k - \frac{1}{t_{norm}}\tilde{x}_k\right)^2}{\sqrt{x_k}}, \tag{4}$$

where x_k and $\tilde{x}_k$ are the numbers of RR intervals in the kth bin of $\boldsymbol{RR}(pat,s)$ and $\tilde{\boldsymbol{RR}}$, respectively. Additionally, t_{norm} acts as a normalizing constant and is calculated as the duration of $\tilde{\boldsymbol{RR}}$ divided by the duration of $\boldsymbol{RR}(pat,s)$.

2.4.1 Genetic algorithm

A problem-specific dynamic GA based on the work presented in Karlsson et al. (2022) is used to get an initial estimate of $\boldsymbol{\theta}(pat,s)$ in every segment. A GA is a metaheuristic, made up of a population of candidate solutions, called individuals in the GA terminology. However, to avoid confusion with individuals in the context of people, here we will call them parameter vectors. Thus, using the problem-specific dynamic GA results in a population of parameter vectors denoted $\hat{\boldsymbol{\theta}}^{GA}_m(pat,s)$, where m denotes the mth fittest parameter vector in the population after completion of the GA, i.e., the parameter vector with the mth lowest ϵ. The hyper-parameters in the algorithm are tuned during the optimization using the difference between the Poincaré histograms in pairs of consecutive segments (ΔP) Karlsson et al. (2022). This difference is calculated using Eq. 4 with x_k and $\tilde{x}_k$ as the number of RR intervals in each bin of the current segment and the following one, respectively.

The GA uses a population of 300 parameter vectors, tournament selection, a two-point crossover, and creep mutation. To avoid premature convergence and to increase performance, immigration through replacement of the least-fit parameter vectors in the population is performed, following the work in Karlsson et al. (2022). Furthermore, ΔP is used to determine the number of generations that the GA runs before moving to the next data segment, between two and seven. The initialization of the parameter vectors is done using latin hypercube sampling within the ranges given in Table 1. These values also act as boundaries for the model parameters in the GA and are set with guidance from electrophysiological measurements from previous clinical studies while keeping a conservative range to not exclude realistic values. For further details about the algorithm, see Karlsson et al. (2022).

TABLE 1 Parameter ranges for the GA and the ABC PMC algorithm.

Parameters	$R^{FP}_{min}, R^{SP}_{min}$	$\Delta R^{FP}, \Delta R^{SP}$	$D^{FP}_{min}, D^{SP}_{min}$	$\Delta D^{FP}, \Delta D^{SP}$	$T^{FP}_R, T^{SP}_R, T^{FP}_D, T^{SP}_D$
GA (ms)	[100, 1,000]	[0, 1,000]	[2, 50]	[0, 100]	[25, 500]
ABC (ms)	[30, 1,300]	[0, 1,300]	[0.1, 80]	[0, 130]	[10, 700]

2.4.2 Approximate Bayesian computation

To estimate the posterior $p(\boldsymbol{\theta}|\boldsymbol{RR}(pat,s),\widehat{\lambda}(pat,s))$, an approximate Bayesian computation population Monte Carlo sampling (ABC PMC) algorithm is used Turner and Van Zandt (2012). The pseudo-code for the problem-specific ABC PMC is shown in Algorithm 1. The ABC PMC uses a set of $N_p = 100$ particles to estimate the posterior in each RR segment independently, which are updated iteratively for eight iterations (j). Each particle corresponds to a model parameter vector, denoted $\widehat{\boldsymbol{\theta}}^{ABC}_{v,j}$, where v corresponds to the vth particle for the jth iteration. Hence, the particles after the eighth iteration are used as the estimate for the posterior. The algorithm is sped up by utilizing the results from the GA to create the initial population. To construct the initial population, twenty particles are drawn from five different normal distributions, having the five most fit parameter vectors in the GA as means, and identical covariance matrices calculated as the covariance of the 25 most fit parameter vectors in the GA. Hence, the five normal distributions are defined as: $\mathcal{N}(\widehat{\boldsymbol{\theta}}^{GA}_1(pat,s),\boldsymbol{\Sigma}_{init}(pat,s))$, $\mathcal{N}(\widehat{\boldsymbol{\theta}}^{GA}_2(pat,s),\boldsymbol{\Sigma}_{init}(pat,s))$, $\mathcal{N}(\widehat{\boldsymbol{\theta}}^{GA}_3(pat,s),\boldsymbol{\Sigma}_{init}(pat,s))$, $\mathcal{N}(\widehat{\boldsymbol{\theta}}^{GA}_4(pat,s),\boldsymbol{\Sigma}_{init}(pat,s))$, and $\mathcal{N}(\widehat{\boldsymbol{\theta}}^{GA}_5(pat,s),\boldsymbol{\Sigma}_{init}(pat,s))$, where the covariance matrix $\boldsymbol{\Sigma}_{init}(pat,s) = \mathrm{Cov}(\widehat{\boldsymbol{\theta}}^{GA}_{1:25}(pat,s))$ where 1:25 denotes $[1,2,\ldots,25]$ for convenience. During each iteration, each particle has a probability of being chosen based on an assigned weight, computed according to Eq. 5 Beaumont et al. (2009)

$$\boldsymbol{w}_{v,j} = \left(\sum_{k=1}^{N_p} \boldsymbol{w}_{k,j-1} \mathcal{N}\left(\widehat{\boldsymbol{\theta}}^{ABC}_{k,j-1} | \widehat{\boldsymbol{\theta}}^{ABC}_{v,j}, \boldsymbol{\Sigma}_{j-1}\right) \right)^{-1}, \tag{5}$$

where $\boldsymbol{w}_{v,j}$ is the weight for the vth particle in the jth iteration and $\mathcal{N}(\widehat{\boldsymbol{\theta}}^{ABC}_{k,j-1}|\widehat{\boldsymbol{\theta}}^{ABC}_{v,j},\boldsymbol{\Sigma}_{j-1})$ is the probability of $\widehat{\boldsymbol{\theta}}^{ABC}_{k,j-1}$ given the normal distribution with mean $\widehat{\boldsymbol{\theta}}^{ABC}_{v,j}$ and covariance $\boldsymbol{\Sigma}_{j-1}$, where $\boldsymbol{\Sigma}_j = 2\mathrm{Cov}(\widehat{\boldsymbol{\theta}}^{ABC}_{1:N_p,j})$. Furthermore, the chosen particle ($\boldsymbol{\theta}^{*}$) is perturbed to create a proposal particle ($\boldsymbol{\theta}^{**}$) using a transition kernel set as $\mathcal{N}(0,\boldsymbol{\Sigma}_j)$ Beaumont et al. (2009). The model is used to simulate data using $\boldsymbol{\theta}^{**}$ to calculate an associated proposal error (ϵ^{**}) according to Eq. 4. If ϵ^{**} is lower than a set threshold (T_j), $\boldsymbol{\theta}^{**}$ is accepted and used in the next iteration of the algorithm; if not, a new particle is chosen and perpetuated to create a new proposal particle. Note that the boundaries for the ABC PMC algorithm are more inclusive compared to the GA to accommodate the full width of the estimated posteriors, as shown in Table 1. A proposal particle outside the boundaries is always rejected. The next iteration starts when N_p new proposal particles have been accepted, and $\boldsymbol{w}_{v,j}$, T_j, and $\boldsymbol{\Sigma}_j$ are then updated. The threshold changes based on the results from the GA; where $T_1 = \widehat{\boldsymbol{\theta}}^{GA}_{10}(pat,s)$, $T_2 = \widehat{\boldsymbol{\theta}}^{GA}_{8}(pat,s)$, $T_3 = \widehat{\boldsymbol{\theta}}^{GA}_{5}(pat,s)$, $T_4 = \widehat{\boldsymbol{\theta}}^{GA}_{3}(pat,s)$, and $T_{5:8} = \widehat{\boldsymbol{\theta}}^{GA}_{1}(pat,s)$. Hence, after the eighth iteration, the ϵ for all particles is lower than the ϵ for the fittest parameter vectors found by the GA. Thus, the final population is assumed to be N_p samples from $p(\boldsymbol{\theta}|\boldsymbol{RR}(pat,s),\widehat{\lambda}(pat,s))$.

The hyper-parameters for the ABC PMC algorithm were decided based on empirical tests on simulated data in combination with theoretical indications. The ABC PMC algorithm should ideally be initialized with a particle cloud that is not too compact and not too wide, since both of those alternatives tend to increase the number of iterations until a steady state can be found for the particle cloud. Initial tests on simulated data (not shown) indicated that a good balance was achieved when the initialization was set to drawn samples from five normal distributions with mean values equal to the five fittest parameter vectors found by the GA. Moreover, the stepwise threshold was based on initial tests on simulated data, however, guided by the theoretical indication that the last iteration should yield parameter vectors with an ϵ lower than the ϵ for the fittest parameter vector found by the GA. The number of iterations was set to eight after simulations indicating that a steady state was reached after eight iterations, as shown in the Supplementary Material S2. Finally, the number of parameter vectors N_p was st to 100 based on available computational resources

2.4.3 Parameter reduction

The posterior estimate of the parameter vector $\boldsymbol{\theta}(pat,s)$ is obtained using the resulting N_p samples ($\widehat{\boldsymbol{\theta}}^{ABC}_{1:N_p,8}(pat,s)$) from the ABC PMC algorithm. Each $\widehat{\boldsymbol{\theta}}^{ABC}_{1:N_p,8}(pat,s)$ is utilized within the model together with the associated $\widehat{\lambda}(pat,s)$ to simulate a 10-min RR interval series. For each simulation, $R_i(n)$ and $D_i(n)$ are stored for each activation n in each pathway node i and used as the sample distribution of the RP and CD for the SP and the FP, respectively. The samples from these four distributions, denoted as $\widehat{\boldsymbol{\Phi}}(pat,s) = [\boldsymbol{R}^{FP}(pat,s),\boldsymbol{R}^{SP}(pat,s),\boldsymbol{D}^{FP}(pat,s),\boldsymbol{D}^{SP}(pat,s)]$, serves as a translation from the twelve model parameters $\widehat{\boldsymbol{\theta}}$ to four more interpretable AV node properties $\widehat{\boldsymbol{\Phi}}$, taking into account not only the model parameters but also the mean AFR associated with the current RR-segment.

To quantify these distributions, their corresponding empirical probability density functions are computed using the MATLAB function ksdensity (MATLAB R2022b) with default bandwidth. From the empirical probability density functions, the maxima are obtained, denoted $\widehat{\boldsymbol{\phi}}_{max}(pat,s) = [R^{FP}_{max}(pat,s),R^{SP}_{max}(pat,s),D^{FP}_{max}(pat,s),D^{SP}_{max}(pat,s)]$. In addition, the 5th percentile and the 95th percentile are obtained from $\widehat{\boldsymbol{\Phi}}(pat,s)$, denoted $\widehat{\boldsymbol{\phi}}_5(pat,s) = [R^{FP}_5(pat,s),R^{SP}_5(pat,s),D^{FP}_5(pat,s),D^{SP}_5(pat,s)]$, and $\widehat{\boldsymbol{\phi}}_{95}(pat,s) = [R^{FP}_{95}(pat,s),R^{SP}_{95}(pat,s),D^{FP}_{95}(pat,s),D^{SP}_{95}(pat,s)]$, respectively. Furthermore, the number of impulses traveling through the FP and SP (N_{FP} and N_{SP}, respectively) is stored, and the ratio is denoted as $SP_{ratio}(pat,s) = \frac{N_{SP}(pat,s)}{N_{FP}(pat,s)+N_{SP}(pat,s)}$.

The patient-specific diurnal variability (ΔDV) in the AV node properties is quantified by the average value of $\widehat{\boldsymbol{\phi}}_{max}$ during daytime (9:00 a.m. to 9:00 p.m.) divided by the average value of $\widehat{\boldsymbol{\phi}}_{max}$ during nighttime (2:00 a.m. to 6:00 a.m.). The definitions of day and night

At iteration $j = 1$, set the initial population
Set a counter $c = 1$
for $1 \le u \le 5$ **do**
 for $1 \le q \le \frac{N_p}{5}$ **do**
  Set $\hat{\boldsymbol{\theta}}_{c,1}^{ABC} \leftarrow \mathcal{N}(\hat{\boldsymbol{\theta}}_u^{GA}, \boldsymbol{\Sigma}_{init})$
  Set initial weights $\boldsymbol{w}_{c,1} \leftarrow \frac{1}{N_p}$
  Update counter $c = c + 1$
 end for
end for
Set the initial covariance for the transition kernel $\boldsymbol{\Sigma}_1 \leftarrow 2\text{Cov}(\hat{\boldsymbol{\theta}}_{1:N_p,1}^{ABC})$
At iteration $j > 1$
for $2 \le j \le 8$ **do**
 for $1 \le v \le N_p$ **do**
  Set $\epsilon^{**} = \inf$
  while $\epsilon^{**} > T_j$ **do**
   Sample one proposal particle from previous iteration $\boldsymbol{\theta}^{*} \sim \hat{\boldsymbol{\theta}}_{1:N_p,j-1}^{ABC}$ with probability $\boldsymbol{w}_{1:N_p,j-1}$
   Perturb $\boldsymbol{\theta}^{*}$ by sampling $\boldsymbol{\theta}^{**} \sim \mathcal{N}(\boldsymbol{\theta}^{*}, \boldsymbol{\Sigma}_{j-1})$
   Simulate data $\tilde{\boldsymbol{RR}}$ from $\boldsymbol{\theta}^{**}$: $\tilde{\boldsymbol{RR}} \sim$ Model$(\boldsymbol{\theta}^{**}, \tilde{\lambda})$
   Calculate ϵ^{**} from Eq. 4 using $\tilde{\boldsymbol{RR}}$ and $\boldsymbol{RR}$
  end while
  Set $\hat{\boldsymbol{\theta}}_{v,j}^{ABC} \leftarrow \boldsymbol{\theta}^{**}$
  Update the weight $\boldsymbol{w}_{v,j} \leftarrow \left(\sum_{k=1}^{N_p} \boldsymbol{w}_{k,j-1} P(\hat{\boldsymbol{\theta}}_{k,j-1}^{ABC} | N(\hat{\boldsymbol{\theta}}_{v,j}^{ABC}, \boldsymbol{\Sigma}_{j-1}))\right)^{-1}$ (Eq. 5)
 end for
  Update the covariance for the transition kernel $\boldsymbol{\Sigma}_j \leftarrow 2\text{Cov}(\hat{\boldsymbol{\theta}}_{1:N_p,j}^{ABC})$
end for

Algorithm 1. Calculate $p(\theta|\boldsymbol{RR}, \tilde{\lambda})$, given $\boldsymbol{RR}$, $\tilde{\lambda}$, the model $\tilde{\boldsymbol{RR}} \sim$ Model$(\theta, \tilde{\lambda})$, the threshold T_j, and the initial estimates $\hat{\theta}^{GA}$. The indication (pat,s) is omitted to avoid redundancy.

are designed to ensure that the patients are awake during the daytime and asleep during the nighttime. In addition, the patient-specific short-term variability in the AV node properties is quantified by the average Kolmogorov-Smirnov distance ($\overline{\Delta KS}$) between consecutive segments of $\widehat{\boldsymbol{\Phi}}$ during the full 24-h (8:00 a.m. to 8:00 a.m.). The Kolmogorov-Smirnov distance represents the maximal separation between the empirical cumulative distribution functions between consecutive segments Massey Jr (1951).

A significant difference between daytime and nighttime for the average $\hat{\boldsymbol{\phi}}_{max}$; the 90% credibility region, quantified by $\hat{\boldsymbol{\phi}}_5(pat,s) - \hat{\boldsymbol{\phi}}_{95}(pat,s)$; and the average Kolmogorov-Smirnov distance $\overline{\Delta KS}$ is evaluated using the Wilcoxon signed rank test, since all data did not follow a normal distribution according to the Shapiro-Wilk test ($p < 0.05$).

2.5 Prediction of treatment outcome

The predictive power of the estimates $\widehat{\boldsymbol{\Phi}}$, $\hat{\boldsymbol{\phi}}_5$, $\hat{\boldsymbol{\phi}}_{95}$, $\hat{\boldsymbol{\phi}}_{max}$, and SP_{ratio} in relation to ΔHR for the different rate control drugs is evaluated in three ways; by analyzing the correlation between the diurnal and short-time variability and ΔHR; by training a feature-based regression model on statistical properties of the trends to predict ΔHR; and by training a convolutional neural network on the trends to predict ΔHR.

To quantify the correlation between diurnal and short-term variability in the AV node properties and ΔHR after treatment with the four rate control drugs, Spearman's rank correlation is used, since the data do not follow a normal distribution according to the Shapiro-Wilk test ($p < 0.05$). Due to the exploratory nature of the study, no hypothesis test is performed and hence no correction of p-values is applied Perneger (1998); Althouse (2016).

Three different feature-based regression models (linear regression, random forest Breiman (2001), and k-nearest neighbor Cover and Hart (1967)) are trained on 66 statistical properties of the trends. These statistical properties are: the mean ± std of the four AV node properties $\hat{\boldsymbol{\phi}}_{max}$ during daytime (8 properties), during nighttime (8 properties), and the full 24-h (8 properties); the mean ± std of the 90% credibility region—calculated as the difference between $\hat{\boldsymbol{\phi}}_5$ and $\hat{\boldsymbol{\phi}}_{95}$—during daytime (8 properties), nighttime (8 properties), and the full 24-h (8 properties); the mean ± std of the SP_{ratio} during daytime (2 properties), nighttime (2 properties), and the full 24-h (2 properties); ΔDV in the four AV node properties (4 properties); the short-term variability in the four AV node properties (4 properties); as well as the age, gender, weight, and height of the patient.

Deep learning approaches have achieved the current state-of-the-art performance for time-series classification and regression Ismail Fawaz et al. (2019). Hence, the prediction of ΔHR for the different rate control drug is evaluated using the time series for $\hat{\boldsymbol{\phi}}_5$, $\hat{\boldsymbol{\phi}}_{95}$, $\hat{\boldsymbol{\phi}}_{max}$, SP_{ratio}, AFR, and the RR interval series as an input to three convolutional neural networks with different architectures, based on only fully connected layers Wang et al. (2017), the ResNet architecture Wang et al. (2017), and the Inception architecture Ismail Fawaz et al. (2020), respectively. To incorporate the age, gender, weight, and height of the patients, the last fully connected layer of the networks is modified to also include these properties as input neurons. The networks were trained using the tsai library Oguiza (2022), with the Adam solver Kingma and Ba (2014) and the Huber loss Huber (1992). Leave-one-out cross-validation is used, so that the network is trained on data from all but one patient and tested on the left-out patient. The average mean square error (MSE) of the predicted and true ΔHR for the whole population is calculated and compared between approaches.

3 Results

As described in Section 2.1, this study is based on a population of 60 patients. However, due to excessive noise, some patients are excluded from analysis, as described in Section 2.2, resulting in a total of 51 patients. The paired significant tests described in Section 2.4.3 are performed on all patients with data for both daytime and nighttime, resulting in a total of 47 patients. In addition, excessive noise in the ECG during treatment with the four rate control drugs leads to missing values for ΔHR for some patients. Thus, of the remaining 51 patients at baseline, two lack data for verapamil, three lack data for diltiazem, two lack data for metoprolol, none lack data for carvedilol, and one lacks data for both verapamil

and metoprolol. The mean ± standard deviation of ΔHR in the population are 19% ± 23% for verapamil; 24% ± 18% for diltiazem, 17% ± 18% for metoprolol; and 11% ± 6% for carvedilol.

The computation of the $\widehat{\Phi}(pat,s)$ is divided into three parts; the GA, the ABC PMC algorithm, and the parameter reduction. All computations were performed on a desktop computer with an AMD Ryzen 9 5900X CPU (using the twelve cores in parallel). Using this setup, the median computation time per patient was 1 h 20 min for the GA, 12 h 30 min for the ABC PMC algorithm, and 6 min for the parameter reduction.

In addition to providing a measure of uncertainty, using the ABC PMC algorithm also reduces ϵ compared to only using the GA. This refinement is quantified by the percentual reduction in ϵ, calculated as the average $\frac{\epsilon_1^{GA}(pat,s)-\epsilon_1^{ABC}(pat,s)}{\epsilon_1^{GA}(pat,s)}100$ for each patient and segment, where $\epsilon_1^{GA}(pat,s)$ and $\epsilon_1^{ABC}(pat,s)$ represent the lowest error value found for the GA and ABC PMC algorithm, respectively. The average refinement ± standard deviation when using the ABC PMC algorithm was 9.14% ± 3.01%. Moreover, a simulation study was performed to validate the proposed model and framework using ground truth data. These results are found in the Supplementary Material S1.

3.1 Parameter trends

Figures 3, 4 show 24-h trends in estimated RP, CD, and SP_{ratio} for two patients, denoted patient A (Figure 3) and patient B (Figure 4). Looking at the two top panels of the figures, FP is blue and SP is red. The dots represent the most probable parameter set per segment, $\widehat{\phi}_{max}(pat,s)$, and colored fields represent the 90% credibility region around the dots, quantified by $\widehat{\phi}_5(pat,s)$, and $\widehat{\phi}_{95}(pat,s)$. Comparing the figures, patient A (Figure 3) displays a lower short-term variability, taking values of $\overline{\Delta KS} = [0.27, 0.19, 0.24, 0.33]$ for R^{FP}, R^{SP}, D^{FP}, and D^{SP}, respectively. Conversely, patient B (Figure 4) displays a larger variability, with $\overline{\Delta KS} = [0.41, 0.55, 0.40, 0.40]$ for R^{FP}, R^{SP}, D^{FP}, and D^{SP}, respectively. Moving on to the bottom panels of Figures 3, 4, it is evident that conduction mainly occurs through the SP in both patients, as indicated by an SP_{ratio} over 0.5, resulting in a wider credibility region in the R^{FP} compared to the R^{SP}. However, for patient B, there are segments where the FP is more prevalent, e.g., between 5 p.m. and 6 p.m.. In these segments, the RP and CD have a very low variability indicating a stationary behavior of the AV node. A notable shift in RP occurs at 8 a.m. for patient A, probably as a response to waking up from sleep, resulting in a clear change in autonomic regulation. No notable diurnal variability for R^{FP}, R^{SP}, and D^{FP} could be seen for patient A, with a slight difference in D^{SP} ($\Delta DV = [0.80, 0.81, 0.99, 1.39]$). For patient B, only D^{FP} showed a notable diurnal variability ($\Delta DV = [0.81, 0.92, 2.60, 1.19]$).

Similar observations can be made for the whole population, as displayed in Table 2, which includes the mean and standard deviation of $\widehat{\phi}_{max}(pat,s)$, the 95% credibility region, and $\overline{\Delta KS}$, during daytime, nighttime, and during 24 h, as well as ΔDV, for the RP and CD in the FP and the SP for all patients. For convenience, the total CD, calculated by multiplying the CD for one node by ten, is listed. Significant difference between daytime and nighttime for $\widehat{\phi}_{max}$, the 90% credibility region, and $\overline{\Delta KS}$ is marked with *, †, and ‡ in Table 2, respectively. From Table 2, it is evident that the RP on average is higher and the CD is lower during nighttime compared to daytime, probably linked to the lower heart rate during sleep and/or circadian autonomic variations. This difference was significant ($p < 0.001$) for R^{FP}, R^{SP}, and D^{SP}, as marked with * in Table 2. Figure 5 illustrates the population average trends of $\widehat{\phi}_{max}(pat,s)$, $\widehat{\phi}_5(pat,s)$, and $\widehat{\phi}_{95}(pat,s)$. To reduce the influence of outliers, only segments containing data from over 20% of the population are shown, resulting in a varying number of patients per plotted segment with a minimum of ten patients per segment and a median of 43 patients per segment. A distinct separation between RP and CD of the two pathways exists, indicating different functionality. Additionally, the credibility region for the R^{FP} is larger compared to the R^{SP}. Moreover, the credibility region for D^{FP}, in proportion to its mean value, is larger than that of D^{SP}. The differences in credibility regions between FP and SP reflect the SP_{ratio}, which is 0.78 ± 0.11 (mean ± std) during the day, 0.79 ± 0.12 during the night, and 0.78 ± 0.10 during the full 24-h, indicating that the SP is dominant on average.

3.2 Prediction of treatment outcome

Spearman's rank correlation between the patient-specific ΔDV, as described in Section 2.5, and ΔHR showed no clear correlation ($p < 0.05$) for any combination of drug and AV node property. Hence, no relationship between diurnal variability and drug outcome was found.

The Spearman correlation between the patient-specific short-time variability, quantified by $\overline{\Delta KS}$, and ΔHR showed no clear correlation ($p < 0.05$) for the RP and CD in the SP. A moderate correlation was however found between $\overline{\Delta KS}$ and ΔHR for R^{FP} in the β-blocker metoprolol ($\rho = 0.47, p = 0.0011$) and for D^{FP} in metoprolol ($\rho = 0.35, p = 0.017$). Figure 6 shows the individual $\overline{\Delta KS}$ plotted against ΔHR and their linear relation for all four drugs, with the left panel showing R^{FP} and the right panel showing D^{FP}. Interestingly, a similar relation between $\overline{\Delta KS}$, and ΔHR is not present in the other β-blocker carvedilol.

The ability to predict ΔHR using machine learning approaches is evaluated by the average MSE between the predicted and true ΔHR for the four drugs using the leave-one-out validation method. The average MSE is benchmarked against the population variance of ΔHR for the four drugs. Hence, if the average MSE is larger than the population variance at 0.0071%, the population mean yields a more accurate predictor. Using the feature-based regression models, as described in Section 2.5, resulted in an average MSE of 0.0073% for the linear regression, an average MSE of 0.0074% for the random forest, and an average MSE of 0.074% for the k-nearest neighbor. In addition, using the convolutional neural network resulted in an average MSE of 0.0073% for the fully connected architecture, an average MSE of 0.0079% for the ResNet architecture, and an average MSE of 0.0074% for the Inception architecture. Overall, all the machine-learning approaches resulted in an average MSE higher than 0.0071% and thus in a poor fit to new-seen data.

4 Discussion

A mathematical model with an associated framework for patient-specific estimation and proper uncertainty quantification

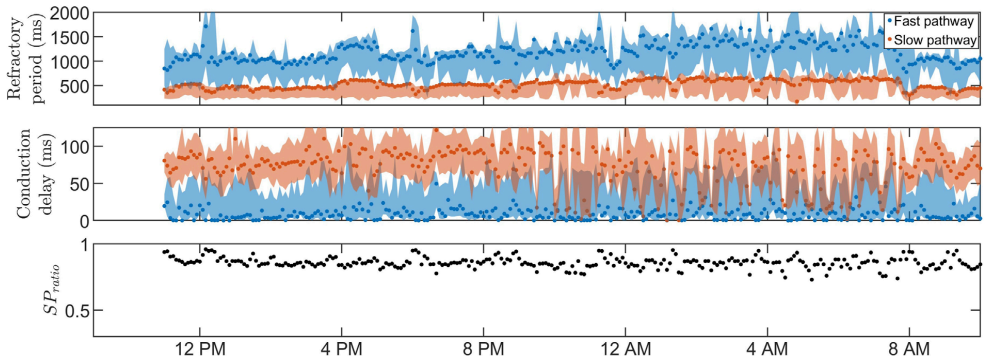

FIGURE 3
The estimated RP (top) and CD (middle) for $\hat{\phi}_{max}(pat,s)$ (dotted) as well as $\hat{\phi}_{5}(pat,s)$ and $\hat{\phi}_{95}(pat,s)$ (filled) for the FP (blue) and SP (red), as well as the SP ratio (bottom) are shown for patient A, marked with a black circle in Figure 6.

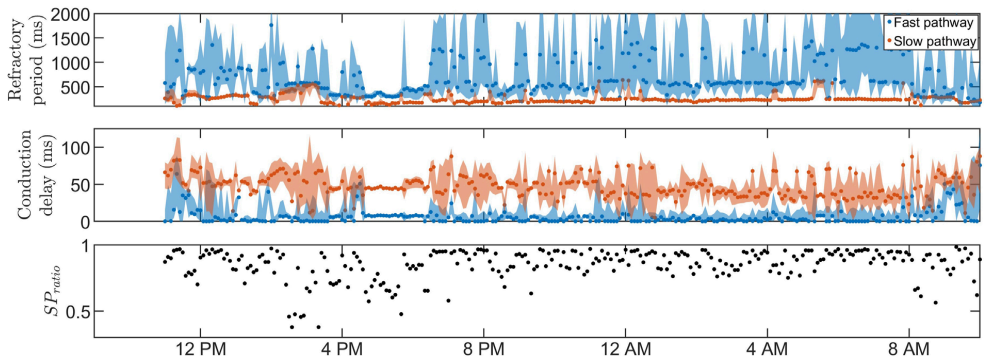

FIGURE 4
The estimated RP (top) and CD (middle) for $\hat{\phi}_{max}(pat,s)$ (dotted) as well as $\hat{\phi}_{5}(pat,s)$ and $\hat{\phi}_{95}(pat,s)$ (filled) for the FP (blue) and SP (red), together with the SP ratio (bottom) are shown for patient B, marked with a red circle in Figure 6.

of the RP and CD in the FP and SP of the AV node using only non-invasive data has been proposed.

Individual estimation of trends and variability in AV node properties using non-invasive data has the potential to increase the patient-specific understanding of the AV node during AF, which in turn can be used to enhance informatics approaches for the next-generation of personalized medicine. The two most dominant properties of the AV node, the RP and CD, together with the ratio of impulses conducted through the different pathways, have the potential to increase the understanding of the AV node and its function during AF.

Due to the physiological differences between the effect of β-blockers and calcium channel blockers, where β-blockers reduce the effect of the sympathetic nervous system, we hypothesized that β-blockers could exhibit an increased effect when variations in the AV node properties are prominent since this would indicate a larger influence of the autonomic nervous system. The population-averaged trends (Figure 5; Table 2) show a significant increase in RP for both pathways and a significant decrease in CD for the SP and a non-significant decrease in CD for the FP during nighttime compared to daytime, suggesting that the decreased sympathetic activity during nighttime affects the RP and CD. The PR interval during sinus rhythm can be used as a measure of the CD in the FP for healthy subjects and is known to have a significant increase during nighttime compared to daytime Dilaveris et al. (2001). Interestingly, no corresponding changes in CD for the FP could be observed in our presented analysis, possibly due to the differences in AV node function between AF and sinus rhythm. However, no correlation was found between diurnal variations in AV properties and reduction in heart rate during treatment with β-blockers.

Interestingly, a potential association between the short-time variability and the treatment outcome with metoprolol was

TABLE 2 The mean ± std of the average $\hat{\bar{\phi}}_{max}$, the 95% credibility region, and $\overline{\Delta KS}$ for all patients during daytime, nighttime, and 24-h average together with ΔDV. For convenience, the total CD, calculated by multiplying the CD for one node by ten, is listed. A significant difference (p <0.001) between the daytime and nighttime estimate is marked by * for $\hat{\bar{\phi}}_{max}$, by † for the 90% credibility region $\bar{\hat{\phi}}_{95} - \bar{\hat{\phi}}_{5}$, and by ‡ for $\overline{\Delta KS}$. The indication (pat, s) is omitted to avoid redundancy.

	$R^{FP*‡}$	$R^{SP*†‡}$	$10D^{FP‡}$	$10D^{SP*†}$
24-h $\bar{\hat{\phi}}_{max}$ (ms)	934 ± 203	399 ± 95	76.9 ± 47.6	546 ± 126
Daytime $\bar{\hat{\phi}}_{max}$ (ms)	839 ± 205	356 ± 94	85 ± 64.6	572 ± 139
Nighttime $\bar{\hat{\phi}}_{max}$ (ms)	1,119 ± 294	481 ± 152	62.1 ± 52.8	484 ± 160
24-h $\bar{\hat{\phi}}_{95} - \bar{\hat{\phi}}_{5}$ (ms)	687 ± 232	217 ± 114	304.1 ± 110.7	447 ± 103
Daytime $\bar{\hat{\phi}}_{95} - \bar{\hat{\phi}}_{5}$ (ms)	671 ± 261	179 ± 103	299.4 ± 123.9	427 ± 94
Nighttime $\bar{\hat{\phi}}_{95} - \bar{\hat{\phi}}_{5}$ (ms)	738 ± 290	291 ± 185	315.5 ± 153.3	477 ± 169
24-h $\overline{\Delta KS}$	0.347 ± 0.057	0.319 ± 0.136	0.376 ± 0.055	0.36 ± 0.07
Daytime $\overline{\Delta KS}$	0.368 ± 0.069	0.352 ± 0.169	0.393 ± 0.061	0.351 ± 0.089
Nighttime $\overline{\Delta KS}$	0.309 ± 0.083	0.253 ± 0.133	0.342 ± 0.075	0.38 ± 0.082
ΔDV	0.77 ± 0.18	0.78 ± 0.27	2.58 ± 3.72	1.29 ± 0.47

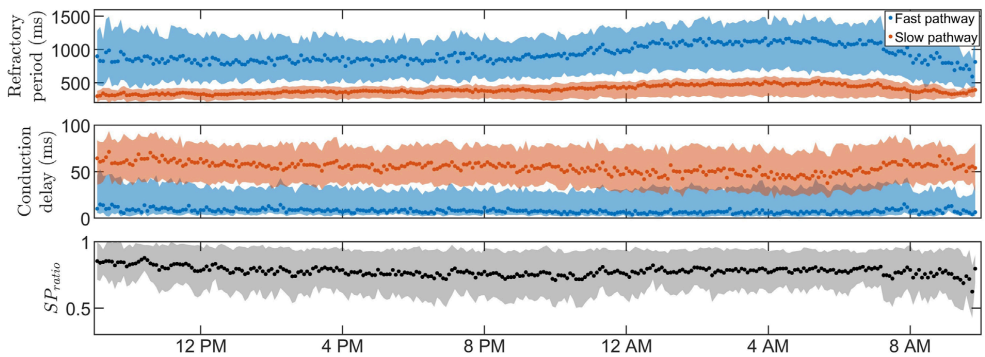

FIGURE 5
The average RP (top) and CD (middle) for $\hat{\phi}_{max}(pat,s)$ (dotted) as well as $\hat{\phi}_{5}(pat,s)$ and $\hat{\phi}_{95}(pat,s)$ (filled) for the FP (blue) and SP (red), together with the mean (black, dotted) and standard deviation (black, filled) of the SP ratio (bottom).

found. The findings depicted in Figure 6 demonstrate a moderate correlation between $\overline{\Delta KS}$ and the change in heart rate (ΔHR) in the RP and CD for the FP for metoprolol, but not for any other drugs or for the SP. The lack of correlation between ΔHR after treatment with carvedilol (also a β-blocker) and $\overline{\Delta KS}$ could potentially be attributed to its modest overall effect observed in the RATAF study, likely stemming from its rapid elimination as acknowledged in Shapiro (2013). Moreover, the FP and SP are known to have distinct electrophysiological behaviors, hence a different response to drugs between the pathways is to be expected Greener et al. (2011); Nikolaidou et al. (2012); George et al. (2017). For example, the β-blocker esmolol has been shown to have a lower effect on the anterograde RP of the SP compared to the FP Philippon et al. (1994). This lower effect on the RP for beta-blockers could possibly explain the lack of correlation seen between the SP estimate and treatment outcome. In general, the mechanisms underlying AV nodal function are debated, and the physiological differences between the pathways that are relevant for the effects of different drug types are not fully known Billette and Tadros (2019). To confirm the association between short-time variability in the RP and CD in the FP and treatment outcome in response to metoprolol, additional studies are needed.

It is possible that predictivity could be improved beyond this association between the short-term variability and the treatment outcome by including additional information from the AV node model. As a tool for this, machine learning techniques are of interest Adam et al. (2020). Hence, three featured-based regression models were used to test if features from the AV node parameter trends

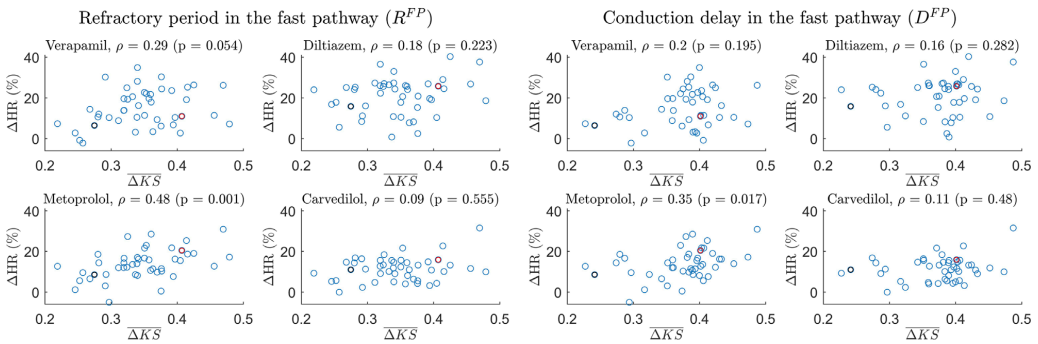

FIGURE 6
Scatter plot of the 24-h ΔHR and $\overline{\Delta KS}$ for the R^{FP} (left) and D^{FP} (right) for the four drugs with ρ indicating the Spearman correlation coefficient, with patient A (as shown in Figure 3) marked with black and patient B (as shown in Figure 4) marked with red.

could predict ΔHR for the different rate control drugs. Moreover, three different architectures of a convolutional neural network were also tested, with the AV node parameter time series as an input, since convolutional neural network have the current state-of-the-art performance for time-series classification and regression Ismail Fawaz et al. (2019). In addition to the estimated AV node parameters, information including the age, gender, weight, and height of the patients was included in an attempt to improve the prediction, since these are immediately available when applying the model in a clinical setting. With a resulting average MSE higher than the variance of ΔHR for the population, it appears impossible to predict ΔHR with any certainty in the present data set. Either there is not enough information relevant for predicting the heart rate reduction after drug treatment in the AV node property trends—possibly due to the 10-min resolution, limiting the information about autonomic regulation—or the data set size of 51 patients is too low given the inter-individual variability present in the measurements.

Prior iterations of the model and framework focused on estimating the model parameter trends rather than the patient-specific property trends of the AV node Karlsson et al. (2022). This approach imposed limitations on the interpretability of the results, since the interpretation of the model parameters in terms of common cardiology terminology such as RP and CD is not straightforward. In contrast, the current work introduces a novel methodology that enables the estimation of the RP and CD for each ECG segment individually, facilitating a more comprehensible and interpretable analysis. The ability to derive such estimates is vital as it allows for effective communication of the analysis results. Furthermore, this advancement in methodology opens up new avenues for gaining a deeper understanding of the AV node and its diurnal and short-term variations.

The estimation of the posterior by obtaining a range of plausible values, as opposed to relying on a point estimate of the AV node properties, offers notable advantages. For example, the credibility region for R^{FP} in Figure 4 is very broad during most segments at nighttime, reflecting a high uncertainty. In scenarios where the extent of the uncertainty is unknown, these uncertain estimates have the potential to influence decision-making processes or further analysis of the trends. As a result, the usefulness and reliability of these estimates may be decreased, emphasizing the need for an estimation of the uncertainty. In our previous work, a GA was used to estimate time variations in the network model parameters during 24 h, with a version of Sobol's method to quantify the uncertainty in the parameter estimates Karlsson et al. (2022). The uncertainty could be quantified using different methods, such as performing multiple runs of the GA and analyzing the distribution of the resulting estimates or by using bootstrapping to resample the RR interval and run the GA on each resampled dataset. However, the uncertainty estimation resulting from these types of methods, including the version of Sobol's method previously used, will not be interpretable as probabilities, limiting the reliability of the resulting uncertainty estimates. To produce uncertainty estimates that are interpretable as probabilities, apart from using an ABC approach, the main alternative would be using a Bayesian surrogate model such as the Gaussian process Sudret et al. (2017). However, initial tests found it to be a slower alternative. The ABC approach is well suited for this work since the previously designed error function in Eq. 4 can be used directly as a distance metric, which is often one of the more cumbersome steps in the ABC approach. In addition, the ABC approach has in recent years been used for the personalization of the electrophysiological properties in cardiac models Camps et al. (2021). Although ABC approaches are generally computationally expensive Turner and Van Zandt (2012), starting in a promising area of the model parameter space, derived from the GA results, reduced the computation time by a factor of around 50 (data not shown). The GA was also used to decide on a reasonable threshold level for the ABC PMC algorithm, which is not straightforward since imperfections in the model make certain RR series more challenging to replicate than others, resulting in a higher average ϵ. Hence, an ϵ value corresponding to a good fit for one RR interval series could correspond to a poor fit for another, making thresholds very data-dependent. Using the GA to find the threshold levels ensures a reasonable threshold level specified for each data segment.

The main advantage of the ABC PMC algorithm is that it provides an estimate of the posterior. Nevertheless, it also has the

ability to reduce the ϵ value, yielding a closer fit to observed data. The improvement in parameter estimates when combining the GA with the ABC PMC algorithm compared to solely using the GA has been evaluated on simulated data with known model parameters, as shown in the Supplementary Material S1. From this, no statistical difference could be found between the GA and the ABC PMC algorithm for ten out of twelve model parameters when measuring the distance to the known model parameters. However, the best particle found by the ABC PMC algorithm had a significantly lower average ϵ value compared to the best parameter vector found by the GA, indicating a better fit to the simulated data. Additionally, in the data analyzed in this study, the best particle for each segment found by the ABC PMC algorithm had on average an ϵ value 9.14% lower compared to the best parameter vector found by the GA, confirming an overall improvement.

4.1 Study limitations and future perspectives

The AV node model accounts for most properties of importance during AF, such as single and dual pathway physiology, rate-dependent changes in AV conduction properties, and is able to simulate retrograde conduction Billette and Tadros (2019). However, it does not include ventricular escape rhythm, and is unable to replicate the behavior of some rare AV node structures, such as multiple slow pathways. Nevertheless, these simplifications are essential to develop a model with a manageable number of parameters, reducing the computational requirements and thus enabling parameter estimation from non-invasive data using tools such as the GA and the ABC PMC algorithm. Moreover, the model does not explicitly account for AV nodal fatigue. However, any effects of fatigue in the analyzed data sets should be indirectly accounted for in the estimated model parameters.

In this work, we generated the AA interval series used as an input to the model using a Poisson process. We are aware that more detailed representations, notably the Pearson type 4 distribution, can be used to describe atrial impulses during AF Climent et al. (2011b); Plappert et al. (2022). However, for the purposes of the present study, the more simplistic Poisson process was preferred due to its single-parameter description, facilitating parameter estimation, and since it has previously been shown to generate realistic RR-interval series together with the employed AV-node model Karlsson et al. (2021).

The estimated RP and CD have not been validated against intracardiac measurements, since obtaining such measurements during AF—if at all possible—would be very difficult and time-consuming. The average RP and CD for the two pathways can however be compared with invasive electrophysiological measurements of the AV node from two patients with paroxysmal supraventricular tachycardia and evidence of dual AV nodal conduction found in the literature Denes et al. (1973). The two patients had an RP in the FP of 820 ms and 495 ms; an RP in the SP of 540 ms and 414 ms; a CD in the FP of 125 ms and 150 ms; and a CD in the SP of 500 ms and 300 ms. Comparing these values to the daytime estimates seen in Table 2, it is evident that the measured values for the RP and CD in both pathways are within the range of our estimated values. It should be noted that the comparison between AV node properties during paroxysmal and permanent AF is non-trivial, since permanent AF may involve remodeling of the AV node, as shown in animal models Zhang and Mazgalev (2012). Adding to this non-triviality is the fact that the measured functional RP values come from an S1-S2 protocol during sinus rhythm. The functional RP is the smallest AA interval preceding a conducted impulse. It is however still dependent on the previous pacing frequency, which is not well-defined during AF. Nevertheless, since AF leads to high frequencies, the RP should be reasonably close to the functional RP.

In this study, short-time variability was estimated as the difference between adjacent 10-min intervals. Given a constant budget of CPU time, there exists a trade-off between temporal resolution and uncertainty in the estimates, since shorter segments result in an increased number of segments, and more segments result in increased computational demands. Thus, the number of particles would need to decrease, resulting in a poorer estimate of the posterior. Because of this, 10-min segments were chosen to balance the temporal resolution and the quality of the estimates, while keeping the computation time at reasonable levels for practical use. However, the results from the analysis suggest a correlation between short-term variability in the AV node properties and treatment outcome, hinting that increasing the time resolution has the potential to increase the information extracted by the model and framework, which could improve the results. Limiting the short-time variability to 10 minutes also limits the information about the autonomic nervous system—which is known to operate on a higher resolution—to a 10-min resolution. Furthermore, to extract even more information about the impact of the autonomic nervous system on the AV node, an extension of the model has been proposed in Plappert et al. (2022). A similar framework to the one presented in this work could be employed for that model to estimate model parameters and simulate the RP and CD. This could further refine the estimates and thus the information about the AV node.

Moreover, analyzing the RP and CD trends for all the patients, a high inter-individual variability with a wide range of diurnal and short-time variability could be seen, likely due to the inherent individual differences. This, in combination with the relatively low number of patients (51), indicates that the results in this paper should be verified in a larger study.

5 Conclusion

We have proposed a novel framework for estimating patient-specific 24-h trends of the RP and CD in the FP and SP of the AV node by mapping estimated model parameters. These estimates include the full posterior of the RP and CD and could be estimated using only non-invasive data. Additionally, a correlation between short-term variability in both the RP and CD for the FP and drug-induced changes to the heart rate was found. The individual estimates of AV node properties offer patient-specific trends in RP and CD, which may have the potential to assist in treatment selection.

Data availability statement

The data analyzed in this study is subject to the following licenses/restrictions: The estimated AV node properties supporting the conclusion for this article will be available from MK upon request. The measured data are owned by Vestre Viken Hospital Trust, and requests for access can be made to SU. The code for the model together with a user example can be found at https://github.com/FraunhoferChalmersCentre/AV-node-model. Requests to access these datasets should be directed to mattias.karlsson@fcc.chalmers.se, sara.ulimoen@gmail.com.

Ethics statement

The studies involving humans were approved by the Regional ethics committee and the Norwegian Medicines Agency. The studies were conducted in accordance with the local legislation and institutional requirements. The participants provided their written informed consent to participate in this study.

Author contributions

MK: Conceptualization, Data curation, Formal Analysis, Investigation, Methodology, Software, Validation, Visualization, Writing–original draft, Writing–review and editing. PP: Formal Analysis, Validation, Writing–review and editing. FS: Conceptualization, Formal Analysis, Investigation, Methodology, Supervision, Validation, Writing–review and editing, Funding acquisition, Project administration, Resources. MW: Conceptualization, Formal Analysis, Investigation, Methodology, Supervision, Validation, Writing–review and editing, Funding acquisition, Project administration, Resources.

Funding

The author(s) declare financial support was received for the research, authorship, and/or publication of this article. This work was supported by the Swedish Foundation for Strategic Research (Grant FID18-0023), the Swedish Research Council (Grant VR 2019-04272), and the Crafoord Foundation (Grant 20200605).

Conflict of interest

The authors declare that the research was conducted in the absence of any commercial or financial relationships that could be construed as a potential conflict of interest.

Publisher's note

All claims expressed in this article are solely those of the authors and do not necessarily represent those of their affiliated organizations, or those of the publisher, the editors and the reviewers. Any product that may be evaluated in this article, or claim that may be made by its manufacturer, is not guaranteed or endorsed by the publisher.

Supplementary material

The Supplementary Material for this article can be found online at: https://www.frontiersin.org/articles/10.3389/fphys.2023.1287365/full#supplementary-material

References

Adam, G., Rampášek, L., Safikhani, Z., Smirnov, P., Haibe-Kains, B., and Goldenberg, A. (2020). Machine learning approaches to drug response prediction: challenges and recent progress. *NPJ Precis. Oncol.* 4, 19. doi:10.1038/s41698-020-0122-1

Althouse, A. D. (2016). Adjust for multiple comparisons? it's not that simple. *Ann. Thorac. Surg.* 101, 1644–1645. doi:10.1016/j.athoracsur.2015.11.024

Andrew, N. E., Thrift, A. G., and Cadilhac, D. A. (2013). The prevalence, impact and economic implications of atrial fibrillation in stroke: what progress has been made? *Neuroepidemiology* 40, 227–239. doi:10.1159/000343667

Beaumont, M. A., Cornuet, J. M., Marin, J. M., and Robert, C. P. (2009). Adaptive approximate bayesian computation. *Biometrika* 96, 983–990. doi:10.1093/biomet/asp052

Benjamin, E. J., Muntner, P., Alonso, A., Bittencourt, M. S., Callaway, C. W., Carson, A. P., et al. (2019). Heart disease and stroke statistics-2019 update a report from the american heart association. *Circulation* 139, e56–e528. doi:10.1161/CIR.0000000000000659

Billette, J., and Nattel, S. (1994). Dynamic behavior of the atrioventricular node: a functional model of interaction between recovery, facilitation, and fatigue. *J. Cardiovasc. Electrophysiol.* 5, 90–102. doi:10.1111/j.1540-8167.1994.tb01117.x

Billette, J., and Tadros, R. (2019). An integrated overview of av node physiology. *Pacing Clin. Electrophysiol.* 42, 805–820. doi:10.1111/pace.13734

Breiman, L. (2001). Random forests. *Mach. Learn.* 45, 5–32. doi:10.1023/a:1010933404324

Camps, J., Lawson, B., Drovandi, C., Minchole, A., Wang, Z. J., Grau, V., et al. (2021). Inference of ventricular activation properties from non-invasive electrocardiography. *Med. Image Anal.* 73, 102143. doi:10.1016/j.media.2021.102143

Climent, A. M., Atienza, F., Millet, J., and Guillem, M. S. (2011a). Generation of realistic atrial to atrial interval series during atrial fibrillation. *Med. Biol. Eng. Comput.* 49, 1261–1268. doi:10.1007/s11517-011-0823-2

Climent, A. M., Guillem, M. S., Zhang, Y., Millet, J., and Mazgalev, T. N. (2011b). Functional mathematical model of dual pathway AV nodal conduction. *Am. J. Physiol. Heart Circ. Physiol.* 300, H1393–H1401. doi:10.1152/ajpheart.01175.2010

Corino, V. D., Sandberg, F., Lombardi, F., Mainardi, L. T., and Sörnmo, L. (2013). Atrioventricular nodal function during atrial fibrillation: model building and robust estimation. *Biomed. Signal Process. Control* 8, 1017–1025. doi:10.1016/j.bspc.2012.10.006

Corino, V. D., Sandberg, F., Mainardi, L. T., and Sornmo, L. (2011). An atrioventricular node model for analysis of the ventricular response during atrial fibrillation. *IEEE Trans. Biomed. Eng.* 58, 3386–3395. doi:10.1109/TBME.2011.2166262

Cover, T., and Hart, P. (1967). Nearest neighbor pattern classification. *IEEE Trans. Inf. theory* 13, 21–27. doi:10.1109/tit.1967.1053964

Denes, P., Wu, D., Dhingra, R. C., Chuquimia, R., and Rosen, K. M. (1973). Demonstration of dual av nodal pathways in patients with paroxysmal supraventricular tachycardia. *Circulation* 48, 549–555. doi:10.1161/01.cir.48.3.549

Di Carlo, A., Bellino, L., Consoli, D., Mori, F., Zaninelli, A., Baldereschi, M., et al. (2019). Prevalence of atrial fibrillation in the Italian elderly population and projections from 2020 to 2060 for Italy and the European Union: the fai project. *EP Eur.* 21, 1468–1475. doi:10.1093/europace/euz141

Dilaveris, P. E., Färbom, P., Batchvarov, V., Ghuran, A., and Malik, M. (2001). Circadian behavior of p-wave duration, p-wave area, and pr interval in healthy subjects. *Ann. noninvasive Electrocardiol.* 6, 92–97. doi:10.1111/j.1542-474x.2001.tb00092.x

Dorian, P. (2005). Antiarrhythmic action ofβ-blockers: potential mechanisms. *J. Cardiovasc. Pharmacol. Ther.* 10, S15–S22. doi:10.1177/10742484050100i403

Eisenberg, M. J., Brox, A., and Bestawros, A. N. (2004). Calcium channel blockers: an update. *Am. J. Med.* 116, 35–43. doi:10.1016/j.amjmed.2003.08.027

George, S. A., Faye, N. R., Murillo-Berlioz, A., Lee, K. B., Trachiotis, G. D., and Efimov, I. R. (2017). At the atrioventricular crossroads: dual pathway electrophysiology in the atrioventricular node and its underlying heterogeneities. *Arrhythmia Electrophysiol. Rev.* 6, 179–185. doi:10.15420/aer.2017.30.1

Greener, I., Monfredi, O., Inada, S., Chandler, N., Tellez, J., Atkinson, A., et al. (2011). Molecular architecture of the human specialised atrioventricular conduction axis. *J. Mol. Cell. Cardiol.* 50, 642–651. doi:10.1016/j.yjmcc.2010.12.017

Henriksson, M., Corino, V. D. A., Sornmo, L., and Sandberg, F. (2015). A statistical atrioventricular node model accounting for pathway switching during atrial fibrillation. *IEEE Trans. Biomed. Eng.* 63, 1842–1849. doi:10.1109/TBME.2015.2503562

Hindricks, G., Potpara, T., Dagres, N., Arbelo, E., Bax, J. J., Blomström-Lundqvist, C., et al. (2020). 2020 ESC guidelines for the diagnosis and management of atrial fibrillation developed in collaboration with the european association of cardio-thoracic surgery (EACTS). *Am. J. Physiol. Heart Circ. Physiol.* 1–38. doi:10.1093/eurheartj/ehaa612

Huber, P. J. (1992). Robust estimation of a location parameter. *Break. statistics Methodol. distribution*, 35. 492–518. Available at: https://www.jstor.org/stable/2238020.

Inada, S., Hancox, J., Zhang, H., and Boyett, M. (2009). One-dimensional mathematical model of the atrioventricular node including atrio-nodal, nodal, and nodal-his cells. *Biophysical J.* 97, 2117–2127. doi:10.1016/j.bpj.2009.06.056

Ismail Fawaz, H., Forestier, G., Weber, J., Idoumghar, L., and Muller, P.-A. (2019). Deep learning for time series classification: a review. *Data Min. Knowl. Discov.* 33, 917–963. doi:10.1007/s10618-019-00619-1

Ismail Fawaz, H., Lucas, B., Forestier, G., Pelletier, C., Schmidt, D. F., Weber, J., et al. (2020). Inceptiontime: finding alexnet for time series classification. *Data Min. Knowl. Discov.* 34, 1936–1962. doi:10.1007/s10618-020-00710-y

Jørgensen, P., Schäfer, C., Guerra, P. G., Talajic, M., Nattel, S., and Glass, L. (2002). A mathematical model of human atrioventricular nodal function incorporating concealed conduction. *Bull. Math. Biol.* 64, 1083–1099. doi:10.1006/bulm.2002.0313

Karlsson, M., Sandberg, F., Ulimoen, S. R., and Wallman, M. (2021). Non-invasive characterization of human AV-nodal conduction delay and refractory period during atrial fibrillation. *Front. Physiol.* 12, 728955, doi:10.3389/fphys.2021.728955

Karlsson, M., Wallman, M., Platonov, P. G., Ulimoen, S. R., and Sandberg, F. (2022). ECG based assessment of circadian variation in AV-nodal conduction during AF – influence of rate control drugs. *Front. Physiology*. 13, 976526, doi:10.3389/fphys.2022.976526

Kingma, D. P., and Ba, J. (2014). Adam: a method for stochastic optimization. *arXiv preprint arXiv:1412.6980*

Kurian, T., Ambrosi, C., Hucker, W., Fedorov, V. V., and Efimov, I. R. (2010). Anatomy and electrophysiology of the human av node. *Pacing Clin. Electrophysiol.* 33, 754–762. doi:10.1111/j.1540-8159.2010.02699.x

Lagerholm, M., Peterson, C., Braccini, G., Edenbrandt, L., and Sornmo, L. (2000). Clustering ecg complexes using hermite functions and self-organizing maps. *IEEE Trans. Biomed. Eng.* 47, 838–848. doi:10.1109/10.846677

Mangin, L., Vinet, A., Pagé, P., and Glass, L. (2005). Effects of antiarrhythmic drug therapy on atrioventricular nodal function during atrial fibrillation in humans. *EP Eur.* 7, S71–S82. doi:10.1016/j.eupc.2005.03.016

Masè, M., Glass, L., Disertori, M., and Ravelli, F. (2012). Nodal recovery, dual pathway physiology, and concealed conduction determine complex av dynamics in human atrial tachyarrhythmias. *Am. J. Physiology-Heart Circulatory Physiology* 303, H1219–H1228. doi:10.1152/ajpheart.00228.2012

Masè, M., Marini, M., Disertori, M., and Ravelli, F. (2015). Dynamics of av coupling during human atrial fibrillation: role of atrial rate. *Am. J. Physiology-Heart Circulatory Physiology* 309, H198–H205. doi:10.1152/ajpheart.00726.2014

Massey, F. J., Jr (1951). The Kolmogorov-smirnov test for goodness of fit. *J. Am. Stat. Assoc.* 46, 68–78. doi:10.1080/01621459.1951.10500769

Nikolaidou, T., Aslanidi, O., Zhang, H., and Efimov, I. (2012). Structure–function relationship in the sinus and atrioventricular nodes. *Pediatr. Cardiol.* 33, 890–899. doi:10.1007/s00246-012-0249-0

Oguiza, I. (2022). Tsai - a state-of-the-art deep learning library for time series and sequential data. *Github*.

Perneger, T. V. (1998). What's wrong with bonferroni adjustments. *Bmj* 316, 1236–1238. doi:10.1136/bmj.316.7139.1236

Philippon, F., Plumb, V. J., and Kay, G. N. (1994). Differential effect of esmolol on the fast and slow av nodal pathways in patients with av nodal reentrant tachycardia. *J. Cardiovasc. Electrophysiol.* 5, 810–817. doi:10.1111/j.1540-8167.1994.tb01119.x

Plappert, F., Wallman, M., Abdollahpur, M., Platonov, P. G., Östenson, S., and Sandberg, F. (2022). An atrioventricular node model incorporating autonomic tone. *Front. Physiology* 13, 1814. doi:10.3389/fphys.2022.976468

Ryzhii, M., and Ryzhii, E. (2023). A compact multi-functional model of the rabbit atrioventricular node with dual pathways. *Front. Physiology* 14, 1126648. doi:10.3389/fphys.2023.1126648

Sandberg, F., Stridh, M., and Sörnmo, L. (2008). Frequency tracking of atrial fibrillation using hidden markov models. *IEEE Trans. Biomed. Eng.* 55, 502–511. doi:10.1109/TBME.2007.905488

Shapiro, M. A. (2013). Using equivalent doses of medications to convert atrial fibrillation. *Am. J. Cardiol.* 111, 1539. doi:10.1016/j.amjcard.2013.03.004

Stridh, M., and Sörnmo, L. (2001). Spatiotemporal qrst cancellation techniques for analysis of atrial fibrillation. *IEEE Trans. Biomed. Eng.* 48, 105–111. doi:10.1109/10.900266

Sudret, B., Marelli, S., and Wiart, J. (2017). "Surrogate models for uncertainty quantification: an overview," in *2017 11th European conference on antennas and propagation (EUCAP)* (IEEE), 793–797.

Teng, Q., Liu, Z., Song, Y., Han, K., and Lu, Y. (2022). A survey on the interpretability of deep learning in medical diagnosis. *Multimed. Syst.* 28, 2335–2355. doi:10.1007/s00530-022-00960-4

Trayanova, N. A., Popescu, D. M., and Shade, J. K. (2021). Machine learning in arrhythmia and electrophysiology. *Circulation Res.* 128, 544–566. doi:10.1161/CIRCRESAHA.120.317872

Turner, B. M., and Van Zandt, T. (2012). A tutorial on approximate bayesian computation. *J. Math. Psychol.* 56, 69–85. doi:10.1016/j.jmp.2012.02.005

Ulimoen, S. R., Enger, S., Carlson, J., Platonov, P. G., Pripp, A. H., Abdelnoor, M., et al. (2013). Comparison of four single-drug regimens on ventricular rate and arrhythmia-related symptoms in patients with permanent atrial fibrillation. *Am. J. Cardiol.* 111, 225–230. doi:10.1016/j.amjcard.2012.09.020

Wang, Z., Yan, W., and Oates, T. (2017). Time series classification from scratch with deep neural networks: a strong baseline. In *2017 International joint conference on neural networks (IJCNN)* (IEEE), 1578–1585.

Zhang, Y., and Mazgalev, T. N. (2012). Atrioventricular node functional remodeling induced by atrial fibrillation. *Heart rhythm.* 9, 1419–1425. doi:10.1016/j.hrthm.2012.04.019

Paper IV

ECG-based beat-to-beat assessment of AV node conduction properties during AF (Manuscript)

Mattias Karlsson[1,2], Felix Plappert[2], Pyotr G. Platonov[3], Sten Östenson[4], Mikael Wallman[1], and Frida Sandberg[2]

[1]Dept. of Systems and Data Analysis, Fraunhofer-Chalmers Centre, Sweden
[2]Dept. of Biomedical Engineering, Lund University, Sweden
[3]Dept. of Cardiology, Clinical Sciences, Lund University, Sweden
[4]Dept. of Internal Medicine and Dept. of Clinical Physiology, Central Hospital Kristianstad, Sweden

***Abstract*—The refractory period and conduction delay of the atrioventricular (AV) node play a crucial role in regulating the heart rate during atrial fibrillation (AF). Beat-to-beat variations in these properties are known to be induced by the autonomic nervous system but have previously not been assessable during AF. Assessing these could provide novel information for improved diagnosis, prognosis, and treatment on an individual basis.**

To estimate AV nodal conduction properties with beat-to-beat variations, we propose a methodology comprising a network model of the AV node, a particle filter, and a smoothing algorithm. The methodology was evaluated using simulated data together with electrogram (EGM) and ECG recordings from five patients in the Intracardiac Atrial Fibrillation Database. The method was then applied to ECG recordings from a tilt test study with participants in AF, to analyze autonomic influence on AV node conduction properties.

The estimated refractory period and conduction delay matched the simulated ground truth with a mean absolute error ($\pm$ std) of 169$\pm$14 ms for the refractory period in the fast pathway; 131$\pm$13 ms for the conduction delay in the fast pathway; 67$\pm$10 ms for the refractory period in the slow pathway; and 178$\pm$28 ms for the conduction delay in the slow pathway. Furthermore, a significant decrease in average refractory period in the fast ($p < 0.05$) and slow ($p < 0.001$) pathway, and conduction delay in the fast pathway ($p < 0.01$) between supine position and head-up-tilt was observed in the tilt test study, as expected in response to sympathetic activity.

These results suggest that beat-to-beat estimation of AV nodal conduction properties during AF from ECG is feasible and that the estimated properties agree with expected AV nodal modulation.

***Index Terms*—Atrial fibrillation, Atrioventricular node model, Mathematical modeling, Particle filter, Smoothing algorithm, Autonomic nervous system**

1. Introduction

Atrial fibrillation (AF), characterized by disorganized electrical activity in the atria, is the most common sustained cardiac arrhythmia with an estimated prevalence between 2% and 4% globally [1]. The disorganized electrical activity in the atria leads to rapid and irregular contraction of the atria and ventricles, resulting in an increased risk of mortality, predominantly due to heart failure or stroke [2]. Despite extensive research on AF, very little robust evidence exists to inform the best type and intensity of rate control treatment on an individual level [3, 4].

The atrioventricular (AV) node normally functions as the sole electrical connection between the atria and ventricles. During AF, the AV node plays a crucial role in protecting the ventricles from the rapid and irregular impulses originating in the atria. This function is accomplished through two distinct pathways; the fast pathway (FP) and the slow pathway (SP), which converge at the Bundle of His [5]. Depending on the refractoriness of its pathways, the AV node can either block an incoming impulse or send it through with a conduction delay. Therefore, the refractory period and conduction delay of the two pathways – here denoted $\phi = [R^{FP}, R^{SP}, D^{FP}, \text{and } D^{SP}]$ – are critical determinants of its filtering capability. The AV node thus serves an essential role in regulating the heart rate during AF, and can functionally be characterized by its properties ϕ.

The autonomic nervous system (ANS) has been shown to contribute to the initiation and maintenance of AF [6], suggesting that inter-patient variability in ANS activity might influence individual responses to AF treatment. During normal sinus rhythm, the ANS affects the heart rate primarily through changes to the sinus node automaticity, which can be quantified using heart rate variability [7]. However, during AF, the disorganized electrical activity in the atria overrides the organized electrical signals from the sinus node, preventing it from regulating the heart rate. Instead, the ANS affects the heart rate primarily through changes to the atrial fibrillatory rate and AV node conduction properties. Therefore, heart rate variability is not applicable as a tool for quantifying ANS modulation during AF. As an alternative, changes in AV nodal function could be used to quantify the ANS function during AF. Since the AV node function mainly depends on the refractory period and conduction delay of the two pathways, estimating beat-to-beat changes to these properties might give insights into the ANS function.

Assessing the AV-nodal function under AF is a complex task, since its behavior is influenced by multiple factors such as atrial impulses, autonomic modulation, as well as

its intrinsic dynamics and structure. Thus, standard signal processing tools are insufficient, and a model-based analysis is required. Several mathematical models of the AV node have previously been proposed, including [8, 9, 10, 11]. For clinical application on an individual level, a model should ideally have parameters identifiable from non-invasive data. To the best of our knowledge, the only model incorporating the refractory period and conduction delay of both pathways while simultaneously allowing for identification of model parameters based on non-invasive data is our previously proposed model [12]. Using this model, the individual 24-hour trends of the AV node properties ϕ have previously been estimated with a temporal resolution of 10 minutes using an error function based on the Poincaré plot of the RR interval series [13, 14]. However, the ANS is known to modulate AV node conduction with beat-to-beat resolution [15]. Thus, beat-to-beat resolution of the AV node properties would be preferable for studying the ANS.

Because the Poincaré plot error function relies on statistical information gathered over a sequence of several heartbeats, it is of limited use for beat-to-beat analysis. To increase temporal resolution, we propose a particle filter to estimate ϕ with beat-to-beat resolution using our previously proposed model of the AV node [12]. Particle filters approximate the solution of the filtering problem – estimating the current state of a system (ϕ in our case) based on past and current observations. Due to their ability to leverage information from previous time points effectively, particle filters are suitable for beat-to-beat estimation. Particle filters have proven especially powerful for nonlinear and non-Gaussian problems, and have previously been used, e.g. for atrial flutter detection [16], to robustly track heart rate [17], and to automatically annotate ultrasound videos of the fetal heart [18]. Moreover, by combining the resulting estimates from a particle filter with a smoothing algorithm, estimates of the current state of a system based on past, current, and future observations can be obtained [19].

This study aims to present and evaluate two particle filter based frameworks for beat-to-beat assessment of AV node conduction properties, based on intracardiac electrogram (EGM) and ECG data, respectively. The evaluation is done in three steps. Step one is to evaluate the estimation accuracy for the EGM and ECG-based methods on simulated data. Step two is to compare the estimates obtained from using synchronized ECG and EGM measurements to estimates derived from ECG measurements only. Finally, step three is to analyze the dynamics of the AV node properties during a tilt test protocol using ECG recordings from 21 patients in order to evaluate the method's ability to quantify expected changes in AV node characteristics.

2. Materials and Methods

The data used in this study are described in Section 2.1, and are followed by a description of the signal processing used to derive an atrial activation time series (AA series) and a ventricular activation time series (RR series) from the EGM and ECG recordings, in Section 2.2. Furthermore, the network model of the AV node is described in Section 2.3, and the computation of the posterior distribution of ϕ using a particle filter is described in Section 2.4.1 and 2.4.2. Finally, the posterior estimates are refined using a smoothing algorithm, as described in Section 2.4.3.

2.1. Datasets

Two previously obtained datasets are used in this study. The publicly available intracardiac atrial fibrillation database (iafdb) provides synchronized EGM and ECG measurements during AF and is used to assess coherence between EGM and ECG-based estimates [20]. Additionally, ECG recordings from a previously conducted tilt test study are used to study modulation of the AV node properties in response to changes in ANS activity [21].

2.1.1. Intracardiac atrial fibrillation database: The iafdb data consists of EGM recordings from four separate regions of the right atrium with synchronized three-lead ECG from eight patients with atrial fibrillation or flutter, sampled at 1000 Hz [20]. The recordings at the tip of the tricuspid valve annulus are used in this study, due to its proximity to the AV-node entrance. Five recordings contain solely AF and were selected for analysis, with an average patient age of 73 $\pm$ 10 years, 60% male, and an average signal duration of 58 $\pm$ 7 seconds. In addition, recordings where the catheter resting against the atrial free wall are used to create realistic simulated data, described in Supplementary Material S1.

2.1.2. Tilt test study: The tilt test study includes ECG recordings from 40 patients with persistent AF [21]. For the current study, data with sufficient quality from 21 patients were used, with an average age of 67 $\pm$ 7 years, and 67% male, previously used in [22]. The tilt test protocol involved standard 12-lead ECG recordings taken between 1 and 3 PM in a quiet room. Participants transitioned from supine position after approximately five minutes to head-down tilt (HDT) position (-30°) for approximately five minutes before finally a head-up tilt (HUT) position (+60°) for approximately five minutes. None of the patients had abnormal levels of thyroid hormones, severe renal failure requiring dialysis, heart valve disease, undergone AF ablation, or received Class I or III antiarrhythmic drugs.

2.2. Signal processing

The frameworks presented in this study for assessing the AV node conduction properties with beat-to-beat resolution rely on simultaneous analysis of the RR and AA series. These are obtained using different signal processing methods depending on whether synchronized EGM and ECG recordings are available, or only ECG recordings, as described below.

2.2.1. RR and AA series from synchronized EGM and ECG: The iafdb data includes EGM recordings with synchronized ECG recordings. The RR series is extracted using R-peak detection performed by the CardioLund ECG parser (www.cardiolund.com). The AA series is extracted from the EGM recordings using an iterative method [23] following average beat subtraction-based ventricular far-field cancellation and standard pre-processing [24, 25].

2.2.2. RR and AA series from ECG: Using solely ECG, the RR series is again extracted from the R-peak detection performed by the CardioLund ECG parser. However, the AA series cannot be extracted from the ECG. Instead, multiple AA series are generated for each RR interval based on the f-wave characteristics of the corresponding ECG segment. Each AA series, denoted $\boldsymbol{\alpha}$, is generated by a Gaussian random walk described by a mean (μ^{α}) and standard deviation (σ^{α}). Both μ^{α} and σ^{α} are estimated based on the f-wave signal extracted from the ECG by applying QRST-cancellation using the CardioLund ECG parser, before a harmonic model [26] is fitted to the f-waves to estimate the f-wave frequency and a signal quality index (SQI), sampled at 50 Hz, as described in [27]. For each RR interval, the mean (μ^{f}) and standard deviation (σ^{f}) of the inverse f-wave frequency are calculated, as well as the SQI. Subsequently, μ^{α} is drawn from $\mathcal{N}(\mu^{f}, \max(0, 0.3 - SQI)^4)$, where a SQI greater than 0.3 is deemed sufficient based on previous studies [26], and the factor 4 is chosen to get a quadratic decrease on the variance for SQI below 0.3. Further, σ^{α} is set to $4\sigma^{f}$, where the factor 4 is chosen empirically.

2.3. Network model of the AV node

Our previously introduced network model of the AV node [12] describes it as two pathways (FP and SP), each comprising 10 nodes, interconnected with a coupling node in the end connected to the ventricles (see Figure 1). Each node corresponds anatomically to a localized section of its respective pathway, while the coupling node represents the Purkinje fibers and Bundle of His [5].

The AA series extracted from data (see Section 2.2) arrives at the first nodes of the FP and the SP simultaneously. Each node can be refractory (blocking impulses) or non-refractory (transmitting impulses). Transmitted impulses arrive at adjacent nodes with an added conduction delay, and transmitting nodes immediately become refractory. The refractory period ($R_i(n)$) and conduction delay ($D_i(n)$) for node i are updated for each incoming impulse n according to Equations 1, 2, and 3,

$$R_i(n) = R_{min} + \Delta R(1 - e^{-\tilde{t}_i(n)/\tau_R}) \quad (1)$$

$$D_i(n) = D_{min} + \Delta D e^{-\tilde{t}_i(n)/\tau_D}, \quad (2)$$

$$\tilde{t}_i(n) = t_i(n) - (t_i(n-1) + R_i(n-1)), \quad (3)$$

where $\tilde{t}_i(n)$ is the diastolic interval preceding impulse n and $t_i(n)$ is the arrival time of impulse n at node i. When $\tilde{t}_i(n) < 0$, the node is in its refractory state and will block incoming impulses. Each pathway has three parameters for the refractory period and three for the conduction delay, totaling 12 model parameters $\boldsymbol{\theta} = [R^{FP}_{min}, \Delta R^{FP}, \tau^{FP}_R, R^{SP}_{min}, \Delta R^{SP}, \tau^{SP}_R, D^{FP}_{min}, \Delta D^{FP}, \tau^{FP}_D, D^{SP}_{min}, \Delta D^{SP}, \tau^{SP}_D]$. The coupling node's refractory period is fixed to the shortest RR interval in the data minus 50 ms, and its conduction delay is fixed at 60 ms [12].

The model is evaluated using a modified version of Dijkstra's algorithm [28]. Impulses are propagated through the network in an event-based fashion where the impulse with the lowest $t_i(n)$ in a queue ($\boldsymbol{q}$) of impulses is propagated next (or blocked depending on $\tilde{t}_i(n)$). Three types of data are needed to run the model. First, the parameter vector $\boldsymbol{\theta}$ is necessary, corresponding to the properties of the AV node. Second, the queue $\boldsymbol{q}$ is required, where each impulse is represented by a tuple containing arrival time $t_i(n)$ and node index i. These impulses can arrive from the atria or from a transmitting node within the model. The atrial activation times from an AA series are placed in $\boldsymbol{q}$ with corresponding node index for the first nodes in the slow and fast pathway. Finally, the repolarization time ($\boldsymbol{RT}$) for each of the 21 nodes in the model is needed, corresponding to the end of the diastolic interval ($\tilde{t}_i(n)$). The model code and a basic user example can be found at https://github.com/FraunhoferChalmersCentre/AV-node-model.

Each simulated heartbeat is associated with the vector $\boldsymbol{\theta}$ (and thus with $\boldsymbol{\phi}$) in the following way: for a given pathway, e.g. FP, R^{FP} and D^{FP} are calculated as the medians of all of $R_i(n)$ and $D_i(n)$ (Equation 1 and 2) during the time interval between the current heartbeat and previous one, with D^{FP} multiplied by 10 to account for the cumulative delay of the whole pathway. Values for SP are computed analogously.

2.4. Parameter estimation

To estimate $\boldsymbol{\phi}$ with beat-to-beat resolution, a particle filter is first used to solve the filtering problem – estimating the current state of the system based on current and past observations – before a smoothing algorithm is applied to the estimated states to solve the smoothing problem – estimating the current state of the system based on current,

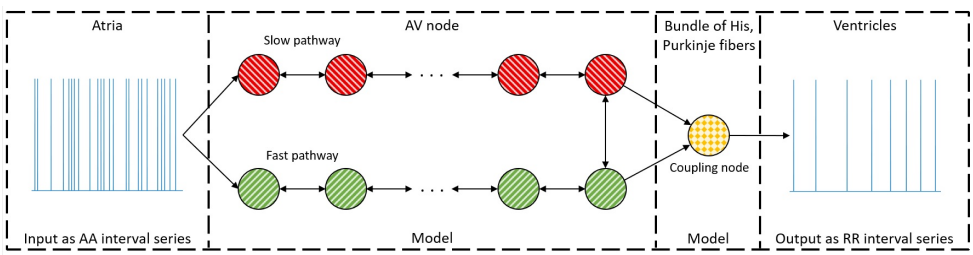

Fig. 1: A schematic representation of the network model where the yellow node represents the coupling node, the red nodes the SP, the green nodes the FP, and arrows the direction for impulse conduction. For readability, only a subset of the 21 nodes is shown [12].

past, and future observations. Moreover, two versions of the particle filter were developed, one designed for RR and AA series extracted from ECG and EGM recordings (EGM-PF), and one designed for AA series generated based on the f-wave frequencies extracted from the ECG (ECG-PF). The pseudo-code for the EGM-PF, the ECG-PF, and the smoothing algorithm are shown in Algorithm 1, 2, and 3, respectively.

2.4.1. EGM-particle filter: A basic particle filter can be described by its four phases: initialization, weighting, resampling, and propagation. These phases all affect the particles in the particle filter. In this work, each particle corresponds to a model parameter vector $\hat{\boldsymbol{\theta}}_{k,j}$, where k denotes the RR interval index (also referred to as time step or heartbeat) and j is the particle index. The EGM-PF is initialized by drawing $N = 1,000,000$ particles independently from a twelve-dimensional uniform distribution (ranges found in Supplementary Material S2), where particles with an SP refractory period greater than the FP refractory period or an SP conduction delay lesser than the FP conduction delay are excluded. Initialization is followed by a weighting phase. This starts by evaluating all $\hat{\boldsymbol{\theta}}_{1,j}$ with the model, using the current repolarization times ($\boldsymbol{RT}_j$) and the current queue ($\boldsymbol{q}_j$) filled by the AA series extracted from the EGM, until each particle has generated a ventricular activation ($\hat{V}_{k,j}$), i.e. a heartbeat. For this first time step, $\boldsymbol{RT}_j$ is set to zero for all j particles. The resulting $\boldsymbol{q}_j$ and $\boldsymbol{RT}_j$ at the time of each new heartbeat $\hat{V}_{k,j}$ is saved. After all N particles in the filter have been used to simulate heartbeats, each $\hat{V}_{k,j}$ is used together with the time of the true heartbeat (V_k) to calculate the weight $w_{k,j}$ of particle j. The weight is calculated as the probability that $\hat{V}_{k,j} - V_k$ was drawn from a normal distribution with zero mean and standard deviation σ_w, according to Equation 4,

$$w_{k,j} = \mathcal{N}(\ (\hat{V}_{k,j} - V_k)\ |0, \sigma_w^2), \tag{4}$$

where σ_w was set to 30 ms to account for uncertainties in R wave detection. After all j weights have been calculated, they are further normalized by the sum of all weights. The weighting phase is followed by a resampling phase, where new particles ($\hat{\boldsymbol{\theta}}_{k+1,j}$) with corresponding $\boldsymbol{q}_j$ and $\boldsymbol{RT}_j$ are drawn with replacement from $\hat{\boldsymbol{\theta}}_{k,j}$ with probability proportional to their weights, thereby approximating the posterior distribution at time step k. In the subsequent propagation phase, each particle is propagated one time step forward by adding a normally distributed noise drawn from $\mathcal{N}(0, \Sigma)$, where the covariance matrix Σ is calculated from all estimated parameter sets in [13] and multiplied with an estimated gain G (see Supplementary Material S2 for details). During the propagation phase, particles with an SP refractory period greater than the FP refractory period or an SP conduction delay lesser than the FP conduction delay are excluded. The propagation phase is followed by a new weighting phase. The resampling, propagation, and weighting are repeated sequentially for each RR interval, from $k = 2$ to $k = K$, where K denotes the last time step. The pseudo-code for the EGM-PF is shown in Algorithm 1.

2.4.2. ECG-particle filter: The ECG-PF is also described by its four phases: initialization, weighting, resampling, and propagation. During initialization, $N = 40,000$ particles are first independently drawn from a twelve-dimensional uniform distribution, same as for the EGM-PF, after which $N_{ECG} = 25$ copies of each particle are created ($\hat{\boldsymbol{\theta}}_{k,j}$), where $j \in [1, N \cdot N_{ECG}]$ is the particle index. Additionally, normally distributed noise drawn from $\mathcal{N}(0, \Sigma)$ is added to each particle, with previously defined Σ (Section 2.4.1). This creates $N \cdot N_{ECG}$ unique particles, identical to the number of particles in the EGM-PF.

Each unique particle is evaluated with a different AA series ($\boldsymbol{\alpha}_{k,j}$), with each $\boldsymbol{\alpha}_{k,j}$ generated by a Gaussian random walk, as described in Section 2.2.2. For the first time step, each particle is evaluated by running the model

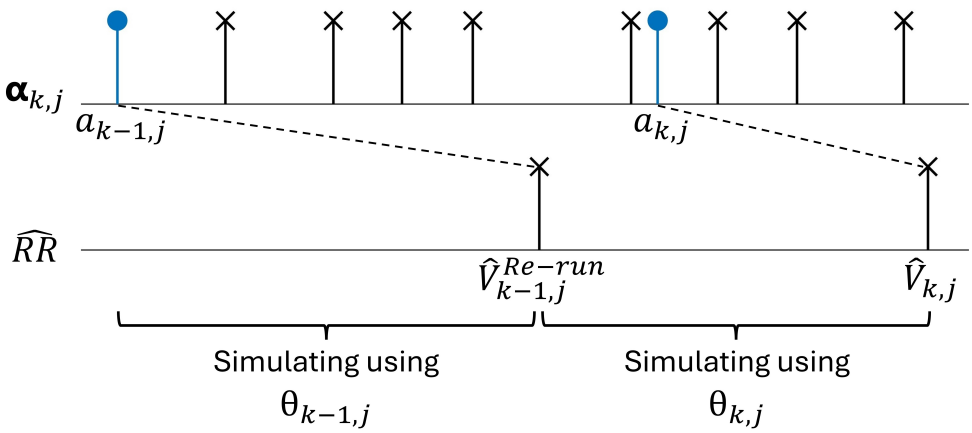

Fig. 2: An AA series $\boldsymbol{\alpha}_{k,j}$ and corresponding time series of simulated ventricular activations ($\hat{V}_{k,j}^{Re-run}$ and $\hat{V}_{k,j}$), where $a_{k-1,j}$ leads to $\hat{V}_{k,j}^{Re-run}$. Note that it is not necessarily the first AA impulse after a ventricular activation that leads to the next ventricular activation since impulses may be blocked.

Algorithm 1 EGM-particle filter

Initialization (k = 1):
Sample $\hat{\boldsymbol{\theta}}_{1,j} \sim U$ with exclusion criteria described in Sec 2.4.1.
Weighting:
Compute $\hat{V}_{1,j}$ by running the model with $\hat{\boldsymbol{\theta}}_{1,j}$, $\boldsymbol{q}_j$, and $\boldsymbol{RT}_j = \mathbf{0}$.
Save $\boldsymbol{q}_j$ and $\boldsymbol{RT}_j$ at ventricular activation time $\hat{V}_{1,j}$.
Compute $w_{1,j} = \mathcal{N}(\ (\hat{V}_{1,j} - V_1)\ |0, \sigma_w)$ (Eq. 4).
Normalize $w_{1,j} \leftarrow w_{1,j} / \sum_j w_{1,j}$.
for $k = 2$ to K **do**
  Resampling:
  Generate $\hat{\boldsymbol{\theta}}_{k,j}$ by resampling $\hat{\boldsymbol{\theta}}_{k-1,j}$ using $w_{k-1,j}$.
  Propagation:
  Sample $\hat{\boldsymbol{\theta}}_{k,j} \sim \mathcal{N}(\hat{\boldsymbol{\theta}}_{k-1,j}, \Sigma)$.
  Weighting:
  Compute $\hat{V}_{k,j}$ by running the model with $\hat{\boldsymbol{\theta}}_{k,j}$, $\boldsymbol{q}_j$, and $\boldsymbol{RT}_j$.
  Save $\boldsymbol{q}_j$ and $\boldsymbol{RT}_j$ at ventricular activation time $\hat{V}_{k,j}$.
  Compute $w_{k,j} = \mathcal{N}(\ (\hat{V}_{k,j} - V_k)\ |0, \sigma_w)$ (Eq. 4).
  Normalize $w_{k,j} \leftarrow w_{k,j} / \sum_j w_{k,j}$.
end

with $\hat{\boldsymbol{\theta}}_{1,j}$ until the next ventricular activation has been simulated ($\hat{V}_{1,j}$).

For the following time steps $k > 1$, the AA series ($\boldsymbol{\alpha}_{k,j}$) is again generated by a Gaussian random walk (see Section 2.2.2). However the arrival time of the first impulse in $\boldsymbol{\alpha}_{k,j}$ is set to the arrival time of the atrial impulse leading to $\hat{V}_{k-1,j}$, denoted $a_{k-1,j}$. Moreover, each particle is evaluated by running the model until *two* ventricular activations have been simulated ($\hat{V}^{Re-run}_{k-1,j}$ and $\hat{V}_{k,j}$). Before the time $\hat{V}^{Re-run}_{k-1,j}$, the parameter vector $\hat{\boldsymbol{\theta}}_{k-1,j}$ is used to evaluate the model, whereas $\hat{\boldsymbol{\theta}}_{k,j}$ is used after $\hat{V}^{Re-run}_{k-1,j}$, as illustrated in Figure 2. Around 98% of the time, $\hat{V}^{Re-run}_{k-1,j}$ is equal to $\hat{V}_{k-1,j}$. However, particles where $\hat{V}^{Re-run}_{k-1,j}$ differ from $\hat{V}_{k-1,j}$ are excluded. Hence, when running the particle filter, $\hat{V}^{Re-run}_{k-1,j}$ is equivalent to $\hat{V}_{k-1,j}$. This leads to impulses generated at time step $k-1$ which arrive after $a_{k-1,j}$ do not affect $\hat{V}_{k-1,j}$ in the particle filter and thus do not affect the probability of being selected for the previous resampling. Therefore, these impulses should not affect $\hat{V}_{k,j}$. To ensure this, re-running the previous time step in this manner was performed.

After $\hat{V}_{k,j}$ has been generated by the model, values for $\hat{V}_{k,j}$, $\boldsymbol{q}_j$, and $\boldsymbol{RT}_j$ are saved for each particle. As for the EGM-PF, each $\hat{V}_{k,j}$ is used together with a corresponding measured value V_k in Equation 4 to calculate the weight $w_{k,j}$.

In the resampling phase, N new particles with corresponding $\boldsymbol{q}_j$ and $\boldsymbol{RT}_j$ are drawn with replacement from $\hat{\boldsymbol{\theta}}_{k,j}$ based on their weights, before $N_{ECG} = 25$ copies of each particle are created. Normally distributed noise drawn from $\mathcal{N}(0, \Sigma)$ is added to each of the copied particles, which functions as the propagation phase, thereby creating $\hat{\boldsymbol{\theta}}_{k+1,j}$.

The propagation phase is followed by a new weighting phase before the resampling, propagation, and weighting are repeated sequentially for each RR interval, from $k = 2$ to $k = K$. The pseudo-code for the ECG-PF is shown in Algorithm 2. In addition, Matlab code with a usage example can be found at https://github.com/FraunhoferChalmersCentre/AV-node-model.

2.4.3. Smoothing algorithm: The combined particle filter and smoothing algorithm utilized in this work is commonly denoted as the forward filtering backward sampling algorithm [19]. The smoothing algorithm is applied after either the EGM-PF or the ECG-PF, and functions as the backward sampling step.

Starting at the index of the last time step $k = K$, one of the j particles is selected with probability proportional to $w_{K,j}$ and denoted $\boldsymbol{x}(K)$, where $\boldsymbol{x}$ is a vector of indices. The algorithm continues iteratively from time step $k = K-1$ to $k = 1$. The weights are updated based on the likelihood that $\hat{\boldsymbol{\theta}}_{k,j}$ originate from the selected particle at the time step of the previous iteration $\hat{\boldsymbol{\theta}}_{k+1,\boldsymbol{x}(k+1)}$, with previously defined Σ (see Section 2.4.1), according to Equation 5.

$$\hat{w}_{k,j} = w_{k,j} \mathcal{N}(\hat{\boldsymbol{\theta}}_{k+1,\boldsymbol{x}(k+1)} | \hat{\boldsymbol{\theta}}_{k,j}, \Sigma). \tag{5}$$

A new particle j is selected with probability proportional to $\hat{w}_{k,j}$ and assigned to $\boldsymbol{x}(k)$. After completion, the vector $\boldsymbol{x}$ contains one trajectory of indices corresponding to parameters $\hat{\boldsymbol{\theta}}_{k,x(k)}$ sampled from the smoothing probability density function. Running the smoothing algorithm $M = 20,000$ times generates M trajectories ($\boldsymbol{x}_m$) of $\hat{\boldsymbol{\theta}}$, all sampled from the smoothing probability density function. The pseudo-code for the smoothing algorithm is shown in Algorithm 3. Since each $\hat{\boldsymbol{\theta}}$ is associated with a $\hat{\phi}$ (see Section 2.3), the M trajectories $\boldsymbol{x}_m(k)$ also yield M trajectories of $\hat{\phi}$ sampled from the smoothing probability density function. These are used as estimates of the posterior distribution of the AV node conduction delays and refractory periods and denoted $\tilde{\boldsymbol{\phi}}_m(k)$.

2.5. Evaluation of particle filters

To evaluate the accuracy of the particle filters and smoothing algorithm, $\tilde{\boldsymbol{\phi}}_m(k)$ estimated using the EGM-PF ($\tilde{\boldsymbol{\phi}}^{EGM}_m(k)$) and ECG-PF ($\tilde{\boldsymbol{\phi}}^{ECG}_m(k)$), respectively, are compared with simulated ground truth data. Recordings from the iafdb (see Section 2.1.1) are used to create realistic simulated data, as described in Supplementary Section S1. This results in 50 model parameter sets $\boldsymbol{\theta}^*(k)$ with associated AA series and f-waves (needed for the

Algorithm 2 ECG-particle filter. Differences from the EGM-PF are marked with '*'.

Initialization (k = 1):
Sample N $\hat{\boldsymbol{\theta}} \sim U$ with exclusion criteria described in Sec 2.4.1.
* Copy $\hat{\boldsymbol{\theta}}$ N_{ECG} times to generate $\hat{\boldsymbol{\theta}}_{1,j}$
* Sample $\hat{\boldsymbol{\theta}}_{1,j} \sim \mathcal{N}(\hat{\boldsymbol{\theta}}_{1,j}, \Sigma)$
Weighting:
* Compute $\hat{V}_{1,j}$ by running the model with $\hat{\boldsymbol{\theta}}_{1,j}$, $\boldsymbol{q}_j = \boldsymbol{\alpha}_{1,j}$, and $\boldsymbol{RT}_j = \mathbf{0}$.
Save $\boldsymbol{q}_j$ and $\boldsymbol{RT}_j$ at ventricular activation time $\hat{V}_{1,j}$.
Compute $w_{1,j} = \mathcal{N}(\ (\hat{V}_{1,j} - V_1)\ |0, \sigma_w)$ (Eq. 4).
Normalize $w_{1,j} \leftarrow w_{1,j} / \sum_j w_{1,j}$.
for $k = 2$ to K **do**
Resampling:
Generate N $\hat{\boldsymbol{\theta}}$ by resampling $\hat{\boldsymbol{\theta}}_{k-1,j}$ using $w_{k-1,j}$.
* Copy $\hat{\boldsymbol{\theta}}$ N_{ECG} times to generate $\hat{\boldsymbol{\theta}}_{k,j}$
Propagation:
Sample $\hat{\boldsymbol{\theta}}_{k,j} \sim \mathcal{N}(\hat{\boldsymbol{\theta}}_{k,j}, \Sigma)$.
Weighting:
* Compute $\hat{V}_{k,j}$ by running the model as described in 2.4.2 with $\hat{\boldsymbol{\theta}}_{k-1,j}$, $\hat{\boldsymbol{\theta}}_{k,j}$, $\boldsymbol{q}_j$, $\boldsymbol{RT}_j$, and $\boldsymbol{\alpha}_{k,j}$ generated as described in 2.2.2.
Compute $w_{k,j} = \mathcal{N}(\ (\hat{V}_{k,j} - V_k)\ |0, \sigma_w)$ (Eq. 4).
Normalize $w_{k,j} \leftarrow w_{k,j} / \sum_j w_{k,j}$.
end

Algorithm 3 Smoothing algorithm

Initialization (k = K):
Sample $\boldsymbol{x}(K) \sim w_{K,j}$
for $k = K - 1$ to 1 **do**
for $j = 1$ to N **do**
Update weights: $\hat{w}_{k,j} \leftarrow w_{k,j} \mathcal{N}(\hat{\boldsymbol{\theta}}_{k+1,\boldsymbol{x}(k+1)} | \hat{\boldsymbol{\theta}}_{k,j}, \Sigma)$ (Eq. 5)
end
Sample: $\boldsymbol{x}(k) \sim \hat{w}_{k,j}$
end

EGM-PF and ECG-PF, respectively). The parameters $\boldsymbol{\theta}^*(k)$ with corresponding AA series were used in the model to generate 50 simulated RR series with associated ground truth AV node property trends ($\boldsymbol{\phi}^*(k)$).

The estimated trends $\tilde{\boldsymbol{\phi}}_m^{EGM}(k)$ and $\tilde{\boldsymbol{\phi}}_m^{ECG}(k)$ are compared to the ground truth $\boldsymbol{\phi}^*(k)$ using the mode of each AV node property. The mode is calculated individually for each time step k by sorting the M values into histogram bins with 5 ms width before identifying the center of the histogram bin with the highest count, resulting in $\tilde{\boldsymbol{\phi}}_{Mode}^{EGM}(k)$ and $\tilde{\boldsymbol{\phi}}_{Mode}^{ECG}(k)$. The l^1-norm (or absolute distance) between $\tilde{\boldsymbol{\phi}}_{Mode}^{EGM}(k)$ and $\tilde{\boldsymbol{\phi}}_{Mode}^{ECG}(k)$ and $\boldsymbol{\phi}^*(k)$, respectively, for each AV node property is used to evaluate how well the most probable estimate aligns with the ground truth. The average l^1-norm of all time steps (equivalent to the mean absolute error) is further calculated for each of the 50 simulated datasets, denoted $\overline{l^1}$. To be able to compare the results between the AV node properties, $\overline{l^1}$ is also normalized to a percentage based on the range between the highest and lowest values for each property in the simulations $\boldsymbol{\phi}^*(k)$ multiplied by 100. This is achieved by dividing with $\boldsymbol{r} = [1450.9, 1050.5, 949.4, 1109.4] \cdot 100$ ms.

Furthermore, the percentage of heartbeats for which the 95% credibility region covered $\boldsymbol{\phi}^*(k)$ ($CR_{95}(k)$) is calculated by finding the values at the 2.5th and 97.5th percentiles of $\tilde{\boldsymbol{\phi}}_m^{EGM}(k)$ and $\tilde{\boldsymbol{\phi}}_m^{ECG}(k)$ and evaluating how often $\boldsymbol{\phi}^*(k)$ lies in between. In theory, this should converge towards 95% as the number of samples grows.

2.6. Analysis of iafdb data

EGM recordings from the tip of the tricuspid valve annulus with synchronized ECG recordings, as described in Section 2.1.1, are used to compare the concordance between the results from the EGM-PF and the ECG-PF. The $\tilde{\boldsymbol{\phi}}_m^{EGM}(k)$ and $\tilde{\boldsymbol{\phi}}_m^{ECG}(k)$ are estimated using the two particle filters and smoothing algorithm before $\tilde{\boldsymbol{\phi}}_{Mode}^{EGM}(k)$ and $\tilde{\boldsymbol{\phi}}_{Mode}^{ECG}(k)$ are calculated in the same manner as in Section 2.5. The concordance between $\tilde{\boldsymbol{\phi}}_{Mode}^{EGM}(k)$ and $\tilde{\boldsymbol{\phi}}_{Mode}^{ECG}(k)$ is analyzed using the Bland–Altman plot.

2.7. Analysis of tilt test data

First, $\tilde{\boldsymbol{\phi}}_m^{ECG}(k)$ is estimated using the ECG-PF and smoothing algorithm, before $\tilde{\boldsymbol{\phi}}_{Mode}^{ECG}(k)$ is calculated in the same manner as in Section 2.5. Further, for each patient, $\tilde{\boldsymbol{\phi}}_{Mode}^{ECG}(k)$ is averaged over each tilt phase to generate one value of $\overline{\boldsymbol{\phi}}^{Supine}$, $\overline{\boldsymbol{\phi}}^{HDT}$, and $\overline{\boldsymbol{\phi}}^{HUT}$ per patient. These are used to analyze the tilt recordings, where the paired difference between $\overline{\boldsymbol{\phi}}^{Supine}$ and $\overline{\boldsymbol{\phi}}^{HDT}$ as well as between $\overline{\boldsymbol{\phi}}^{Supine}$ and $\overline{\boldsymbol{\phi}}^{HUT}$ are calculated.

2.8. Statistical analysis

The paired one-sided Wilcoxon signed rank test is used to quantify significant increase or decrease in this study, since the data do not generally follow a normal distribution according to the Shapiro-Wilk test ($p < 0.05$). This includes the paired significant test between $\overline{l^1}$ calculated using $\tilde{\boldsymbol{\phi}}_{Mode}^{EGM}(k)$ and $\tilde{\boldsymbol{\phi}}_{Mode}^{ECG}(k)$, as well as the paired difference between $\overline{\boldsymbol{\phi}}^{Supine}$ and $\overline{\boldsymbol{\phi}}^{HDT}$ and between $\overline{\boldsymbol{\phi}}^{Supine}$ and $\overline{\boldsymbol{\phi}}^{HUT}$.

3. Results

To recapitulate, three datasets were used in this study. The simulated data (see Section 2.5) are used to evaluate the estimation accuracy for the EGM and ECG-based methods. The iafdb recordings (see Section 2.1.1) are used to compare the estimates obtained from synchronized EGM and ECG recordings. The tilt recordings (see Section 2.1.2) are used to evaluate the method's ability to quantify expected changes in AV node characteristics.

The computation time (performed on a desktop computer with a Ryzen 9 5900X CPU, using the twelve cores in parallel) for $\tilde{\phi}_m^{EGM}(k)$ and $\tilde{\phi}_m^{ECG}(k)$ was on average 3.7 and 17.5 minutes per minute of data, respectively.

3.1. Evaluation of particle filters

An example of $\tilde{\phi}_m^{EGM}(k)$ and $\tilde{\phi}_m^{ECG}(k)$ and corresponding ground truth $\phi^*(k)$ is displayed in Figure 3. The shown example displays typical patterns, such as an estimated R^{SP} with a narrow credibility region (see Figure 3 b)), and where the D^{SP} can track fast changes in $\phi^*(k)$ more accurately using EGM recordings compared to ECG recordings (Figure 3 d)). Moreover, fast changes in $\phi^*(k)$ for R^{FP} and D^{FP} do not seem to be captured in either $\tilde{\phi}_m^{EGM}(k)$ nor $\tilde{\phi}_m^{ECG}(k)$ (Figure 3 a) and c)).

The results from the analysis of all simulated data are presented in Table I, where the estimation error quantified by $\overline{l^1}$ using EGM is significantly lower for R^{SP}, D^{FP}, and D^{SP} compared to using ECG. The estimate of R^{SP} has the closest match to the ground truth independently on the type of recording used, with an EGM $\overline{l^1}/\boldsymbol{r}$ of 4.48% and ECG $\overline{l^1}/\boldsymbol{r}$ of 6.33%. Further, the estimation error of D^{SP} increases the most between EGM and ECG recordings, as seen in an almost doubling of $\overline{l^1}/\boldsymbol{r}$, from 8.97% to 16%. Additionally, CR_{95} is close to 95% for all AV node properties, generally slightly over, indicating that the uncertainty bounds produced are conservative if not exact. The narrow credibility region seen in Figure 3 (and in Table I) combined with the low $\overline{l^1}/\boldsymbol{r}$ suggest that tracking beat-to-beat changes in R^{SP} accurately during AF is feasible using either ECG or EGM.

TABLE I: The mean ± standard deviation of $\overline{l^1}$ between simulated patients, using the EGM-PF and ECG-PF. † and ‡ indicate a significant decrease and increase ($p < 0.05$), respectively, for ECG compared to EGM.

	R^{FP}	R^{SP}	D^{FP}	D^{SP}
EGM $\overline{l^1}$ (ms)	174 ± 16.5	51.4 ± 11.5	105 ± 8.7	99.5 ± 23.6
ECG $\overline{l^1}$ (ms)	169 ± 13.7†	66.5 ± 9.78‡	131 ± 13.3‡	178 ± 28.1‡
EGM $\overline{l^1}/\boldsymbol{r}$ (%)	12 ± 1.14	4.89 ± 1.1	11 ± 0.916	8.97 ± 2.13
ECG $\overline{l^1}/\boldsymbol{r}$ (%)	11.7 ± 0.943†	6.33 ± 0.931‡	13.8 ± 1.4‡	16 ± 2.53‡
EGM CR_{95} (%)	99.5 ± 1.1	99.4 ± 1.39	98.9 ± 1.67	98.8 ± 2.38
ECG CR_{95} (%)	99.8 ± 0.543	96.4 ± 3.72	98.5 ± 1.97	93 ± 6.48

3.2. Concordance between ECG-PF and EGM-PF estimates

An example of $\tilde{\phi}_m^{EGM}(k)$ and $\tilde{\phi}_m^{ECG}(k)$ estimated using EGM and ECG recordings from one patient is visualized in Figure 5. Similar to the analysis of simulated data, the largest difference between using EGM and ECG recordings is seen in D^{SP} (see Figure 5 d)). Interestingly, the difference between $\tilde{\phi}_m^{EGM}(k)$ and $\tilde{\phi}_m^{ECG}(k)$ is more prominent for the first heartbeats, as seen clearly in the R^{FP} (Figure 5 a)).

The results of $\tilde{\phi}_{Mode}^{EGM}(k)$ and $\tilde{\phi}_{Mode}^{ECG}(k)$ for all patient is presented in Table II. Moreover, the Bland–Altman plots of $\tilde{\phi}_{Mode}^{EGM}(k)$ and $\tilde{\phi}_{Mode}^{ECG}(k)$ are presented in Figure 4. From this, it is possible to see a low consistent bias for all AV node properties, with no average difference larger than 5%. On average, R^{SP}, D^{FP}, and D^{SP} estimated using the EGM-PF are slightly higher compared to using ECG-PM, whereas the opposite is true for R^{FP}. Differences between $\tilde{\phi}_{Mode}^{EGM}(k)$ and $\tilde{\phi}_{Mode}^{ECG}(k)$ do not seem to be patient-specific.

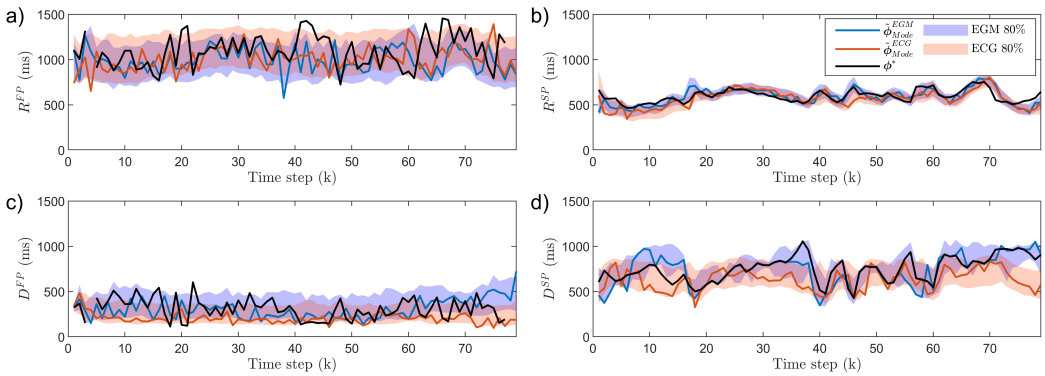

Fig. 3: AV node estimates $\tilde{\phi}_m^{EGM}(k)$ and $\tilde{\phi}_m^{ECG}(k)$ obtained based on simulated data and corresponding ground truth $\phi^*(k)$. For comparison with Table I, EGM and ECG $\overline{l^1}$ are 183 ms and 160 ms in R^{FP}, 46 ms and 58 ms in R^{FP}, 114 ms and 127 ms in R^{FP}, and 76 ms and 138 ms in R^{FP}. The modes $\tilde{\phi}_{Mode}^{EGM}(k)$ and $\tilde{\phi}_{Mode}^{ECG}(k)$ are shown with lines and the 80% credibility region as shaded background. The 80% credibility region is used over the 95% for ease of visualization.

TABLE II: The mean ± standard deviation of $\tilde{\phi}_{Mode}^{EGM}(k)$ and $\tilde{\phi}_{Mode}^{ECG}(k)$ for each time step k for all patients in the iafdb.

Patient	Data	R^{FP} (ms)	R^{SP} (ms)	D^{FP} (ms)	D^{SP} (ms)
1	EGM	917 ± 141	535 ± 104	257 ± 67.8	593 ± 135
1	ECG	993 ± 76.3	492 ± 81.6	231 ± 42.5	627 ± 78.9
2	EGM	818 ± 149	392 ± 69.9	240 ± 77.5	600 ± 132
2	ECG	926 ± 74.8	355 ± 61.3	221 ± 34.4	574 ± 68.2
3	EGM	1015 ± 108	663 ± 59.7	283 ± 120	761 ± 164
3	ECG	1037 ± 101	656 ± 79	219 ± 68.8	655 ± 104
4	EGM	1240 ± 102	1058 ± 113	355 ± 92.3	507 ± 81.4
4	ECG	1217 ± 72.2	1004 ± 37.7	259 ± 93.7	478 ± 67.7
6	EGM	952 ± 251	576 ± 183	253 ± 82	538 ± 159
6	ECG	1035 ± 89.6	559 ± 161	221 ± 50.8	485 ± 72.9

3.3. Analysis of tilt test ECG

An example of $\tilde{\phi}_m^{ECG}(k)$ for one patient is visualized in Figure 6. Interestingly, transient changes in R^{SP} and D^{SP} can be seen in response to HDT and HUT.

The results of $\overline{\phi}^{Supine}$, $\overline{\phi}^{HDT}$, and $\overline{\phi}^{HUT}$ are shown in Table III. Notably, there was a significant decrease between $\overline{\phi}^{Supine}$ and $\overline{\phi}^{HUT}$ for R^{FP} ($p < 0.05$, 16 of 21 patients), R^{SP} ($p < 0.001$, 18 of 21 patients), and D^{FP} ($p < 0.01$, 16 of 21 patients), with no significant difference in D^{SP}. Moreover, no significant difference between $\overline{\phi}^{Supine}$ and $\overline{\phi}^{HDT}$ was seen.

TABLE III: The population mean ± standard deviation of the average $\tilde{\phi}_{Mode}^{ECG}(k)$ for each tilt position for the patient in the tilt test, where † indicate a significant decrease ($p < 0.05$) compared with supine position.

	R^{FP}	R^{SP}	D^{FP}	D^{SP}
$\overline{\phi}^{Supine}$ (ms)	926.2 ± 26.2	349.4 ± 68.8	203.5 ± 13.7	523.8 ± 11.3
$\overline{\phi}^{HDT}$ (ms)	925.5 ± 24.1	338.7 ± 64.8	202.0 ± 12.4	528.8 ± 12.8
$\overline{\phi}^{HUT}$ (ms)	921.5 ± 25.3†	327.8 ± 63.4†	199.4 ± 14.2†	525.8 ± 11.7

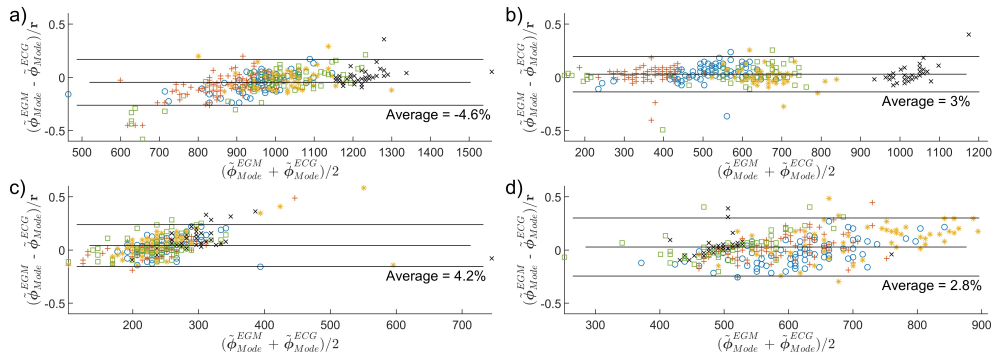

Fig. 4: Bland-Altman plot comparing the concordance between ECG-PF and EGM-PF estimates for the five patients. For comparison with Table II, Patient 1 is represented by blue 'o', Patient 2 by red '+', Patient 3 by yellow '*', Patient 4 by black 'x', and Patient 6 by green '□'.

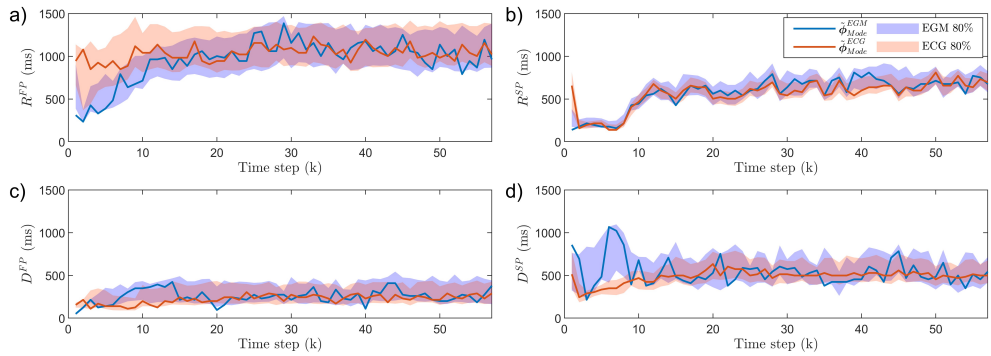

Fig. 5: The AV node estimates $\tilde{\phi}_m^{EGM}(k)$ and $\tilde{\phi}_m^{ECG}(k)$ for Patient 6 in the iafdb database. The modes $\tilde{\phi}_{Mode}^{EGM}(k)$ and $\tilde{\phi}_{Mode}^{ECG}(k)$ are shown with lines and the 80% credibility region as shaded background.

4. Discussion

This study proposes a method for estimating AV node conduction properties with beat-to-beat resolution during AF utilizing a network model of the AV node and a particle filter together with a smoothing algorithm. The method was evaluated using simulated data to analyze how well the particle filters estimated the AV node conduction properties for each heartbeat. Additionally, synchronized EGM and ECG recordings were used to analyze the concordance between estimates using the two data types. Finally, AV node properties during a tilt test protocol using ECG recordings were estimated to evaluate the method's ability to quantify expected changes in AV node characteristics.

Simulated data were used to evaluate how well the particle filter could estimate the AV node conduction properties. These simulation results can be compared with a previous study where the same AV node model was used to estimate ϕ with a 10-minute resolution [14]. In the previous study, ϕ could be estimated based on simulated data with a mean absolute error of 111 ms for R^{FP}, 12 ms for R^{SP}, 90 ms for D^{FP}, and 110 ms for D^{SP}. The mean absolute error measurement is equivalent to the ECG $\overline{l1}$ measure seen in Table I, which was 169 ms for R^{FP}, 67 ms for R^{SP}, 131 ms for D^{FP}, and 178 ms for D^{SP}. Comparing these, the proposed framework has somewhat higher error for R^{FP}, D^{FP}, and D^{SP}, and drastically higher error for R^{SP}, but with a beat-to-beat resolution, illustrating a trade-off between temporal resolution and estimation accuracy. Moreover, the computation time for the previous framework (proposed in [14]) was on average 40 seconds per minute of data whereas it is 17.5 minutes per minute using ECG in this study. Nevertheless, based on the low EGM $\overline{l1}$ of 51 ms and ECG $\overline{l1}$ of 67 ms, the proposed framework seems able to capture beat-to-beat changes in R^{SP}. Hence, an increase in temporal resolution from 10 minutes to beat-to-beat enables a more detailed analysis of the AV node dynamics, whereas using 10-minute segments is more robust and faster and therefore applicable to track slower AV node changes over an extended period (such as 24-hour which was done in [14]).

The iafdb was used to compare the concordance between the EGM-PF and the ECG-PF results. As seen in Figure 5, there are some differences when using EGM recordings compared to ECG recordings. This is clearest in D^{SP}, where estimates obtained using the EGM-PF have higher beat-to-beat variability compared to the estimates obtained using the ECG-PF. A difference in convergence time also exists, clearest seen for R^{FP} in Figure 5. These phenomena could be seen for all patients in the iafdb database. Nevertheless, R^{SP} is similar and shows a low consistent bias with no notable correlation in Figure 4 b), indicating that beat-to-beat resolution could be achieved when using either EGM or ECG recordings.

The framework presented in this paper enables analysis of beat-to-beat changes in the AV node properties, which can be used to analyze ANS activity. The ANS activity is known to change between tilt segments during a tilt test protocol, and changing the position from supine to HUT is associated with increased sympathetic activity [29]. Increased sympathetic activity is in turn associated with a decrease in AV nodal conduction delay [30, 31, 32, 33] and refractory period [32, 33]. Consequently, a change from supine to HUT can also be assumed to lead to these effects [22]. It is however unclear how HDT affects the sympathetic and parasympathetic activity, and in turn the AV node properties. Previously published results on the same dataset have shown a significant decrease in the average heart rate, the heart rate variability, and the heart rate irregularity between the supine and HUT position [22].

The results on the AV node properties in this study, seen in Table III, show a significant decrease in average $\tilde{\phi}^{ECG}_{Mode}(k)$ from supine to HUT position for R^{FP} ($p < 0.05$), R^{SP} ($p < 0.001$), and D^{FP} ($p < 0.01$). Hence, these results are in line with what can be expected for HUT. Thus, for five-minute segments, evidence suggests that the model and framework can accurately estimate changes in AV node properties originating from sympathetic activity.

The framework presented in this study can be applied to study e.g. the transient response to tilting in the AV node properties, as seen in Figure 6. This transient response

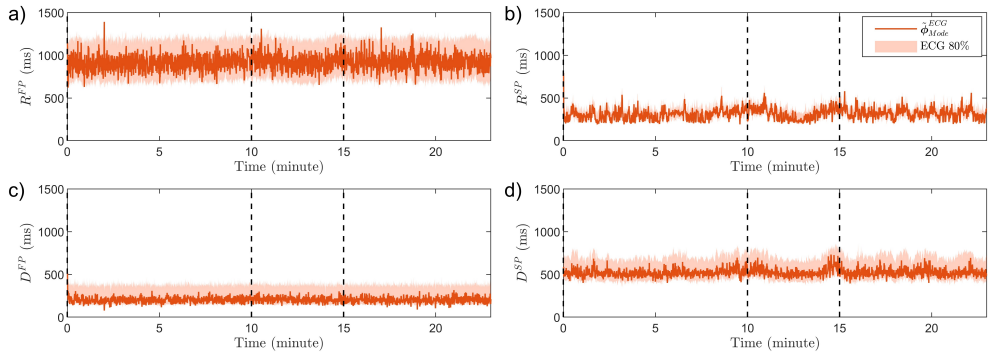

Fig. 6: The modes $\tilde{\phi}^{ECG}_{Mode}(k)$ (lines) and the 80% credibility region (shaded background) for one patient in the tilt test study. Dashed vertical lines indicate the time of tilting, staring in supine position, following five minues in HDT, before HUT.

could be seen for some of patients in the tilt dataset, with different levels of magnitude change. A similar response have previously been shown in the f-waves and heart rate [22]. However, a notable transient response to tilt in the AV node properties could not be seen for most of the patients.

4.1. Study limitations and future perspectives

The network model accounts for several important properties of the AV node conduction during AF, however, it is not a perfect replica. For example, it does not include ventricular escape rhythm and the network topology used in this work excludes some uncommon AV node structures such as multiple slow pathways. Nevertheless, these simplifications are essential to developing a model with a manageable number of parameters. Moreover, seeing as these are uncommon structures these limitations are not likely to affect the results.

The estimated AV node properties have only been validated using ground truth data generated from the same AV node model. However, obtaining the exact refractory period and conduction delay in both pathways from patients suffering from AF – if at all possible – would be very difficult and time-consuming.

Moreover, since inter-patient variability in ANS activity might influence individual responses to AF treatment, it would be of interest to quantify the ANS activity with the proposed framework during common AF treatments such as different rate control drugs.

5. Conclusion

We have proposed a novel framework for estimating patient-specific AV node properties with beat-to-beat resolution and conservative uncertainty estimates utilizing a mathematical model combined with a particle filter and smoothing algorithm. By using EGM and ECG recordings for the parameter estimation, the loss using non-invasive recordings could be studied, suggesting a high enough accuracy for capturing beat-to-beat changes in the refractory period in the SP.

We illustrate the potential of the proposed methodology by analyzing a tilt-test dataset. Results suggest that ANS-induced changes in AV node conduction properties can be assessed from ECG using the proposed method.

Acknowledgment

The computations were enabled by resources provided by the National Academic Infrastructure for Supercomputing in Sweden (NAISS) at Tetralith partially funded by the Swedish Research Council through grant agreement no. 2022-06725.

Conflict of Interest Statement

The authors declare that the research was conducted in the absence of any commercial or financial relationships that could be construed as a potential conflict of interest.

Funding

This work was supported by the Swedish Foundation for Strategic Research (Grant FID18-0023), the Swedish Research Council (Grant VR2019-04272), and the Crafoord Foundation (Grant 20200605).

References

[1] E. J. Benjamin, P. Muntner, A. Alonso, M. S. Bittencourt, C. W. Callaway, A. P. Carson, A. M. Chamberlain, A. R. Chang, S. Cheng, S. R. Das et al., "Heart disease and stroke statistics-2019 update a report from the american heart association," Circulation, 2019.

[2] N. E. Andrew, A. G. Thrift, and D. A. Cadilhac, "The prevalence, impact and economic implications of atrial fibrillation in stroke: what progress has been made?" Neuroepidemiology, vol. 40, no. 4, pp. 227–239, 2013.

[3] G. Hindricks, T. Potpara, N. Dagres, E. Arbelo, J. J. Bax, C. Blomström-Lundqvist, G. Boriani, M. Castella, G.-A. Dan, P. E. Dilaveris et al., "2020 ESC guidelines for the diagnosis and management of atrial fibrillation developed in collaboration with the european association of cardio-thoracic surgery (EACTS)," Am. J. Physiol. Heart Circ. Physiol., 2020.

[4] S. M. Al-Khatib, N. M. Allen LaPointe, R. Chatterjee, M. J. Crowley, M. E. Dupre, D. F. Kong, R. D. Lopes, T. J. Povsic, S. S. Raju, B. Shah et al., "Rate- and rhythm-control therapies in patients with atrial fibrillation: a systematic review," Annals of internal medicine, vol. 160, no. 11, pp. 760–773, 2014.

[5] T. Kurian, C. Ambrosi, W. Hucker, V. V. Fedorov, and I. R. Efimov, "Anatomy and electrophysiology of the human av node," Pacing and clinical electrophysiology, vol. 33, no. 6, pp. 754–762, 2010.

[6] M. J. Shen and D. P. Zipes, "Role of the autonomic nervous system in modulating cardiac arrhythmias," Circulation research, vol. 114, no. 6, pp. 1004–1021, 2014.

[7] F. Shaffer and J. P. Ginsberg, "An overview of heart rate variability metrics and norms," Frontiers in public health, vol. 5, p. 290215, 2017.

[8] S. Inada, J. Hancox, H. Zhang, and M. Boyett, "One-dimensional mathematical model of the atrioventricular node including atrio-nodal, nodal, and nodal-his cells," Biophysical journal, vol. 97, no. 8, pp. 2117–2127, 2009.

[9] A. M. Climent, M. S. Guillem, Y. Zhang, J. Millet, and T. Mazgalev, "Functional mathematical model of dual pathway AV nodal conduction," Am. J. Physiol. Heart Circ. Physiol., vol. 300, no. 4, pp. H1393–H1401, 2011.

[10] M. Ryzhii and E. Ryzhii, "A compact multi-functional model of the rabbit atrioventricular node with dual pathways," Frontiers in Physiology, vol. 14, p. 353, 2023.

[11] M. Henriksson, V. D. Corino, L. Sörnmo, and F. Sandberg, "A statistical atrioventricular node model accounting for pathway switching during atrial fibrillation," IEEE Trans Biomed Eng, vol. 63, no. 9, pp. 1842–1849, 2015.

[12] M. Karlsson, F. Sandberg, S. R. Ulimoen, and M. Wallman, "Non-invasive characterization of human AV-nodal conduction delay and refractory period during atrial fibrillation," Front. Physiol., p. 1849, 2021.

[13] M. Karlsson, M. Wallman, P. G. Platonov, S. R. Ulimoen, and F. Sandberg, "ECG based assessment of circadian variation in AV-nodal conduction during AF – influence of rate control drugs," Frontiers in Physiology, p. 2015, 2022.

[14] M. Karlsson, P. G. Platonov, S. R. Ulimoen, F. Sandberg, and M. Wallman, "Model-based estimation of av-nodal refractory period and conduction delay trends from ECG," Frontiers in Physiology, vol. 14, p. 1287365, 2024.

[15] C. T. Leffler, J. P. Saul, and R. J. Cohen, "Rate-related and autonomic effects on atrioventricular conduction assessed through beat-to-beat pr interval and cycle length variability," Journal of cardiovascular electrophysiology, vol. 5, no. 1, pp. 2–15, 1994.

[16] J. Lee, D. D. McManus, P. Bourrell, L. Sörnmo, and K. H. Chon, "Atrial flutter and atrial tachycardia detection using bayesian approach with high resolution time–frequency spectrum from ECG recordings," Biomedical Signal Processing and Control, vol. 8, no. 6, pp. 992–999, 2013.

[17] V. Nathan and R. Jafari, "Particle filtering and sensor fusion for robust heart rate monitoring using wearable sensors," IEEE journal of biomedical and health informatics, vol. 22, no. 6, pp. 1834–1846, 2017.

[18] C. P. Bridge, C. Ioannou, and J. A. Noble, "Automated annotation and quantitative description of ultrasound videos of the fetal heart," Medical image analysis, vol. 36, pp. 147–161, 2017.

[19] N. Chopin, O. Papaspiliopoulos et al., An introduction to sequential Monte Carlo. Springer, 2020, vol. 4.

[20] A. L. Goldberger, L. A. Amaral, L. Glass, J. M. Hausdorff, P. C. Ivanov, R. G. Mark, J. E. Mietus, G. B. Moody, C.-K. Peng, and H. E. Stanley, "Physiobank, physiotoolkit, and physionet: Components of a new research resource for complex physiologic signals," Circulation [Online], vol. 101, no. 23, pp. e215–e220, 2000.

[21] S. Östenson, V. D. Corino, J. Carlsson, and P. G. Platonov, "Autonomic influence on atrial fibrillatory process: head-up and head-down tilting," Annals of Noninvasive Electrocardiology, vol. 22, no. 2, p. e12405, 2017.

[22] F. Plappert, M. Wallman, M. Abdollahpur, P. G. Platonov, S. Östenson, and F. Sandberg, "An atrioventricular node model incorporating autonomic tone," Frontiers in Physiology, p. 1814, 2022.

[23] J. Ng, V. Sehgal, J. K. Ng, D. Gordon, and J. J. Goldberger, "Iterative method to detect atrial activations and measure cycle length from electrograms during atrial fibrillation," IEEE Transactions on Biomedical Engineering, vol. 61, no. 2, pp. 273–278, 2013.

[24] S. Shkurovich, A. V. Sahakian, and S. Swiryn, "Detection of atrial activity from high-voltage leads of implantable ventricular defibrillators using a cancellation technique," IEEE Transactions on Biomedical Engineering, vol. 45, no. 2, pp. 229–234, 1998.

[25] G. W. Botteron and J. M. Smith, "A technique for measurement of the extent of spatial organization of atrial activation during atrial fibrillation in the intact human heart," IEEE transactions on biomedical engineering, vol. 42, no. 6, pp. 579–586, 1995.

[26] M. Henriksson, A. Petrėnas, V. Marozas, F. Sandberg, and L. Sörnmo, "Model-based assessment of f-wave signal quality in patients with atrial fibrillation," IEEE Transactions on Biomedical Engineering, vol. 65, no. 11, pp. 2600–2611, 2018.

[27] M. Abdollahpur, G. Engström, P. G. Platonov, and F. Sandberg, "A subspace projection approach to quantify respiratory variations in the f-wave frequency trend," Frontiers in Physiology, vol. 13, p. 976925, 2022.

[28] M. Wallman and F. Sandberg, "Characterisation of human AV-nodal properties using a network model," Med Biol Eng, vol. 56, no. 2, pp. 247–259, 2018.

[29] L. Aponte-Becerra and P. Novak, "Tilt test: a review," Journal of Clinical Neurophysiology, vol. 38, no. 4, pp. 279–286, 2021.

[30] J. W. Lister, E. Stein, B. D. Kosowsky, S. H. Lau, and A. N. Damato, "Atrioventricular conduction in man: Effect of rate, exercise, isoproterenol and atropine on the pr interval," The American Journal of Cardiology, vol. 16, no. 4, pp. 516–523, 1965.

[31] R. C. Dhingra, E. Winslow, J. M. Pouget, S. H. Rahimtoola, and K. M. Rosen, "The effect of isoproterenol on atrioventricular and intraventricular conduction," The American Journal of Cardiology, vol. 32, no. 5, pp. 629–636, 1973.

[32] F. Morady, S. D. Nelson, W. H. Kou, R. Pratley, S. Schmaltz, M. De Buitleir, and J. B. Halter, "Electrophysiologic effects of epinephrine in humans," Journal of the American College of Cardiology, vol. 11, no. 6, pp. 1235–1244, 1988.

[33] S. F. Cossú, S. A. Rothman, I. L. Chmielewski, H. H. Hsia, R. L. Vogel, J. M. Miller, and A. E. Buxton, "The effects of isoproterenol on the cardiac conduction system: Site-specific dose dependence," Journal of cardiovascular electrophysiology, vol. 8, no. 8, pp. 847–853, 1997.